Defense Threat Reduction Agency
8725 John J. Kingman Road, MS 6201
Fort Belvoir, VA 22060-6201

DTRA-TR-02-6

TECHNICAL REPORT

Characterization of Underwater Explosions by Spectral/Cepstral Analysis, Modeling and Inversion

May 2005

DSWA 01-98-C-0157

Douglas R. Baumgardt and
Angelina Freeman

Prepared by:
ENSCO, Inc.
5400 Port Royal Road
Springfield, VA 22151-2312

DESTRUCTION NOTICE

Destroy this report when it is no longer needed.
Do not return to sender.

PLEASE NOTIFY THE DEFENSE THREAT REDUCTION AGENCY, ATTN: BDLMI, 8725 JOHN J. KINGMAN ROAD, MS-6201, FT BELVOIR, VA 22060-6201, IF YOUR ADDRESS IS INCORRECT, IF YOU WISH IT DELETED FROM THE DISTRIBUTION LIST, OR IF THE ADDRESSEE IS NO LONGER EMPLOYED BY YOUR ORGANIZATION.

DISTRIBUTION LIST UPDATE

This mailer is provided to enable DTRA to maintain current distribution lists for reports. (We would appreciate you providing the requested information.)

- ☐ Add the individual listed to your distribution list.
- ☐ Delete the cited organization/individual.
- ☐ Change of address.

NAME. _____

ORGANIZATION: _____

OLD ADDRESS	NEW ADDRESS
_____	_____
_____	_____
_____	_____

TELEPHONE NUMBER: ( ) _____

DTRA PUBLICATION NUMBER/TITLE	CHANGES/DELETIONS/ADDITONS, etc. *(Attach Sheet if more Space is Required)*
_____	_____
_____	_____
_____	_____

DTRA or other GOVERNMENT CONTRACT NUMBER: _____

CERTIFICATION of NEED-TO-KNOW BY GOVERNMENT SPONSOR (if other than DTRA):

SPONSORING ORGANIZATION: _____

CONTRACTING OFFICER or REPRESENTATIVE. _____

SIGNATURE: _____

DEFENSE THREAT REDUCTION AGENCY
ATTN: BDLMI
8725 John J Kingman Road, MS 6201
Fort Belvoir, VA 22060-6201

DEFENSE THREAT REDUCTION AGENCY
ATTN: BDLMI
8725 John J Kingman Road, MS 6201
Fort Belvoir, VA 22060-6201

REPORT DOCUMENTATION PAGE

Form Approved
OMB No. 0704-0188

1. REPORT DATE (DD-MM-YYYY)	2. REPORT TYPE	3. DATES COVERED (From - To)
00-01-2005		1 OCTOBER 1998-1 JULY 2001

4. TITLE AND SUBTITLE
Characterization of Underwater Explosions by Spectral/Cepstral Analysis, Modeling, and Inversion

5a. CONTRACT NUMBER
DSWA01-98-C-0157

5b. GRANT NUMBER
NA

5c. PROGRAM ELEMENT NUMBER
4613D

6. AUTHOR(S)
Douglas R. Baumgardt and Angelina Freeman

5d. PROJECT NUMBER
CD

5e. TASK NUMBER
CD

5f. WORK UNIT NUMBER
DH66461

7. PERFORMING ORGANIZATION NAME(S) AND ADDRESS(ES)

ENSCO, Inc.
5400 Port Royal Road
Springfield, VA 22151-2312

8. PERFORMING ORGANIZATION REPORT

9. SPONSORING / MONITORING AGENCY NAME(S) AND ADDRESS(ES)
Defense Threat Reduction Agency
8725 John J Kingman Road MS6201
Ft Belvoir VA 22060-6201

TDND/ Barber

10. SPONSOR/MONITOR'S ACRONYM(S)

11. SPONSOR/MONITOR'S REPORT NUMBER(S)
DTRA-TR-02-6

12. DISTRIBUTION / AVAILABILITY STATEMENT

Approved for public release; distribution is unlimited.

13. SUPPLEMENTARY NOTES
This work was sponsored by the Defense Threat Reduction Agency under RDT&E RMSS Code B 4613 D CD CD 66461 5P50 A 25904D

14. ABSTRACT

This report describes the development and evaluation of a cepstral analysis, modeling and inversion program for the characterization of underwater explosions recorded by seismic stations. The algorithm matches synthetic against observed cepstrums for suspected underwater blasts. The observed cepstrums are computed for regional phases (e.g., *Pn, Pg, Sn,* and *Lg*) by taking the logarithm of the trend-corrected spectrums for each phase, stacked across an regional array if array data is available, and then taking the inverse Fourier transform of log amplitude spectrum. The signed cepstrums for regional phases from underwater explosions have negative peaks caused by the reflections of the acoustic wave from the surface and positive peaks from the bubble pulse. The depth and yield of the underwater blast are determined by finding a synthetic cepstrum that most closely matches the observed cepstrum. The best matching synthetic cepstrum is the one with the highest match, either by cross correlation coefficient, L1 Norm, or L2 Norm, with the observed cepstrum.. This algorithm has been tested on the November 1999 DTRA sponsored calibration blasts in the Dead Sea, and the method gives explosion yields consistent with the known yields and depths of the events. Results are also given for analysis of two events in the Barents Sea, an explosion near Murmansk and the Kursk submarine event. We conclude that the Kursk event was an underwater explosion with a yield of about 4300 kg, or 4.73 tons, at a depth of 90 m.

15. SUBJECT TERMS
Underwater Explosions; Modeling; Regional Seismograms; Comprehensive Nuclear Test-Ban Treaty; Cepstrum Analysis; Inversion; Seismic Event Identification

16. SECURITY CLASSIFICATION OF:			17. LIMITATION OF ABSTRACT	18. NUMBER OF PAGES	19a. NAME OF RESPONSIBLE PERSON
					Douglas R. Baumgardt
a. REPORT	b. ABSTRACT	c. THIS PAGE	SAR	123	19b. TELEPHONE NUMBER (include area code)
UNCLASSIFIED	UNCLASSIFIED	UNCLASSIFIED			703-322-4718

Standard Form 298 (Rev. 8-98)
Prescribed by ANSI Std. Z39.18

SUMMARY

This study has investigated using seismic data to characterize underwater explosions and discriminate underwater blasts from earthquakes. Seismic recordings of underwater blasts can be used to characterize the source itself, based on identification of bubble pulses, and the in-situ water depths from mode-converted acoustic signals reflecting in the vicinity of the source. Thus, regional phases from underwater events, such as *Pn*, *Sn*, and *Lg*, may provide more information about the source and in-situ source characteristics than later arriving *T* phases, usually recorded hydroacoustically, since the latter signals may be strongly distorted by heterogeneities in the water-column propagation path. Bubble pulses and near-source water-column reflections cause time-independent scalloping of the spectra of regional phases that can be analyzed to infer depth and yield of the explosion.

An inversion algorithm has been prototyped in Matlab© to characterize the regional-phase cepstra from underwater explosions recorded at seismic stations. The algorithm matches synthetic against observed cepstrums for suspected underwater blasts. The observed cepstrums are computed for regional phases (e.g., *Pn, Pg, Sn,* and *Lg*) by taking the logarithm of the trend-corrected spectrums for each phase, stacked across an regional array if array data is available, and then taking the inverse Fourier transform of log amplitude spectrum. The result is the so-called signed cepstrum. Each of the individual phase cepstrums is then stacked to produce a composite cepstrum for the event. The signed cepstrums for regional phases from underwater explosions have negative peaks caused by the reflections of the acoustic wave from the surface and positive peaks from the bubble pulse. Undersea earthquakes may only have the negative water-column reflection peaks or no peaks at all. Cepstrums of the background noise before *Pn* are also computed in order to check if the peaks are caused by noise or processing artifact. Synthetic cepstrums are computed for assumed minimum-phase wavelets for an explosion of specified yield and depth in the water, which can be constrained by known bathymetry. The depth and yield of the underwater blast are determined by finding a synthetic cepstrum that most closely matches the observed cepstrum. The best matching synthetic cepstrum is the one with the

highest match, either by cross correlation coefficient, L1 Norm, or L2 Norm, with the observed cepstrum. The best matching cepstrum can be found by either exhaustive and optimal search algorithms, including the downhill simplex method. This algorithm can identify undersea events as either blast or earthquake based on the degree of correlation between a best fitting underwater explosion model cepstrum and the observed cepstrum.

The algorithm has been tested on offshore events that are suspected to be underwater chemical blasts. Offshore events have been collected by a survey of the Reviewed Event Bulletins (REB) of the Prototype National Data Center (PIDC). The main focus initially was on events around Scandinavia, in the Norwegian, North, and Baltic Seas, and the Gulf of Bothnia, recorded at one or more of the Scandinavian arrays. In this report, we test the cepstral inversion algorithm on the calibrated Dead Sea explosion data, and apply the algorithm to events in the Barents Sea, a Russian underwater blast near Murmansk and an event that coincided with the Kursk submarine disaster. The three calibrated Dead Sea explosions had actual yields of 500, 2000 and 5000 kg. Our inversion program picked estimated yields of 600, 1500, and 3100 kg, respectively. For the Kursk event, we determined that the second large event was an underwater explosion. Our inversion program picked a model that has a yield of 4300 kg, or about 4.73 tons, and a depth of 90 m. This supports news reports of a very large explosions being related to the Kursk submarine tragedy.

Although the cepstral-matching algorithm seems to work well in characterizing underwater blasts, there have been a couple of observations that have been difficult to explain. First, our estimated yields from bubble pulses to not correlate strongly with the local magnitude estimates for blasts in different regions. We noted some correlation for several events in about the same location. The lack of correlation with extreme values of yield might be due to confusion in identifying the true first bubble pulse. Second, the models that fit the observed cepstra the best must have very small surface reflection coefficients, which are on the order of -0.2 to -0.4, much less than the expected value of -1. This result may be due to poor resolution of the peaks at low quefrency.

However, we have found that the method overall is robust and provides a means for char-

acterizing and screening underwater explosions. A uses manual for the algorithm and user interfaces, prototyped in Matlab©, is included in the Appendix.

CONVERSION TABLE

Conversion Factors for U.S. Customary to metric (SI) units of measurement.

MULTIPLY →	BY →	TO GET
TO GET ←	BY ←	DIVIDE

angstrom	1.000 000 x E -10	meters (m)
atmosphere (normal)	1.013 25 x E +2	kilo pascal (kPa)
bar	1.000 000 x E +2	kilo pascal (kPa)
barn	1.000 000 x E -28	meter^2 (m^2)
British thermal unit (thermochemical)	1.054 350 x E +3	joule (J)
calorie (thermochemical)	4.184 000	joule (J)
cal (thermochemical/cm^2)	4.184 000 x E -2	mega joule/m^2 (MJ/m^2)
curie	3.700 000 x E +1	*giga bacquerel (GBq)
degree (angle)	1.745 329 x E -2	radian (rad)
degree Fahrenheit	$t_k = (t°f + 459.67)/1.8$	degree kelvin (K)
electron volt	1.602 19 x E -19	joule (J)
erg	1.000 000 x E -7	joule (J)
erg/second	1.000 000 x E -7	watt (W)
foot	3.048 000 x E -1	meter (m)
foot-pound-force	1.355 818	joule (J)
gallon (U.S. liquid)	3.785 412 x E -3	meter^3 (m^3)
inch	2.540 000 x E -2	meter (m)
jerk	1.000 000 x E +9	joule (J)
joule/kilogram (J/kg) radiation dose absorbed	1.000 000	Gray (Gy)
kilotons	4.183	terajoules
kip (1000 lbf)	4.448 222 x E +3	newton (N)
kip/inch^2 (ksi)	6.894 757 x E +3	kilo pascal (kPa)
ktap	1.000 000 x E +2	newton-second/m^2 ($N-s/m^2$)
micron	1.000 000 x E -6	meter (m)
mil	2.540 000 x E -5	meter (m)
mile (international)	1.609 344 x E +3	meter (m)
ounce	2.834 952 x E -2	kilogram (kg)
pound-force (lbs avoirdupois)	4.448 222	newton (N)
pound-force inch	1.129 848 x E -1	newton-meter (N-m)
pound-force/inch	1.751 268 x E +2	newton/meter (N/m)
pound-force/foot^2	4.788 026 x E -2	kilo pascal (kPa)
pound-force/inch^2 (psi)	6.894 757	kilo pascal (kPa)
pound-mass (lbm avoirdupois)	4.535 924 x E -1	kilogram (kg)
pound-mass-foot^2 (moment of inertia)	4.214 011 x E -2	kilogram-meter^2 ($kg-m^2$)
pound-mass/foot^3	1.601 846 x E +1	kilogram-meter^3 (kg/m^3)
rad (radiation dose absorbed)	1.000 000 x E -2	**Gray (Gy)
roentgen	2.579 760 x E -4	coulomb/kilogram (C/kg)
shake	1.000 000 x E -8	second (s)
slug	1.459 390 x E +1	kilogram (kg)
torr (mm Hg, 0^0 C)	1.333 22 x E -1	kilo pascal (kPa)

*The bacquerel (Bq) is the SI unit of radioactivity; 1 Bq = 1 event/s.
**The Gray (GY) is the SI unit of absorbed radiation.

TABLE OF CONTENTS

LIST OF FIGURES

Figure **Page**

LIST OF FIGURES CONTINUED

LIST OF FIGURES CONTINUED

APPENDIX - LIST OF FIGURES

Figure **Page**

APPENDIX LIST OF FIGURES CONTINUED

APPENDIX - LIST OF FIGURES

SECTION 1
INTRODUCTION

The problem of the identification of underwater blasts has gained increased interest recently in the context of the monitoring of the Comprehensive Nuclear Test-Ban Treaty (CTBT), which was opened for signature by the United Nations on 24 September 1996. Annex 1 to the Protocol of the CTBT calls for the installation of an International Monitoring System (IMS) including six hydroacoustic stations and five so-called "T-phase" stations. T-phase stations are seismic sensors located near the coast that can detect hydroacoustic phases converted to seismic phases at the coast. Thus, only 11 stations will be available specifically for monitoring underwater events. If an explosion occurs in the ocean, but near the coast outside of the SOFAR channel, long-range propagation of hydroacoustic signals may be blocked, and there is a possibility that the events may not be easily detected by the IMS hydroacoustic and T-phase assets directed toward the underwater explosions. Because of the relatively larger number of seismic stations, 170 primary plus auxiliary stations, called for in the CTBT Protocol for the IMS, near-coast seismic stations may have a better chance of detecting and characterizing underwater events on the continental slopes, outside of the SOFAR channel, or in confined seas. Moreover, early-arriving seismic signals, such as *Pn*, *Pg*, *Sn*, and *Lg*, produced by mode conversion of acoustic waves in the water in the vicinity of the source, may carry more useful information about in-situ source conditions than later arriving T phases that may be affected by propagation path effects in the oceanic water column.

Recent studies of underwater acoustics data for CTBT monitoring have focused primarily on analysis of T phase signals from underwater events. T phases from undersea earthquakes are usually the largest signals recorded on hydrophones (e.g., deGroot-Hedlin and Orcutt, 1997). Gitterman et al (1994) have analyzed seismic recordings of explosions in the Dead Sea, and describe a low-frequency spectral analysis method (LFSM) for discrimination of underwater explosions from earthquakes. Laney et al, 1999 have used cepstral and cross correlation analysis to characterize bubble pulse signals from calibration explosions recorded at hydrophone sensors. Calculations of first bubble pulse period at

the PIDC, using cross correlation and cepstral analysis, have agreed with theoretical values from Urick (1983) for some calibration explosions (Ronan Le Bras, personal communication).

Baumgardt and Der (1998) and Baumgardt (1999) published an extensive study of numerous examples of underwater explosions recorded at seismic stations and how they can be characterized by spectral and cepstral analysis. A simple model for underwater explosions was developed and synthetic cepstra were produced that reproduced most of the essential features of observed underwater explosion cepstra. The main features were bubble pulses, which produce positive cepstral peaks, and the surface reflections that produce strong negative cepstral peaks. The timing and relative amplitudes of these cepstral peaks provide useful constraints on the depth and yield of underwater explosions.

In the study described in this report, we have extended our original work in Baumgardt and Der (1998) to directly match model cepstra to observed cepstra with the intent of identifying and characterizing underwater explosions. Our method of "cepstral inversion" involves both exhaustive and optimal search algorithms that find models that fit the observed cepstra by maximizing a fit parameter between the observed and theoretical cepstra. In essence, modeling cepstra involves modeling the correlation structure of the different pulses produced in the water by underwater explosions.

This report describes the method of using cepstral analysis to characterize spectral modulations of underwater explosions, and examples of its application to a presumed underwater explosion off the coast of Norway near Tromso, the Dead Sea calibration explosions, a Russian underwater explosion near Murmansk, and the recent Kursk Submarine event in the Barents Sea. The theory for modeling cepstrums for underwater explosions, originally described by Baumgardt and Der (1998), and our method fitting a best-fitting model to observed cepstra, first described by Baumgardt (1999), will be reviewed. The last section will include summary and conclusions.

SECTION 2
UNDERWATER EXPLOSION MODELING APPROACH

The most striking feature of the observations of underwater explosions is the occurrence of strong modulations or scalloping in the spectra of each regional phase that produces sharp cepstral peaks. Similar features have been observed in hydroacoustic data from underwater explosions caused by the complex interference of bubble pulses and water-column bounces. In this section, we present a model and synthetic cepstra that explain the seismic observations, and estimate approximate ranges of sizes and water depths of the charges that could have produced the observed cepstra.

An underwater explosion produces the seismic signals by the conversion at the water-bottom interface of the acoustic waves in the water into each of the regional seismic phases that propagate through the earth to the stations. The strength of this conversion depends on the transfer function at the water bottom, and this function will affect the relative strengths of the different regional phases, *Pn*, *Pg*, *Sn*, and *Lg*, which in turn, controls the size of the *P/S* amplitude ratios. However, the spectral characteristics that are common to each of the phases are controlled strictly by the explosion source function in the water and should be insensitive to the water-bottom transfer function and the propagation-path effects of the earth. In this study, we only model the spectral and cepstral characteristics of the source function, not the actual relative excitation of the regional phases.

2.1 UNDERWATER EXPLOSION MODEL.

The water column time-domain source function, *W(t)*, which should be common to all phases, can be written as follows:

$$W(t) = X(t) * S(t) * R(t) \tag{2.1}$$

X(t) is the primary and bubble-pulse source function, *S(t)* is the surface-reflection transfer function, and *R(t)* is the water column reverberation transfer function, and * represents the convolution function. We discuss each of these terms below.

2.1.1 Bubble Pulse

As mentioned above, strong modulations observed in the spectra and the sharp consistent peaks in the cepstra of these events appear to result from the interference of the primary shock and bubble pulses in the water. The concept of the bubble pulse is illustrated in Figure 1.

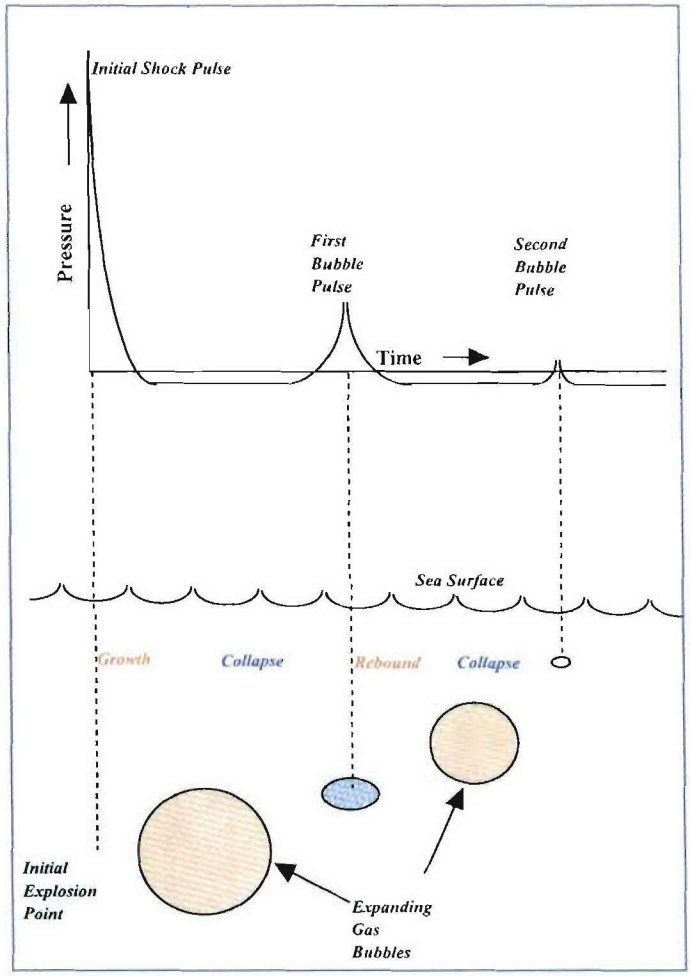

Figure 1. Illustration of a rising bubble pulse from an underwater explosion.

The dynamics of bubble pulses, or "cavitation," have been studied extensively in hydroacoustics since World War II. As illustrated in, after the initial shock front is produced by the explosion, there follow a series of positive pressure pulses generated by the expanding and contracting gas sphere that rises to the surface. The amplitude of the pulses decays steadily as the energy in the expanding gas spheres dissipates and as the bubble

rises to the surface. Accordingly, we model the primary pressure and bubble function term as follows:

$$X(t) = P(t) + \gamma b(t - \tau_1) + \gamma^2 b(t - \tau_2) \tag{2.2}$$

P(t) represents the primary pressure pulse time function in the water, *b(t)* is the bubble pulse source function, τ_1 and τ_2 are the first and second bubble pulse delay times. The time delay between the explosion pressure pulse and the first bubble pulse has been derived from theory (Willis, 1941) and verified by a number of studies (Cole, 1948) to be of the form

$$\tau_1 = \frac{K w^{1/3}}{(d+10)^{5/6}} \tag{2.3}$$

where K is a proportionality constant that depends on the type of explosive, w is the charge size in kilograms, and d is the depth of the explosions in meters. For TNT, K is equal to 2.11. [1] For the second bubble pulse, if present, we assumed $\tau_2 = \alpha \tau_1$, where α is a multiplicative factor on the order of 1.8 to 2.0. These bubble pulses can continue until the bubble rises and breaks the surface. For our models, we allowed only one or two bubble pulses. The multiplicative amplitude factor γ in (2.2) was set to 0.4, which was required to produce the spectral modulations we have observed.

Figure 2 shows a nomogram of water pressure and bubble pulse frequencies as a function of depth and yield. This is the pressure nomogram currently being used by Air Force Technical Applications Center (AFTAC) to estimate hydroacoustic pressure levels and bubble pulse frequencies, and in turn, the yields and depths of underwater explosions re-

---

[1] Note that in the original paper of Baumgardt and Der (1998), K was erroneously stated to be equal to 1.1, a typographical error. However, the actual calculations in the paper were make with the correct value.

corded on a hydroacoustic sensor at a distance of 35°. For our study, we are more interested in the bubble-pulse frequency since pressure levels are irrelevant to the analysis of seismic data. Bubble-pulse frequency, which is the inverse of τ_1 given in (2.1), is plotted as dashed lines. The curves indicate that bubble pulse frequency increases as a function of increasing depth and decreasing yield. Note that, for continental-shelf water depths of about 100 to 1000 ft, and yields between 1 and 100 tons, the bubble-pulse frequencies are in the range of 0.5 to 8 Hz, well within the short-period 20 Hz nyquist seismic bandwidth of the data collection systems of stations in the IMS.

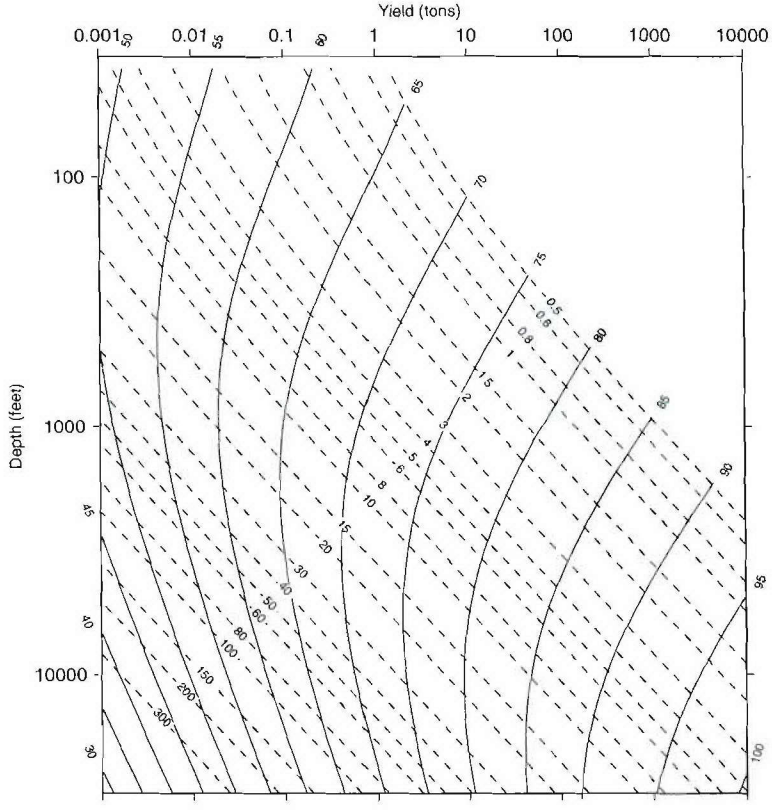

Figure 2. Pressure and bubble-pulse frequency nomogram. Solid lines are contours of signal strength at a distance of 35° in units of dB relative to 1 mPa. Dashed lines are contours of the bubble pulse frequency in Hz.

The pressure function can be expressed as a step function multiplied by a decaying exponential, as follows:

$$
\begin{aligned}
&P(t) = H(t)\exp(-\alpha t),\\
&H(t)=1 \text{ for } t \geq 0\\
&H(t) = 0 \text{ for } t < 0.
\end{aligned}
\tag{2.4}
$$

The bubble pulse term is represented as a double-sided exponential, as follows:

$$b_i(t) = \exp(-\beta|t-\tau_i|), \tag{2.5}$$

for the i'th bubble pulse with delay time τ_i. The exponential time constants in (2.4) and (2.5), are $\alpha = 100$ and $\beta = 50$.

2.1.2 Water Column Bounces

As mentioned above, an underwater explosion produces a primary pulse and one or more bubble pulses resulting in a multiple pulse wavelet that passes into the water column. This wavelet may then reflect off the free water-air interface and pass back down into the water column, as illustrated schematically in Figure 3.

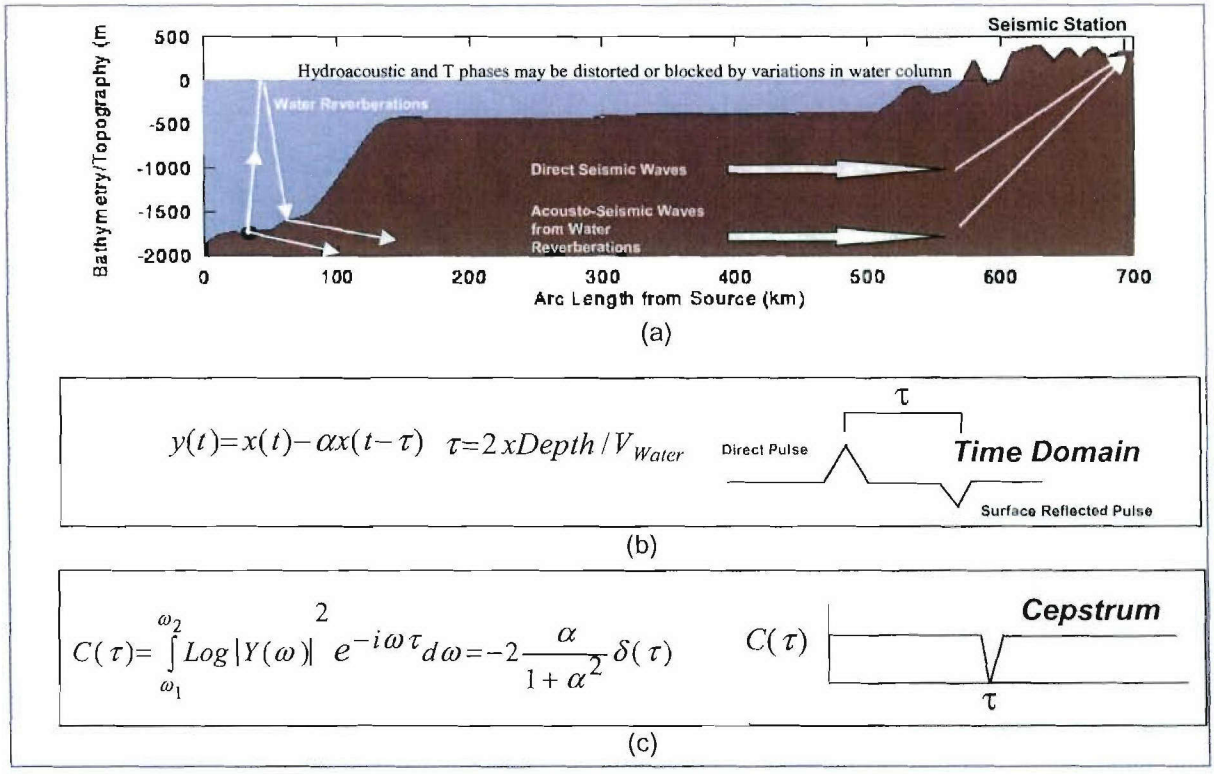

Figure 3. (a) Illustration of acoustic to seismic conversion in the water column. (b) Time domain pulses expected from underwater explosion and reflection from the free surface. (c) Cepstrum of direct and reflected pulses. Cepstrum has negative peak at quefrency of the two-way reflection time in water column.

For explosions near the continental slope, there may only be one reflection because the laterally heterogeneous bathymetry may cause the bottom reflections to be scattered and subsequent reflections not observed. The spectra for near coastal underwater events, studied by Baumgardt and Der (1998), seemed to be more consistent with just a single reflection. More examples will be shown later in this report. However, the model described in this section will include other reflections as well.

In the Baumgardt and Der (1994) model in (2.1), water column reflections were represented as the transfer function of the water column reflections convolved with the first surface reflection. The expression for the first surface reflection, *S(t)*, is

$$S(t) = \delta(t) + r_s \delta\left(t - \frac{2d}{c}\right), \tag{2.6}$$

where d is the depth of the water column, c is the speed of sound in water, which is 1480 m/sec on average for most oceanic regions, r_s is the surface reflection coefficient, and δ is the kronecker delta. The transfer function, $R(t)$, for the successive water-column reflections is given by

$$R(t) = \sum_{n=0}^{M} (r_s r_b)^n \delta\left(t - \frac{2nd}{c}\right), \tag{2.7}$$

where M is the number of reverberations in the water column and r_b is the water-bottom reflection coefficient. We typically model up to $M = 5$ reverberations in the water column after the first surface reflection.

Generally, the value of the bottom reflection coefficient, r_b, depends upon the water bottom geology. Baumgardt and Der (1998) found that values of 0.2 and 0.3 fit most of he explosions that occurred in the Baltic and North Seas. The surface reflection coefficient, r_s, physically should be about –0.9. However, as we will show later in the report, we have sometimes had to assumed lower values to fit observed cepstra.

2.1.3 Synthetic Cepstra

Cepstral analysis has proven to be a very effective method for characterizing multiple pulse wavelets, like the ones produced by this model of underwater explosions. We adopt the definition of the "real cepstrum", or the rceps function from Matlab © Signal Processing Toolbox represented as follows:

$$RCEPS\{x(t)\} = IFFT\{\log_{10} ABS[FFT(x(t)]\} \tag{2.8}$$

Where FFT and IFFT refer to Fast Fourier Transform and Inverse Fast Fourier transform, respectively. Taking the $\log_{10}$ of the spectrum prior to taking the next Fourier transform effectively whitens the spectrum. Thus, the cepstrum is just a whitened autocorrelation

function and the peaks that appear in the cepstrum are correlation peaks.

In effect, the model described above represents the correlation structure of the waveform produced by the source. As shown in Figure 3, it provides direct insight into the characteristics of the source itself with no need for more complex modeling of laterally heterogeneous earth structure. It is not really necessary when modeling cepstra to include the effects due to source coupling and propagation path because only the correlation of pulses is modeled, not the pulses themselves. The primary argument of this study is that it is much easier and more feasible to model cepstra than waveforms or spectra since the correlation structure is easier to model than the waveforms themselves. The proof of this is whether or not we can adequately match synthetic cepstra to observed cepstra.

Also, note that the model in expressions (2.1), (2.2), (2.6) and (2.7) will produce cepstra consisting of both positive and negative peaks, assuming that the primary and secondary pulses from the explosion pressure waves, bubble pulses, and water column reflections, are correlated. If the two pulses are both the same polarity, as they are in the case of the primary pulse and the bubble pulse, the result in the cepstrum will be a single positive correlation pulse. However, if there is a free surface reflection, the primary and reflection pulse will have opposite polarity, as illustrated in Figure 3(b). Thus, the cepstrum, given in, will have a negative correlation peak. The composite cepstrum will consist of both positive and negative peaks, and by matching the polarities of these peaks, we can separate the pulses produced by bubble pulses from those produced by the surface reflection.

2.2 APPLICATION TO NOVEMBER 17, 1998 EVENT NEAR TROMSO, NORWAY.

Baumgardt and Der (1998) showed a number of examples of cepstra with both positive and negative peaks, presumably produced by bubble pulses and surface reflections, respectively. In our Annual Report (Baumgardt, 1999), we described methods for matching synthetic cepstra to actual data cepstra, demonstrated on presumed explosions in the Gulf of Bothnia and in the Baltic Sea. Here, we summarize the application of the technique to a presumed underwater event that occurred on November 17, 1998 near Tromso, Norway.

2.2.1 Source and Waveform Characteristics

The event occurred off the coast of Norway that appeared in the Reviewed Event Bulletin (REB) for the PIDC with the following event parameters:

EVENT 20230910

Date	Time	Latitude	Longitude	Depth	Ndef	Magl	# of Stations
1998/11/25	11:34:29.5	69.0645	16.4273	0.0 f	12	ML 3.5	4

This event was not large enough to be retained by the REB at the time, and so the data was not available through the PIDC. Data was requested for the event from NORSAR for the four regional arrays that recorded the event. The map of the propagation paths from the event to the arrays and a record section of the data are shown in Figure 4.

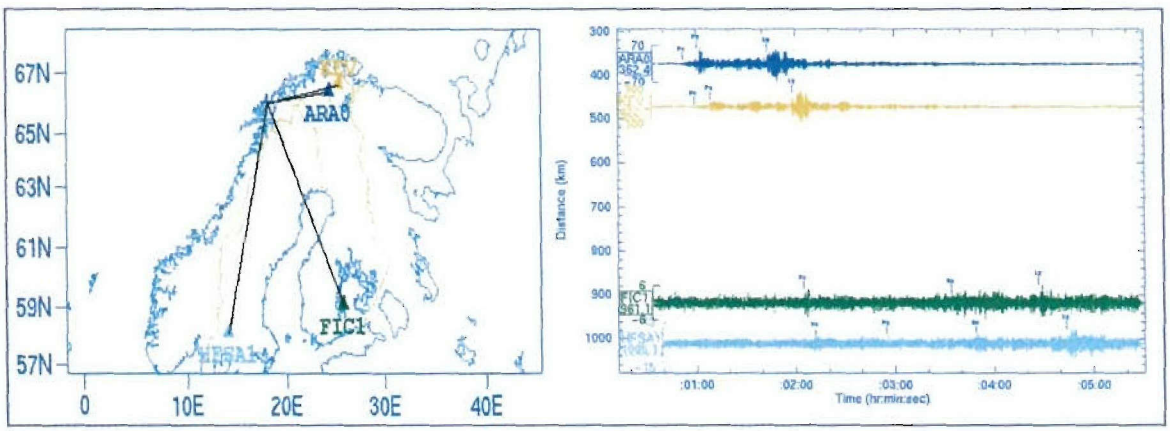

Figure 4. (Left) Map showing propagation paths from the primary stations recording the November 25, 1998 event. The station symbols are ARCES (ARA0), FINES (FIC1), Hagfors (HFSA1), and Kevo (KEV). (Right) Record section of array waveforms obtained from NORSAR for the event.

The regional phases recorded from the event are indicated on the record section on the right. Regional phases *Pn*, *Sn*, and Lg were observed across the 4 stations ARCES (ARA0), Kevo (KEV), FINES (FIC1), and Hagfors (HFSA1). The best signal-to-noise ratios were recorded at the ARCES array (ARA0) and KEV.

We relocated the event using the travel times for the regional phase picks made on the waveforms shown in The travel time models, IASPEI91 (Kennett, 1991) and the Baltic

Shield model of Bondar and Ryaboy (1997) were used to relocate the event. The picks in Figure 4 (right) are close to the ones in the REB except that the NORSAR picks were not included. We were not able to see large enough signals at NORSAR to make picks on individual channels although the REB did include picks for NORSAR. It is possible that the REB picks were made by the PIDC analysis on beams, which would enhance phases not clearly visible on individual traces.

Table 1 shows the results of the relocation. The best location, using the Baltic Shield model and our phase picks, is shown in Figure 5. IASPEI91 refers to the global travel time curves (Kennett, 1991) that have been used for routine location in the PIDC. Improved regional travel time curves for this region have been developed by Bondar and Ryaboy (1997), which is referred to as the Baltic Travel time curves. The term "local network" refers to the phase picks in Figure 4 (b) and "IMS network" refers to the picks in the REB.

Table 1. Location Estimates for the November 25, 1998 Presumed Explosion Near Tromso, Norway.

Network	Travel Time Table	Latitude (Deg. N.)	Longitude (Deg. E)	Error Ellipse (Sq. Km)	RMS Time Residuals (sec)
IMS	IASPEI91	68.940	16.583	2.005	1.27
Local	IASPEI91	68.935	16.710	3679	0.87
IMS	Baltic	69.052	16.434	685	1.27
Local	Baltic	69.083	16.465	1187	0.96

This location places the event in amongst several groups of islands off the coast of Norway and the confidence ellipse covers mostly water-covered areas. However, the ellipse clearly overlaps numerous offshore islands although it does not overlap the mainland. So,

refined location analysis in this case cannot definitively determine if the event is on land or underwater.

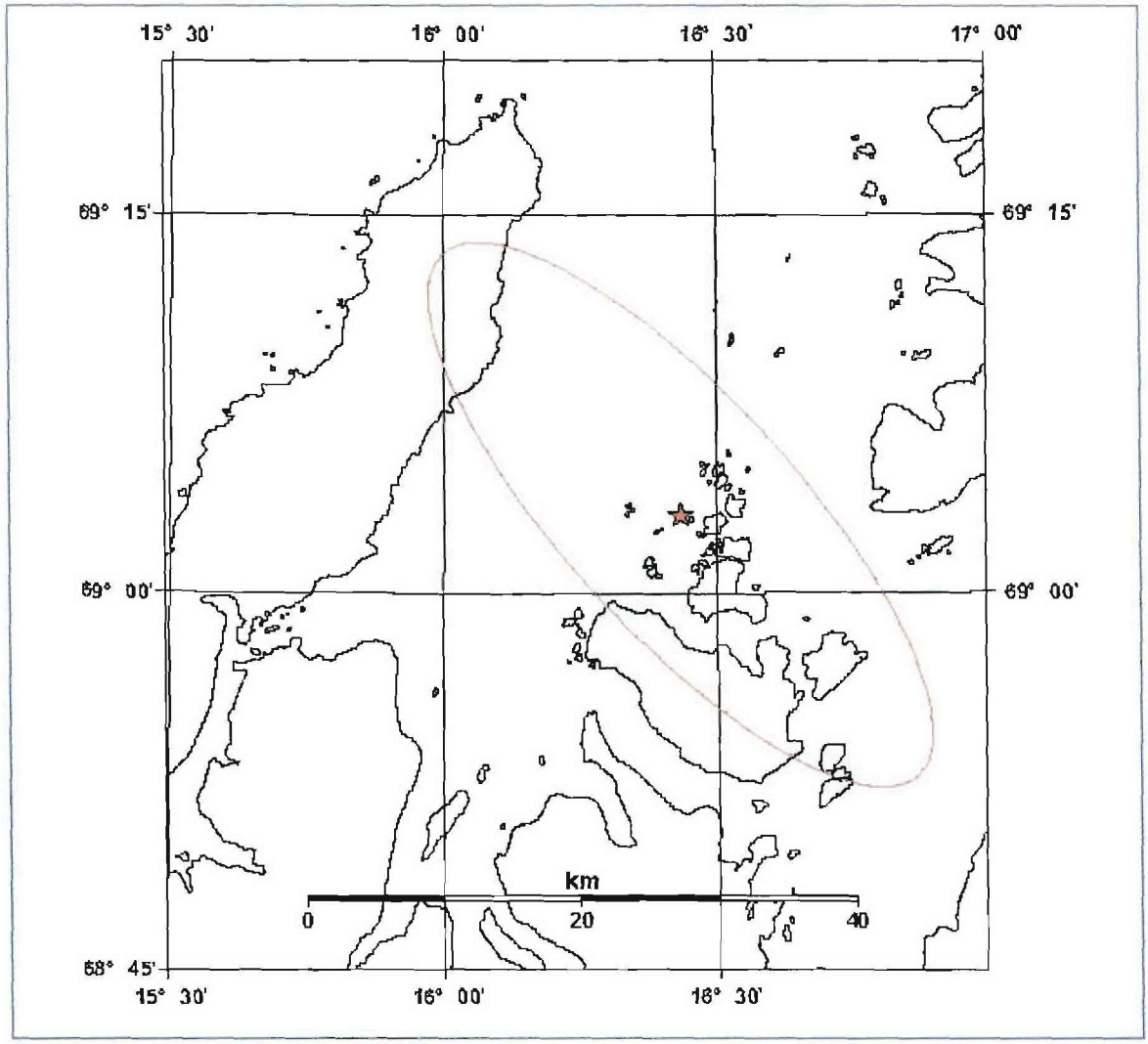

Figure 5. Epicenter and confidence ellipse of the relocated Tromso event of November 28, 1998.

Figure 6 (top) shows a map with the great circle propagation path from the event location reported in the REB to the ARCES array center element. Figure 6 (bottom) shows part of the bathymetric/topographic data for the first 50 km of the path from the source to the receiver. The bathymetry gives a water depth of 130 m in the vicinity of the source, although the water depth varies from between 50 to 300 m along the path. Also, Figure 6 shows that the event was only within about 13 to 15 km of the land of the offshore is-

lands, which is less than the REB epicenter error ellipse long axis of about 21 km. However, as we will show below, the spectral/cepstral characteristics of the signal are consistent with a water depth of 130 m.

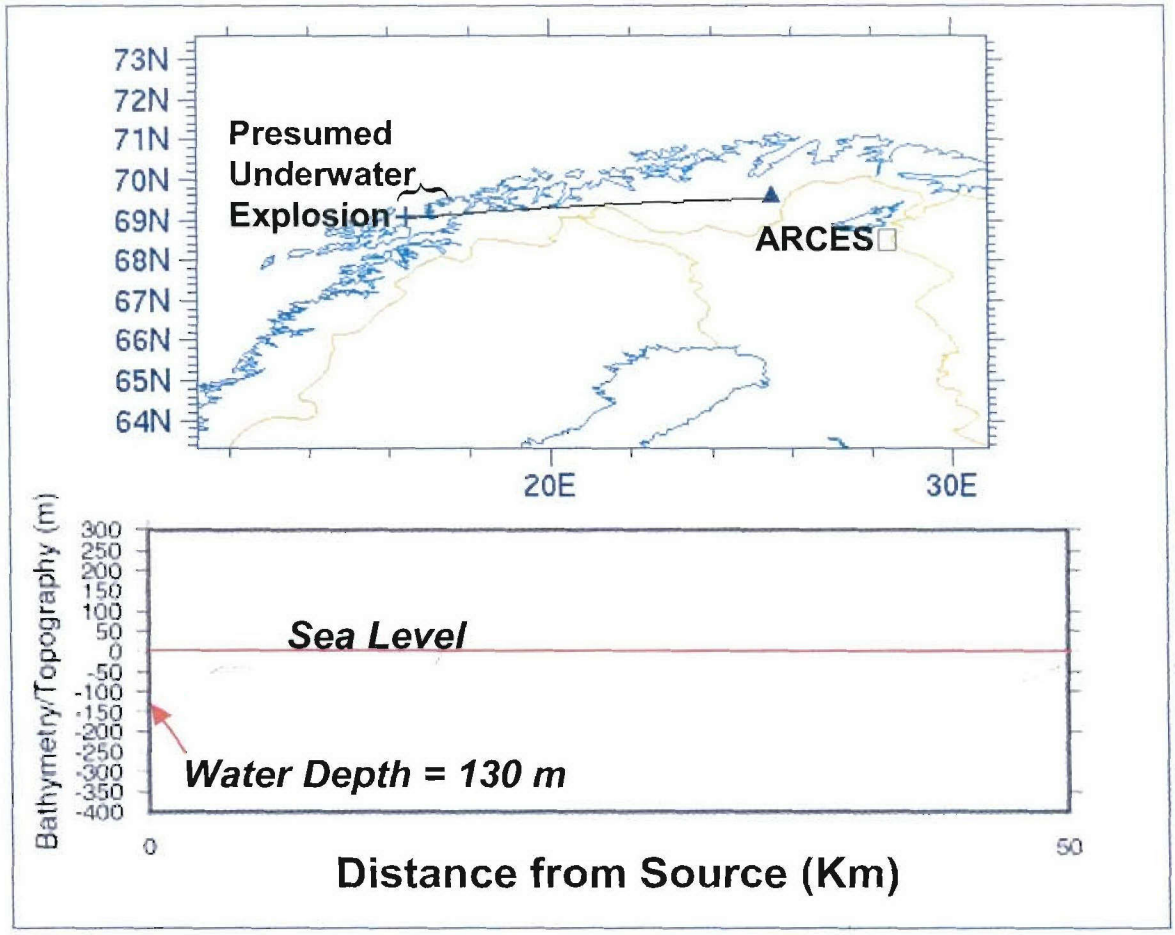

Figure 6. (Top) Great circle path from the PIDC location of the Tromso event to the ARCES array. (Bottom) Bathymetric and topographic cross section from source to receiver showing water depth in the region is about 130 m.

2.2.2 Spectral and Cepstral Analysis

For the analysis of this event, we chose to focus primarily on the waveforms from the ARCES array, which was closest to the event and had the best signal-to-noise ratios of all the stations that recorded it.

Figure 7(a) shows a bandpass filter analysis of the ARCES waveforms, with frequency bands from 0.5 to 2.5 Hz up to 10 to 16 Hz. The signal-to-noise ratio is quite high

through the entire spectral band. The *Pg* and *Lg* phases are notably large throughout the band from 2 to 7 Hz and the first arrival *Pn* is emergent. *Pn/Lg* ratios are generally less than 1, except at frequencies above 8 Hz, indicating significant shear-wave excitation. Baumgardt and Der (1998) showed that, under certain circumstances, the *Pn/Lg* or *Pg/Lg* ratio might discriminate earthquakes and explosions for screening purposes. However, it is doubtful that a *Pn/Lg* or *Pg/Lg* ratios would confidently screen this event out as an earthquake.

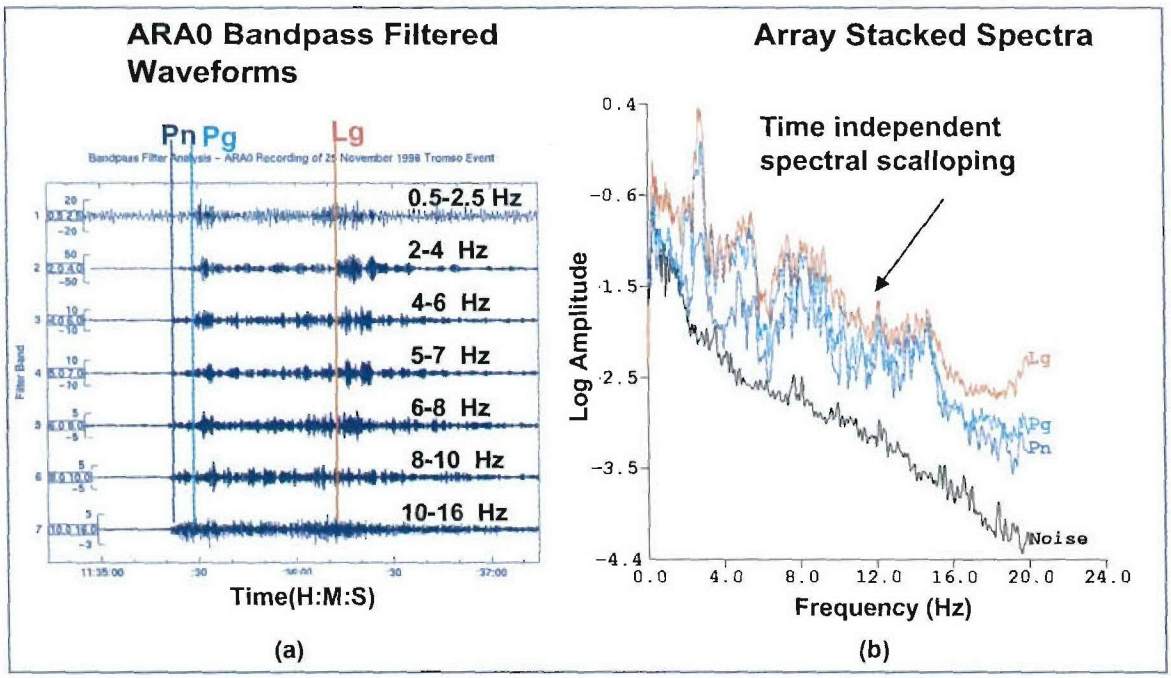

Figure 7. (a) Bandpass filtered waveforms of the ARA0 channel of the ARCES array from the November 25, 1998 event near Tromso. (b) Array stacked spectra of the phases recorded at ARCES.

Figure 7(b) shows the array-averaged spectra for the different phases and background noise. The spectra are computed on each individual ARCES vertical-component channel by windowing the phases, starting at the time picks shown in Figure 7(a), for 20 seconds and applying a Parzen window. The spectra for each channel are then averaged across the array, which produces much smoother spectra than the individual channel spectra.

These figures show spectral modulations or "scalloping" in all phases with a strong spectral peak at about 3 Hz. None of these features appears in the noise. Spectra of this kind

have been shown to be caused by source multiplicity, either due to ripple fire in mine blasts (Baumgardt and Ziegler, 1988) or by water column reverberations and bubble pulses in underwater explosions (Baumgardt and Der, 1998). Since the event occurs off the coast, it is likely to be an underwater explosion, as can be shown by cepstral analysis.

The spectra in Figure 7(b) clearly have a frequency-dependent trend due to the combined effect of the instrument response, the source spectral trend, and the effects of the propagation path. Whitening the spectra would remove the trends due to these effects and enhance the effect of the spectral modulations in the cepstum. We have performed a number of experiments with whitening the spectra for this purpose. In our earlier research (Baumgardt and Ziegler, 1988; Baumgardt and Der, 1998), we would first remove the instrument response, fit a polynomial function to the residual trend, and then remove the polynomial trend. However, deconvolving the instrument response sometimes causes a blowup in the spectrum at low frequencies that can cause unwanted processing artifacts in the cepstra. In our current study, we have chosen to only fit the polynomial trend and remove it, skipping the step of removing the instrument response, and have found that this procedure produces reasonably stable cepstra without the low-frequency blowup problem. This was discussed in more detail in our earlier report (Baumgardt, 1999).

The expression for the cepstrum can be written as follows:

$$RCEP\{x(t)\} = FFT\{\log_{10} ABS[\underline{x}(f)]\} \qquad (2.9)$$

where FFT stands for "fast fourier transform" and $ABS[\underline{x}]$ refers to the whitened amplitude spectrum. This expression is similar to expression (2.8) in the previous section for the theoretical cepstra except that the spectra have been whitened by removing the polynomial trend prior to taking the second FFT. In the case of theoretical cepstra, no whitening is applied to the spectrum, other than the $\log_{10}$, before taking the second FFT.

For the regional arrays, cepstra can be computed for each of the phases and then averaged across the array channels. This averaging accentuates the peaks and troughs in the cepstra caused by real source effects, since they show up on each channel, and diminish those due

to site effects. Comparisons of single channel and array averaged cepstra have shown that the array averaged cepstra have much sharper peaks and troughs than the single channel cepstra. Moreover, further enhancement of the peaks and troughs can be attained by averaging or stacking the array-averaged cepstra for each phase to form a composite, stack cepstrum.

Figure 8 shows cepstra for the three phases, the stack of the three cepstra, and the cepstra of the background noise. The resultant cepstra, using (2.9), are a function of delay time between the multiple pulses, called "quefrency" in units of time (sec), and are signed. A cepstrum for the noise spectrum is also computed in order to check for cepstral features that may be due to processing artifact rather than source effects. We look for cepstral peaks in the individual phase cepstra that do not appear in the noise cepstra. The cepstra in have been shifted for display purposes and the absolute amplitudes are arbitrary. Positive cepstral peaks indicate pulses that are correlated with the same polarity and negative peaks, or troughs, are produced by pulses with reverse polarity. As shown by Baumgardt and Der (1998), positive peaks are caused by bubble pulses with positive polarity and negative peaks are produced by reflections of acoustic waves off the water-air interface.

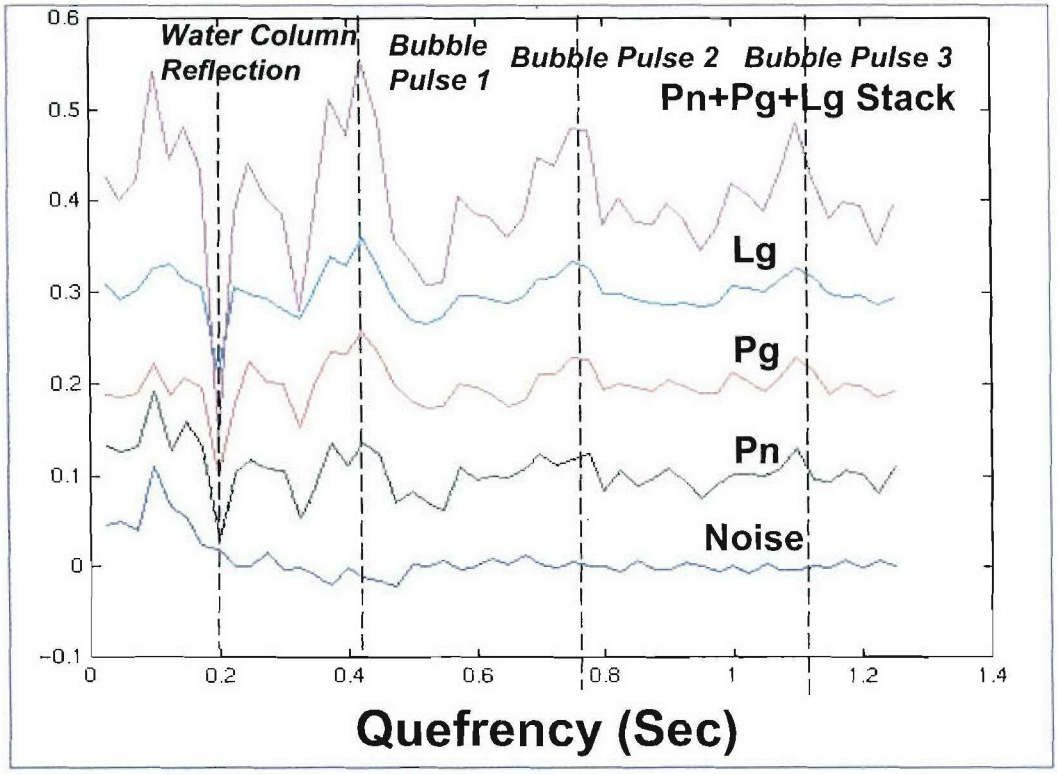

Figure 8. Shifted cepstra computed for the spectra shown in Figure 7(b).

2.2.3 Synthetic Cepstra

The modeling techniques, described by Baumgardt and Der (1998) and in the previous section, are illustrated in Figure 9. We compute wavelets for the bubble pulse, shown on top, and water column reverberations, shown as the second trace, for a given assumed yield and depth in the water. Other parameters that must be specified include average water column depth, that can be obtained from the bathymetry, and the surface and water bottom reflection coefficients, which we assume to be –0.9 and 0.3, respectively. As in the case of water depth, these parameters can be estimated with some degree of accuracy, but it is also conceivable that they can be inferred from the data. We assume that the acoustic waves in the water reflect from first-order discontinuities at the bottom and the surface.

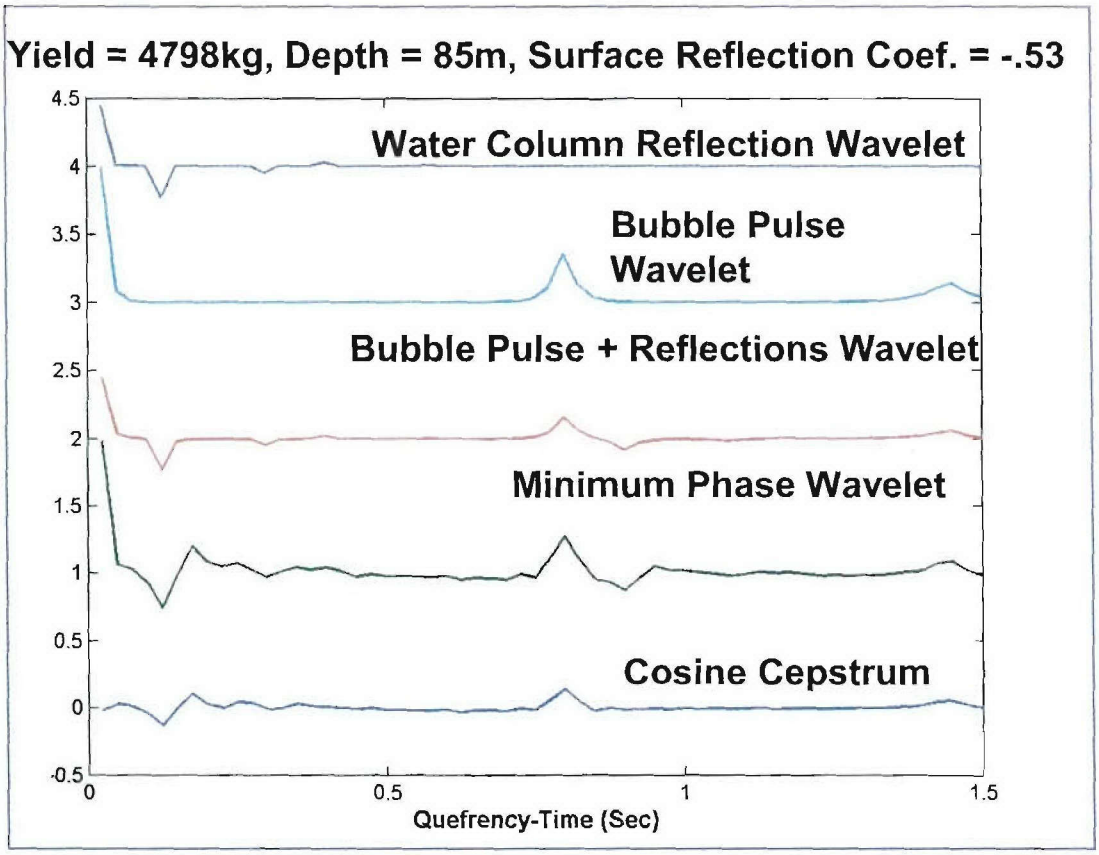

Figure 9. Method for computing the cepstral model for matching observed cepstra.

The final synthetic cepstrum is the convolution of the source plus bubble pulse wavelet and reflection wavelet. We then compute the cepstrum of this composite wavelet, which is shown at the bottom of Figure 9. We also show a minimum phase wavelet reconstruction from the cepstrum, which is identical to the original wavelet since the wavelets were constructed minimum phase.[2]

2.2.4 Cepstral Inversion

Finally, we seek a synthetic cepstrum, like that at the bottom of Figure 9 that matches the observed cepstrum. For this purpose, we compute the correlation coefficient between the

[2] The assumption of "minimum phase" means that the amplitudes of the pulses in the wavelet decrease with time, a reasonable assumption for bubble pulses and surface reflections. However, there is no way from the cepstrums alone to determine if the signals are minimum phase or not.

stacked observed cepstrum and the synthetic cepstrum and seek a cepstrum that provides the maximum correlation.

We have first considered a simple exhaustive search method, where the parameter space of blast yield and depth in the water is gridded and synthetic cepstra are computed for each grid point. The method correlates the synthetic cepstrum at each grid point with the observed cepstrum, compute a correlation coefficient surface over the depth/yield parameter space, and look for the peaks in the depth/yield surface.

Figure 10 shows the resultant correlation coefficient surface plotted as a 3D surface (left) and as a contour plot (right). Both displays have a distinct peak in the correlation, with a maximum correlation coefficient of 0.73, corresponding to a water depth of 130 m and yield of 1800 kg or about 1.98 tons. It is evident in that depth is well constrained but yield is less well constrained. The yield is controlled exclusively by the bubble pulse delay time, although the bubble pulse delay is also a function of depth. However, depth is constrained also by the negative peak delay time, corresponding to the two-way water-column reflection time.

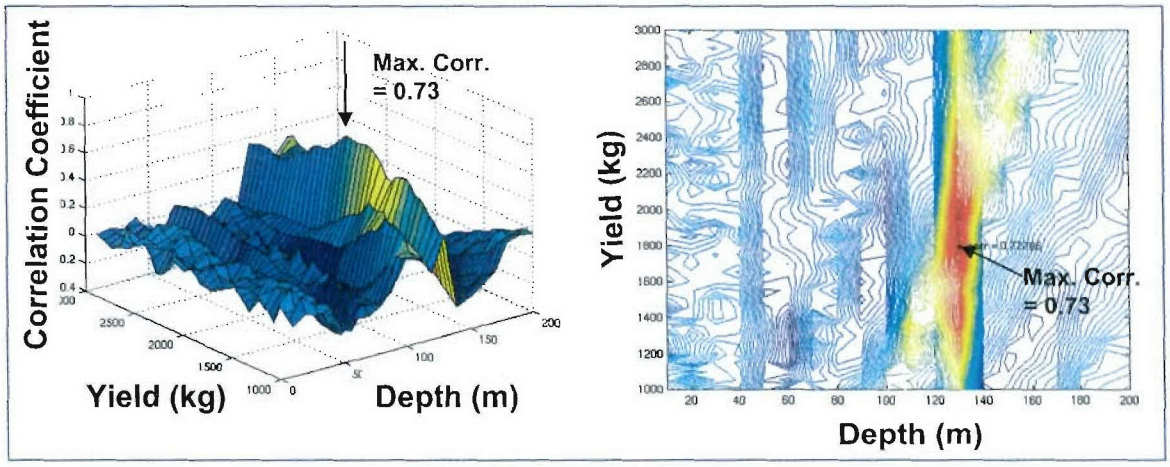

Figure 10. Synthetic cepstra computed for a range of yield (1000 to 3000 kg) and depth (0 to 200 m) and each correlated with the observed cepstra. Surface plot (left) and contour plot (right) showing the maximum peak that gives the best estimate of the depth and yield of the explosion.

The search algorithm found a depth of 130 m based on the 0.2-second surface reflection time. Note that this would be the depth of the explosion below the water surface. It is notable that the inferred explosion depth of 130 m is close to the actual water depth of the source location as inferred from bathymetry, shown in the cross section in Figure 6.

This suggests that the explosion may have occurred near the bottom or on the bottom. However, that knowledge of the water depth is not actually required to infer the explosion depth in the water, since the reflection from the surface is by far the strongest signal. We actually assumed a water depth of 225 m in our model. Reflections from the bottom may, in principle, be observed and reveal water depth, but they are very weak, as is evident in Figure 9.

Generally, we have not observed strong bottom reflections in the observed cepstra, which indicates that the bottom reflection coefficient is very small. Small-reflection coefficients may be caused by roughness of the bottom itself. Moreover, transitional ocean bottom layers may cause frequency-dependent reflection coefficients that distort the bottom reflections such that they do not correlate with the primary pulses and produce strong cepstral peaks. However, water depths at given locations in the ocean are usually well known and need not be inferred by this method. However, knowing the maximum water depth is useful because it constrains the required search space.

The sensitivity to yield is shown in Figure 11, where the correlation coefficient is plotted as a function of yield for the depth of 130 m. The maximum peak was at 1800 kg, but another peak of comparable strength appears at closer to 2000 kg. However, the overall broad peak is about 200 or 300 kg in width, which provides an estimate of the resolution of the method to yield. Thus, a better estimate of yield might be 1900 kg $\pm$ 200 kg.

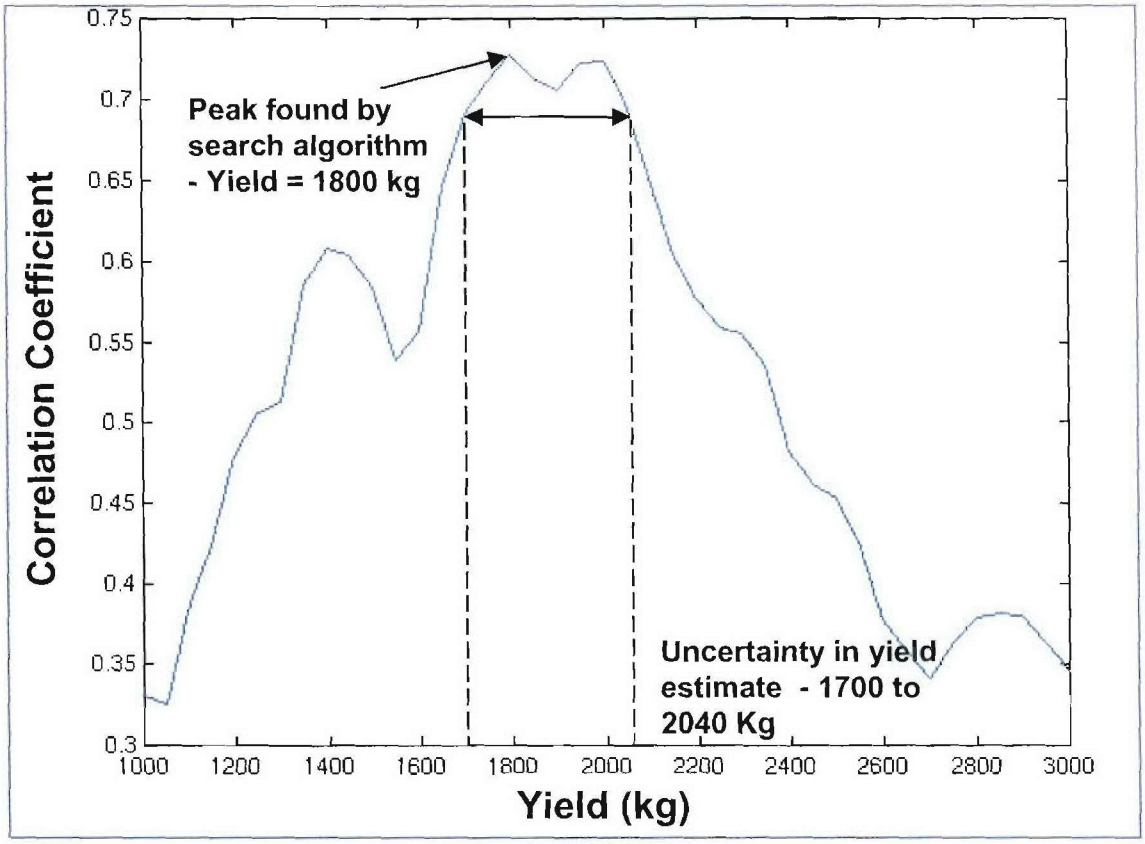

Figure 11. Sensitivity of the correlation method for estimating underwater explosion yield by matching synthetic and observed cepstra.

Finally, Figure 12 shows a direct comparison of the observed stack cepstrum and the best-matching synthetic cepstrum. This comparison shows that, although the match is not perfect, reasonably good matches of the essential features, the negative peaks of the water column reflection and the bubble pulses, have been attained. The primary features that drive the match correlation is the position of the negative surface-reflection peak and the bubble pulse peaks, three of which can be seen in this case.

We can also check the yield with the AFTAC pressure nomogram in Figure 2. The bubble pulse period for the best fitting cepstrum in Figure 12 is about 0.42 sec, or a bubble-pulse frequency of 2.4 Hz. (In spectral terms, the spectral scalloping that gives rise to the cepstral peak has modulation period of 2.4 Hz.) Given a depth of 130 m, or 426 ft, Figure 1 gives a yield of a just above 1 ton, that is consistent with the 1.98 ton value obtained by cepstral fitting search algorithm.

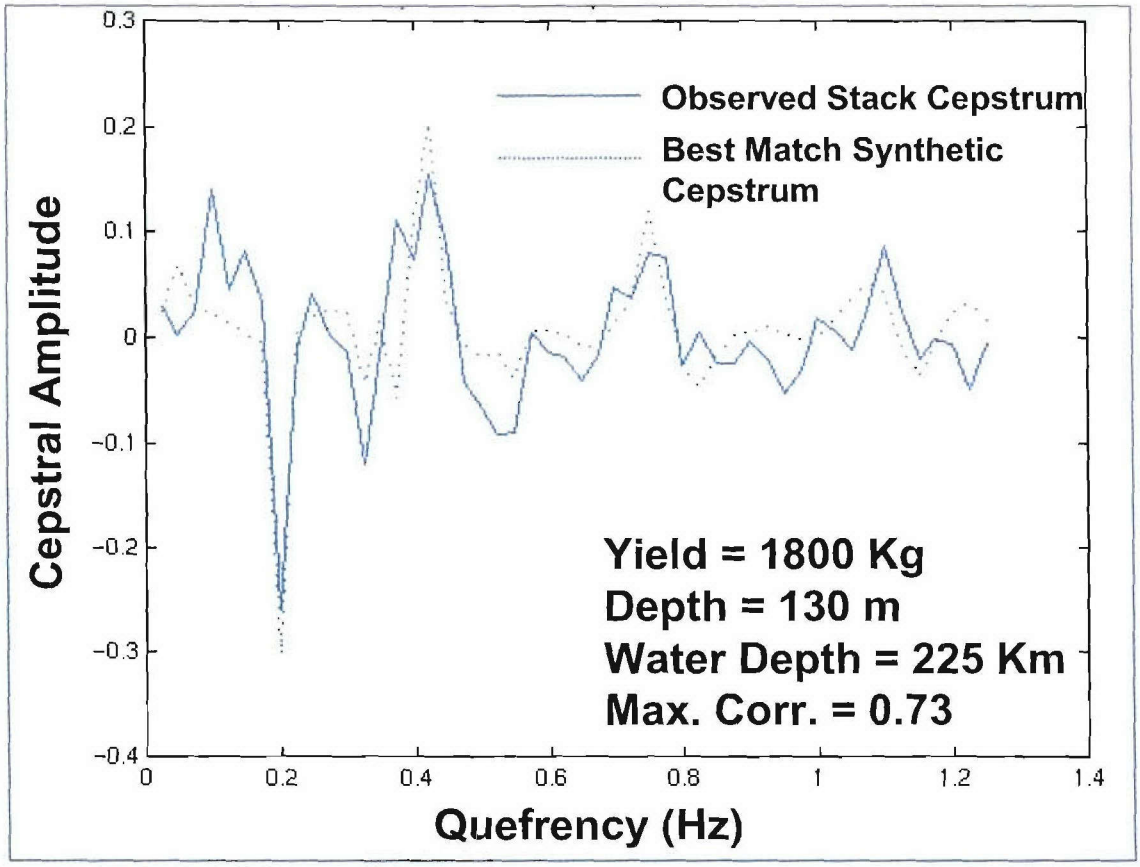

Figure 12. Match of the synthetic cepstra (dotted) to the observed stacked cepstra the best fitting underwater explosion model.

Thus, this analysis strongly suggests that this event must be an underwater explosion of close to 2 tons to explain the spectra and cepstra. The event was not identified by the PIDC as an underwater explosion, and in fact, the IMS hydroacoustic network did not detect the event because propagation paths were blocked to all hydroacoustic stations.

It might be argued that this is only a small conventional explosion of no importance and if it had been a nuclear blast of much larger yield, the IMS hydroacoustic network would have easily detected it. From Figure 2, the pressure level at 130 m for a 1-ton shot would have been between 70 and 75 mPa at a distance of 35°. If the explosion had been 10,000 tons, or 10 Kt, consistent with a small nuclear blast, the pressure levels at 35° from Figure 1 would only be between 85 and 90 mPa. This increase in pressure level for a two order-of-magnitude increase of yield, may not be able to overcome the blockage effects in order to be detected at an IMS hydroacoustic station. Thus, this kind of analysis should also be

applied seismic data as well as hydroacoustic data for offshore events near the coast.

Several other examples of presumed underwater chemical blasts were described in our earlier report (Baumgardt, 1999). However, we had no actual ground truth on the events, although the data was compelling that they were actually explosions. In order to validate that the technique, we need to test the method on actual underwater explosions for which ground-truth information is available. In the next section, we discuss the application of the method to the DTRA sponsored calibration explosions detonated in the Dead Sea in November of 1999.

SECTION 3
CEPSTRAL CHARACTERZATION OF THE NOVEMBER 8, 10, and 11 CALIBRATED UNDERWATER EXPLOSIONS IN THE DEAD SEA

In November of 1999, under the sponsorship of DTRA, three calibration chemical explosions were detonated in the Dead Sea by the Geophysical Institute of Israel. The main objective of the detonations was to calibrate seismic travel times at local and regional distances in the region. Each of the three explosions are at three different yields and at the same depth of 70 m. The event parameters for the explosions were (Gitterman et al, 1999; Gittermann and Shapira, 2000) are given in Table 2.

Table 2. Event Parameters for the three Dead Sea Calibration Events.

Date	Time (GMT)	Latitude	Longitude	Depth	M_L	m_b	Yield (kg)
1999/11/08	13:00:00.33	31.5330	35.4406	70 m	3.1	-	500
1999/11/10	13:59:58.21	31.5338	35.4400	70 m	3.6	-	2060
1999/11/11	15:00:00.79	31.5336	35.4413	70 m	3.9	4.1	5000

The detonations were timed with GPS with an accuracy of 5 milliseconds. The location accuracy was on the order of 50 m.

Our analyses of these events allowed the testing of our developed algorithm to known, calibrated explosions. In this section, we describe the cepstral analysis and inversion of these events in order to validate the accuracy of the method for estimating explosion yield.

For our analysis, we used data recorded at regional IMS stations available to us from the PIDC. The locations of the regional Israeli IMS stations at Eilat (EIL) and Meron (MRNI) that recorded the Dead Sea explosions are shown in Figure 13. The figure shows a map

with the great circle propagation paths from the locations of the explosions to the MRNI and EIL sites.

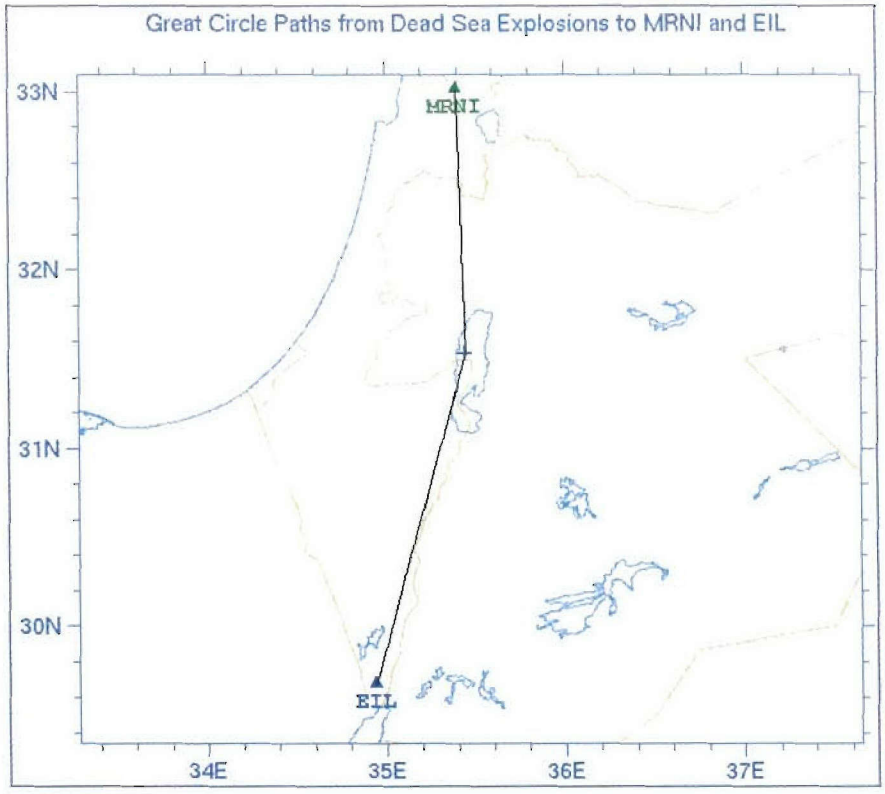

Figure 13. Great Circle Paths from Dead Sea Explosions to MRNI and EIL.

3.1 DEAD SEA EXPLOSION WAVEFORMS.

Figure 14 shows three-component MRNI waveforms for the November 9, 1999 explosion. Data from the EIL station was not available for this event. Waveforms recorded on the EIL and MRNI stations, for the November 10 and 11, 1999 explosions are shown in Figure 15 and Figure 16, respectively. Figure 17 shows the waveforms for both the EIL and MRNI stations for the November 11, 1999 explosion. The regional phase picks made by the PICD analysts are shown on each of the waveforms.

Figure 17 compares the Eilat, Israel (EIL) recordings of November 19 and November 11, 1999 Dead Sea explosions. Figure 18 compares the Meron, Israel (MRNI) recordings of

November 8, 10, and 11, 1999. These comparisons show that the relative amplitudes of the waveforms approximately correlate with the differing explosion yields.

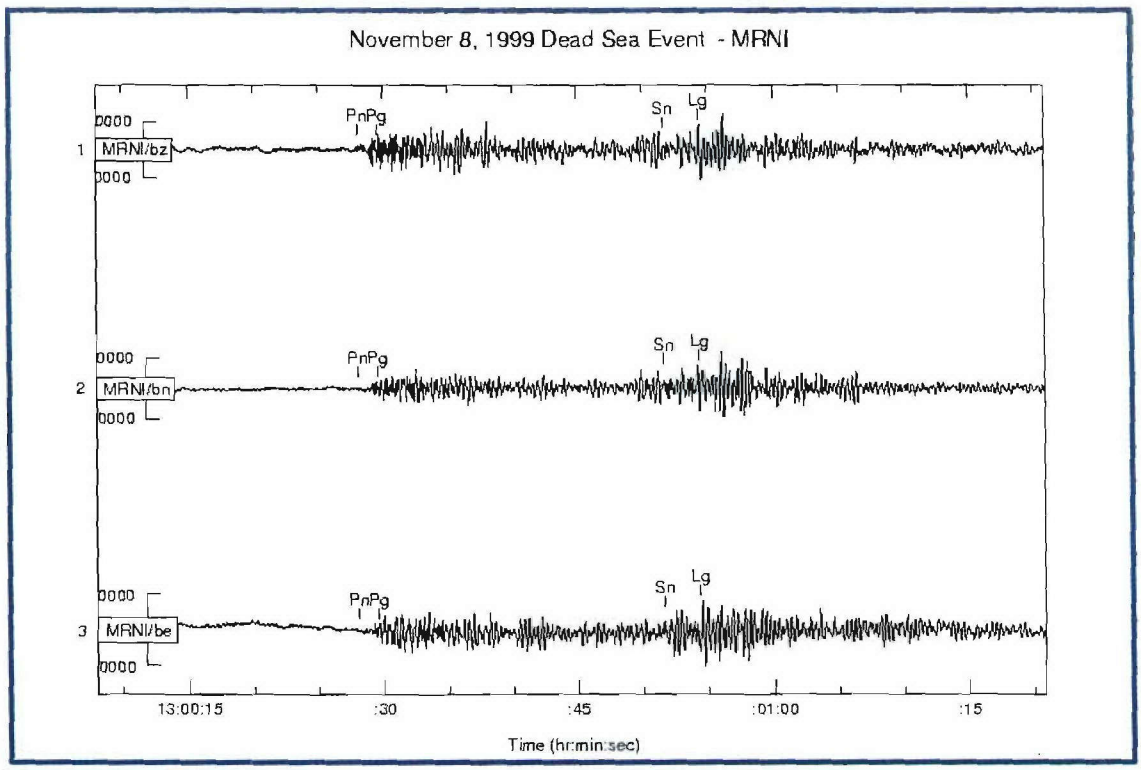

Figure 14. November 8, 1999 Explosion: Eilat, Israel (EIL), Three-Component Phase Picks.

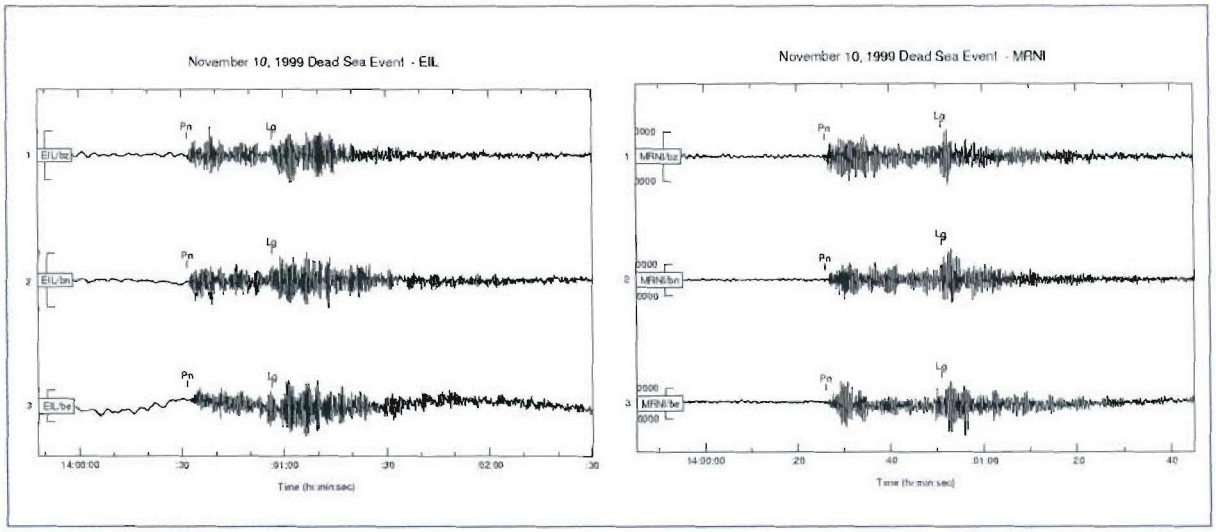

Figure 15. November 10, 1999 Explosion: (left) Eilat, Israel (EIL) Three-Component Phase Picks; (right) Meron, Israel (MRNI) Three-Component Phase Picks.

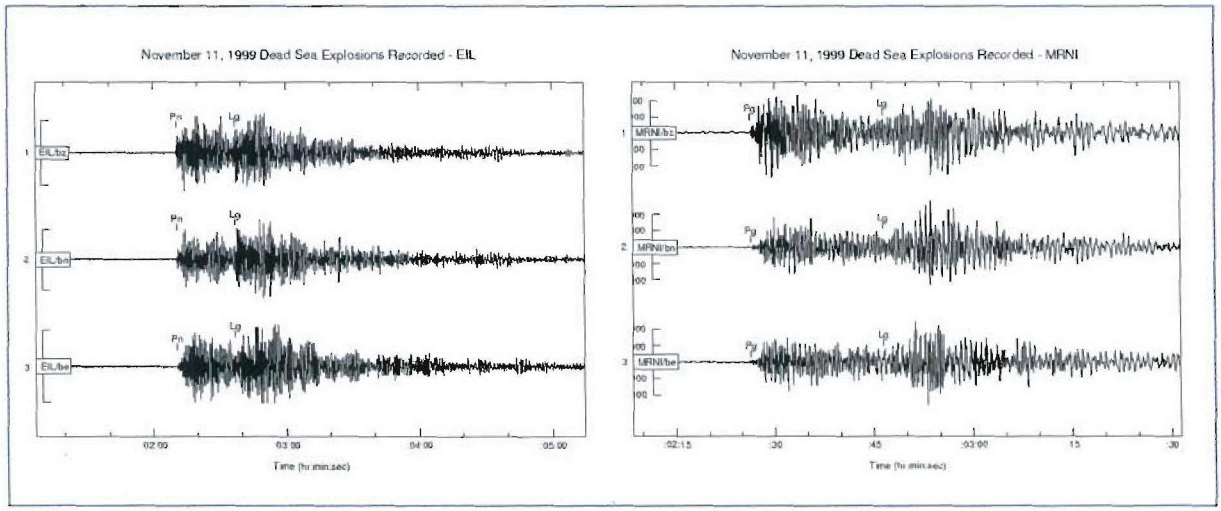

Figure 16. November 11, 1999 Explosion: (left) Eilat, Israel (EIL) Three-Component Phase Picks; (right) Meron, Israel (MRNI) Three-Component Phase Picks.

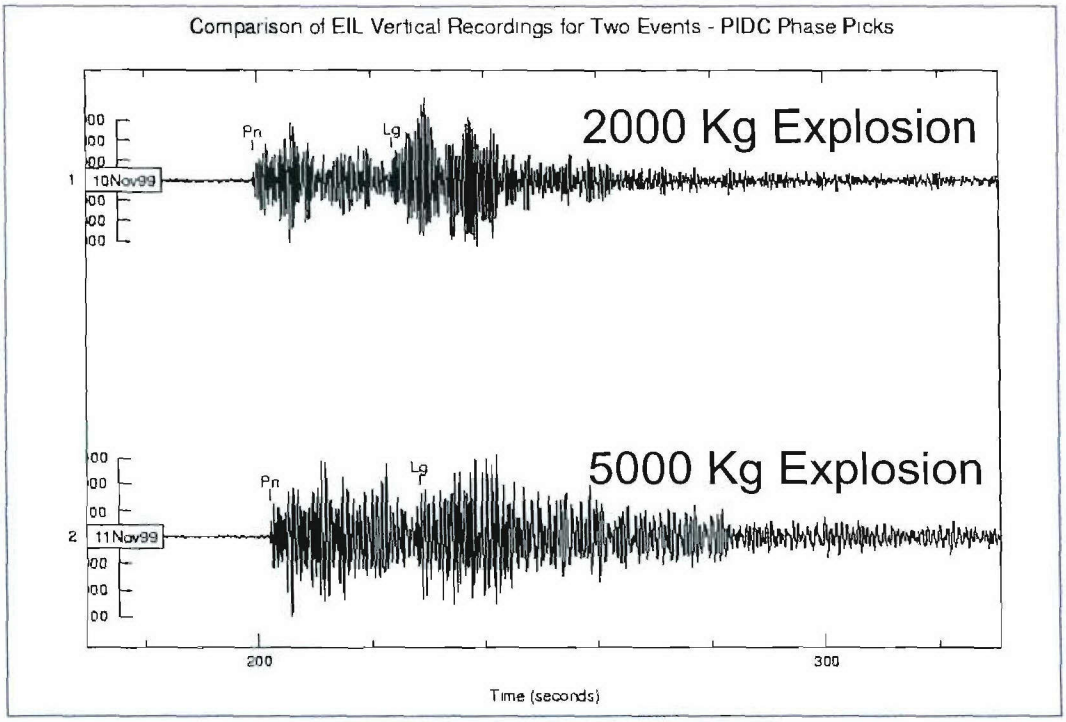

Figure 17. Comparison of EIL Vertical Recordings for November 10, and November 11, 1999 Explosions.

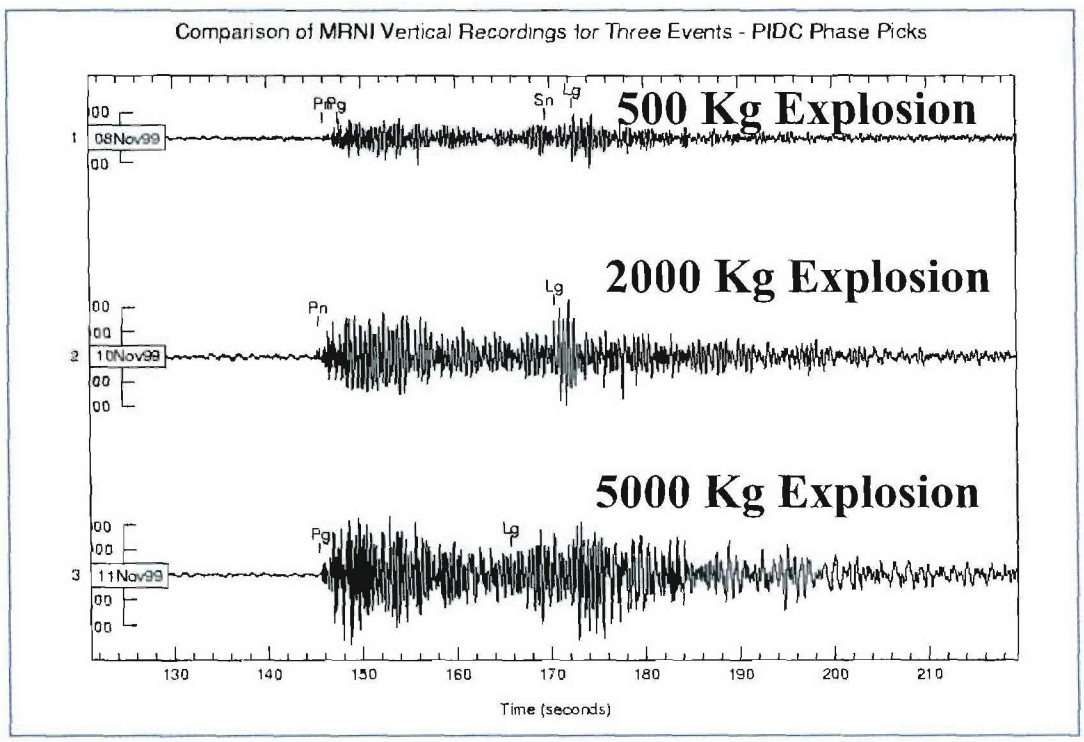

Figure 18. Comparison of MRNI Vertical Recordings of November 8, 10, and 11 Explosions.

3.2 SPECTRAL/CEPSTRAL ANALYSIS.

We use the same method for computing spectra and cepstra that was described in the earlier discussion of the Tromso. Figure 19 shows the vertical-component spectra for the different phases and background noise, for the phases recorded at the for the three Dead Sea underwater explosions. The spectra were computed on each of the individual three-component channels by windowing the phases, starting at the time picks shown in Figure 17 and Figure 18, using a 20-second Parzen window. Since no array data was available for these events, the spectra for each channel were averaged across the three component waveforms, which produce much smoother spectra than the individual channel spectra. The spectra have very distinct spectral modulations or "scalloping" in all phases with a strong spectral peak at about 2.5 Hz. None of these features appears in the noise.

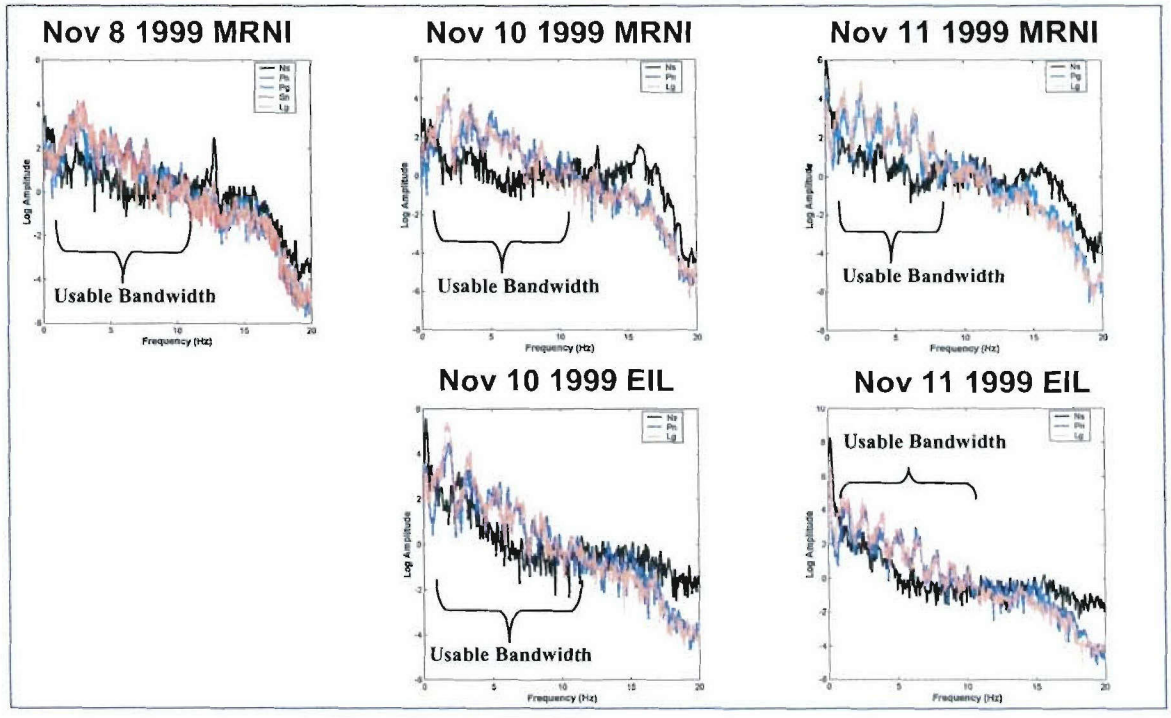

Figure 19. Averaged spectra for each of the recordings of the Dead Sea underwater blasts.

Figure 19 also shows the "usable bandwidth" of each of the signal. The "usable bandwidth" is the portion of the spectrum where the phase spectral amplitudes are above the noise levels. Within the usable bandwidth in each case, the spectral modulations are evident, although they are stronger for the larger explosions on November 10 and 11 than for the November 8 explosion. It is obvious from Figure 19 that the "usable bandwidth" is considerably smaller than the overall bandwidth of the data. In order to apply the same cepstral analysis as that described in the previous section for synthetic data, spectral shaping is required.

We use the same technique for computing cepstra of the Dead Sea events as we used for the Tromso events, which is expression (2.9). Figure 20 shows the spectra (left) and cepstra (right) for the MRNI recordings of the November 8, 1999 explosion. In this figure, both the spectra and the cepstra have been shifted for display purposes. This explosion was the smallest of the three and has the weakest spectral modulations, and we only have data from this one station. Figure 21 and Figure 22 show the composite spectra for the November 10 and 11 explosions, respectively. For these two events, the spectra for all channels of MRNI and EIL have been averaged.

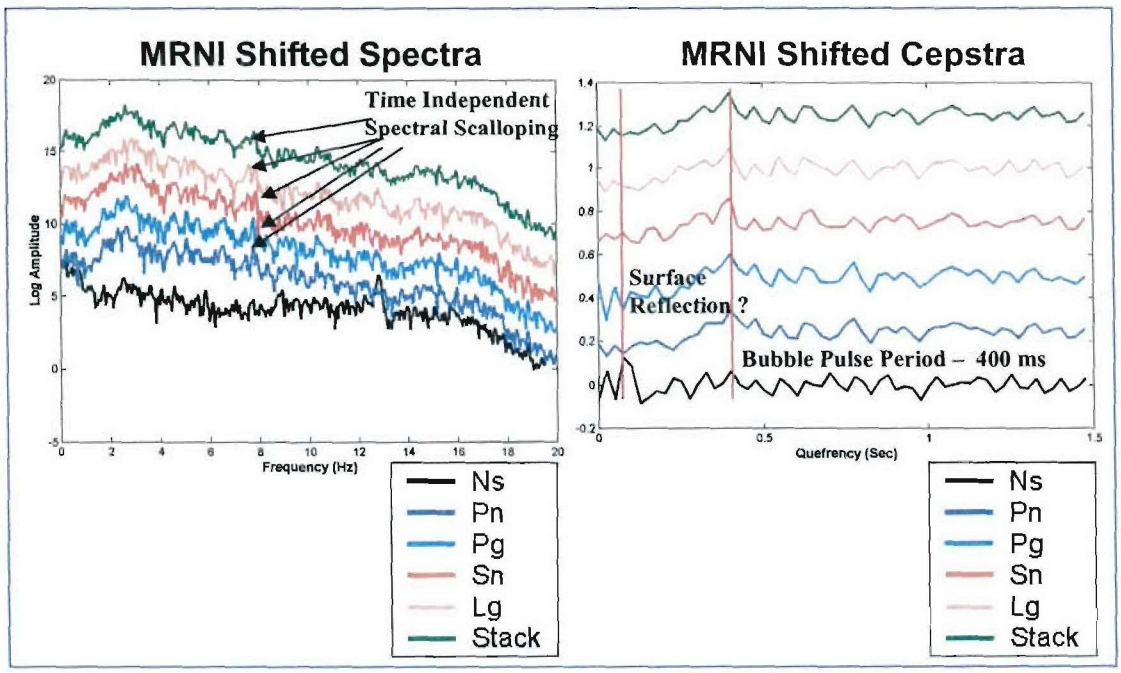

Figure 20. Spectra and cepstra for the November 8, 1999 explosion.

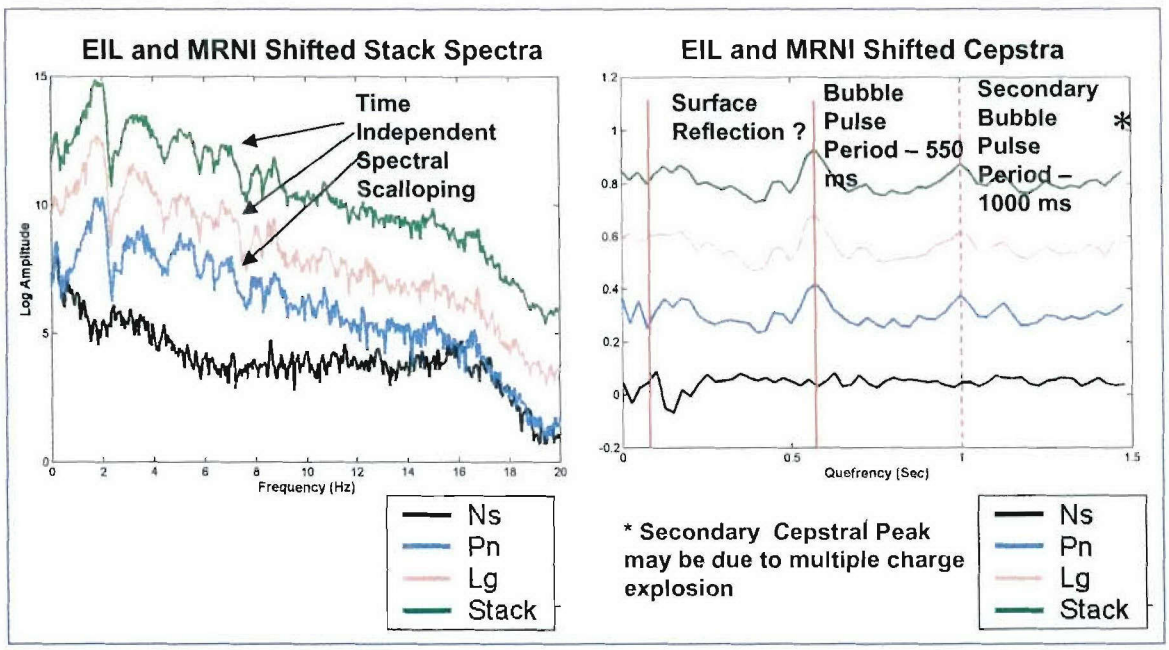

Figure 21. Averaged MRNI and EIL spectra and cepstra for the November 10, 1999 explosion.

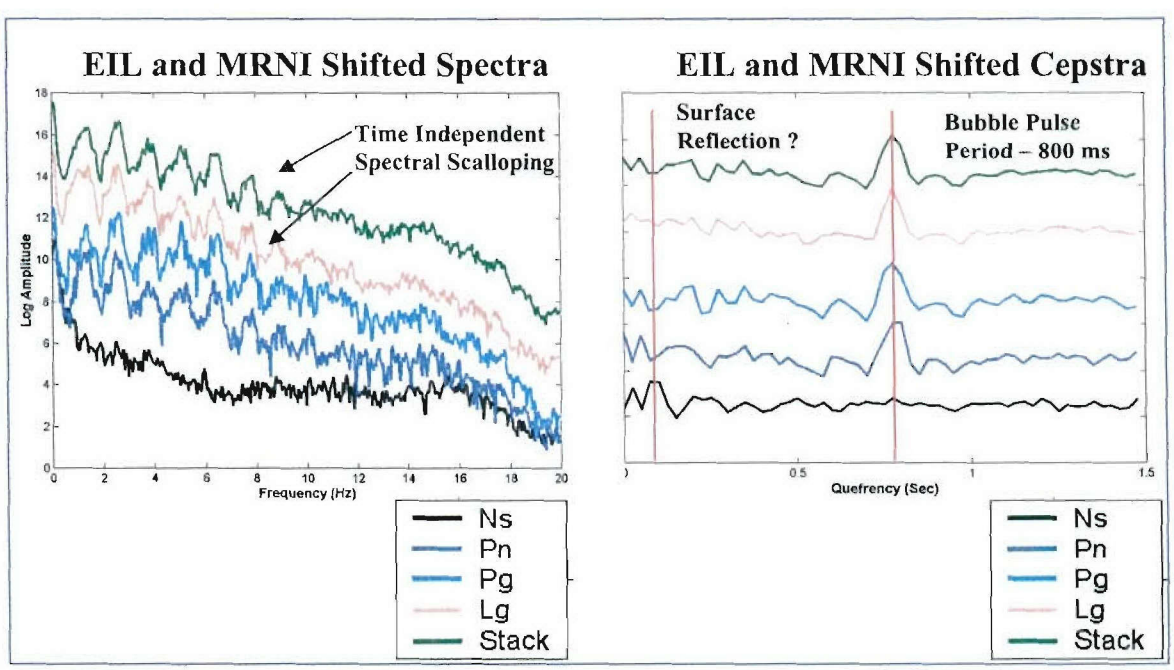

Figure 22. Averaged MRNI and EIL spectra and cepstra for the November 11, 1999 explosion.

These plots show the spectra and cepstra for each phase that was identified and the background noise sample before the *Pn*, and a composite stack of all the phase cepstra for

each event. The strongest modulations were observed for the November 10 and 11 events, as might be expected since they are the largest. The larger the explosion, the higher the signal relative to the noise in the usable bandwidth, the stronger the spectral modulations, and the larger the cepstral peaks. Also, the period of the primary peak, which as associate with the bubble pulse, scales with the size of the explosion. The November 10 event appears to have peaks that may either be caused by two bubble pulses or multiple explosions. This event did have a small secondary charge but it was only about 60 kg. We now apply the cepstral model and inversion algorithm on the composite stack cepstrum of each event.

3.3 CEPSTRAL MODELING AND INVERSION.

We have first considered a simple exhaustive search method, where the parameter space of blast yield and depth in the water is gridded and synthetic cepstra are computed for each grid point, as we did for the Tromso event in the previous section. However, for the match statistic, we have used the L1 norm rather than the correlation coefficient to find the best matching synthetic cepstrum to the observed cepstrum. The L1 norm is the absolute value of the difference between the observed and synthetic cepstrum, which would be zero for a perfect match. Thus, in the exhaustive search, we seek the parameters of explosion depth and yield that maximize the 1.0 – L1 norm.

The result of the exhaustive search solution to the fit to the November 8 explosion is shown in Figure 23. Although a peak is found that gives a yield of 650 kg, close to the expected value of 500 kg, the peak is not well resolved.

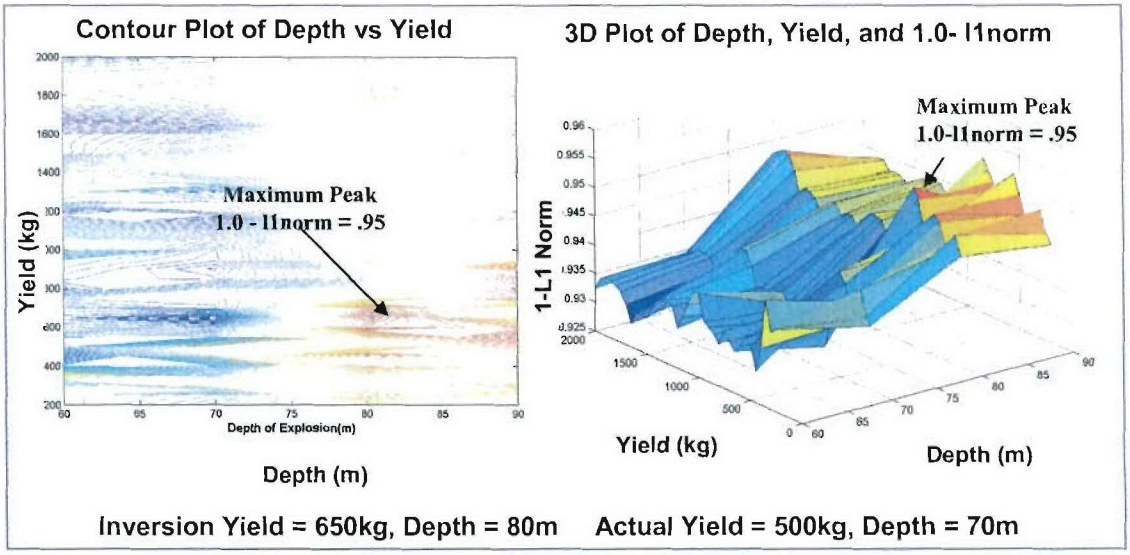

Figure 23. L1 norm exhaustive search solution to the November 8, 1999 event. The peaks indicate the best matching yield and depth on the contour plot (left) and surface plot (right) for the 1 – L1 norm.

Figure 24 (left) shows the sensitivity of the data to this solution, where the 1 – L1 norm coefficient is plotted as a function of yield for a depth of 80 m. The maximum peak was 650 kg. The overall broad peak is about 140 kg in width, which provides an estimate of the resolution of the method to yield; thus, a better estimate of yield is 650 kg ± 140 kg.

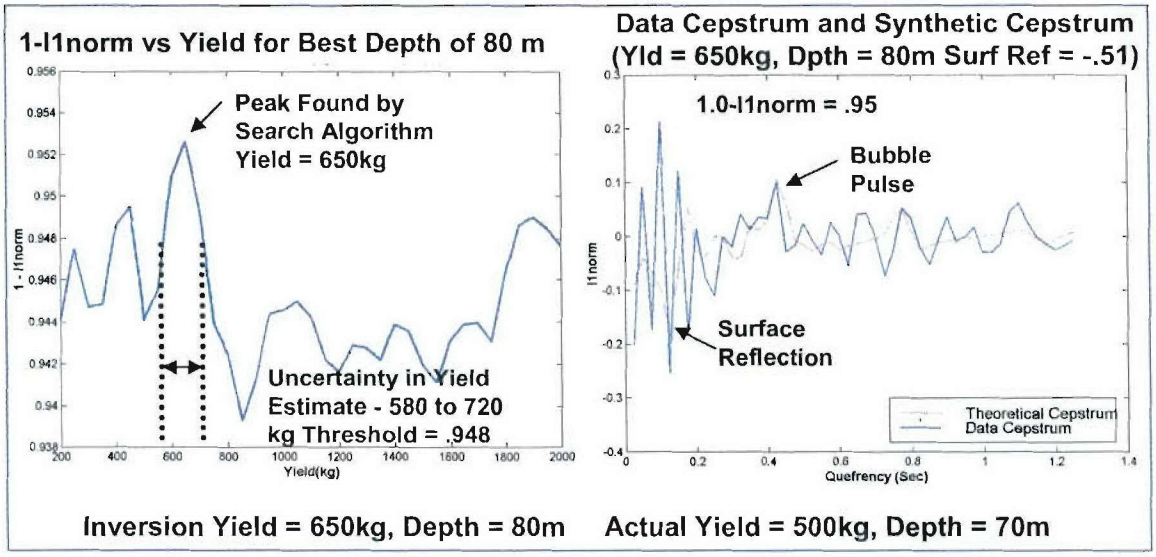

Figure 24. November 8, 1999: (left) cross section of cepstral fit surface; (right) comparison of synthetic cepstrum with stack MRNI data cepstrum.

Figure 24 (right) shows a direct comparison of the observed stack cepstrum and the best-matching synthetic cepstrum. This comparison shows that, although the match is not perfect, the theoretical cepstrum matches the overall shape of the observed cepstrum, but not the details. The primary feature that drives the match correlation is the position of the bubble pulse peak. It should be noted, however, that the depth is not well constrained. Also, there appears to be significant low-quefrency noise due the processing artifacts.

The solution for the November 10, 1999 event is shown in Figure 25. This solution produced multiple peaks in the match surface. The maximum peak gave a yield of 4000 kg, which is considerably larger than the true yield of 2000 kg. However, it should be noted that the depth of the estimate of the maximum peak is 110 m, which is considerably greater than the true depth of 70 m. The secondary peaks correspond to lower depths, including one at about 80m.

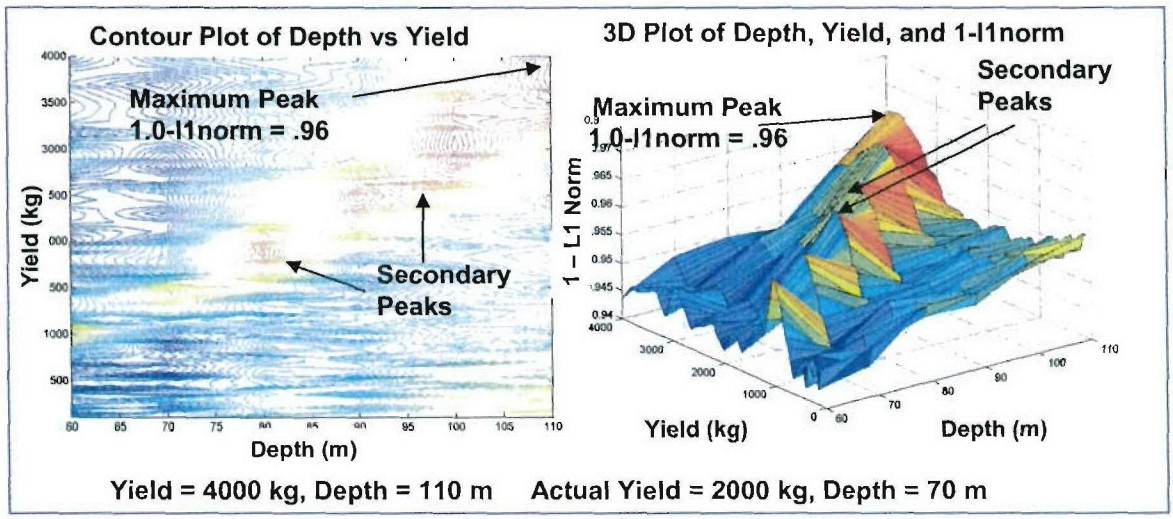

Figure 25. L1 norm exhaustive search solution to the November 10, 1999 event. The peaks indicate the best matching yield and depth on the contour plot (left) and surface plot (right) for the 1 – L1 norm.

Figure 26 shows the sensitivity to yield where the 1 – L1 Norm coefficient is plotted as a function of yield for the depth of 80 m. The maximum peak was at 1950 kg, which is closer to the true value. The overall broad peak is about 700 kg in width, which gives a yield estimate, with uncertainty, of 1950 kg ± 350 kg.

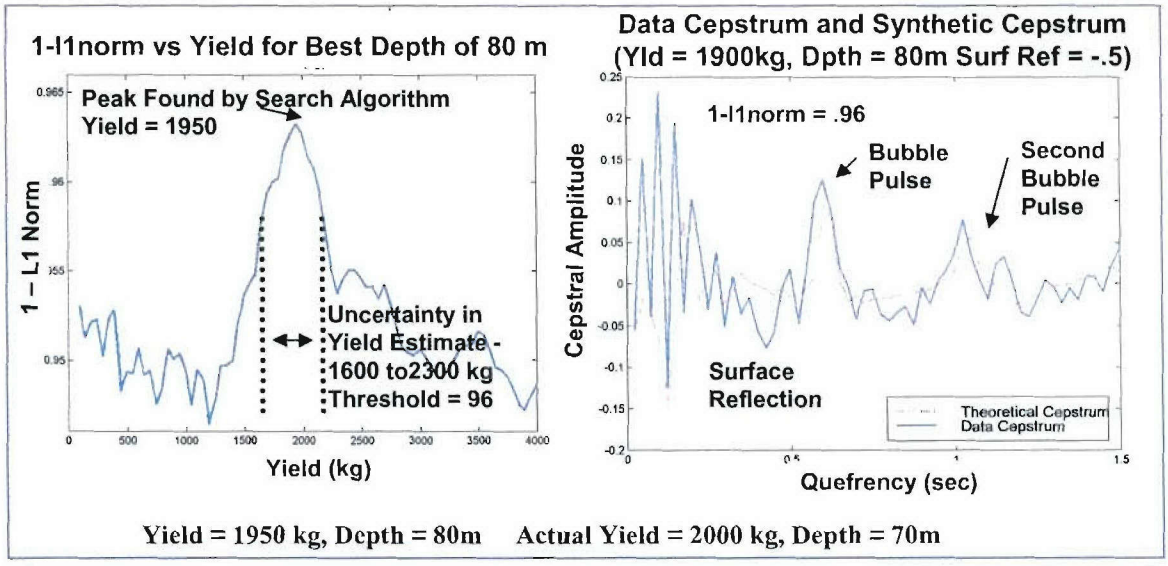

Figure 26. November 10, 1999: (left) cross section of cepstral fit surface; (right) comparison of synthetic cepstrum with stack EIL and MRNI data cepstrum.

Figure 26 (right) shows a direct comparison of the observed stack cepstrum and the best-matching synthetic cepstrum at depth of 80 m. This comparison shows that a double-bubble pulse gives a good match of the essential features. Thus, the complexity in the fitting surface, caused by the multiple peaks, can be explained by a double bubble-pulse feature in the cepstrum. Again, the depth appears to be poorly constrained, with significant low-quefrency noise evidently caused by processing artifact.

Figure 27 shows the solution for the November 11, 1999 explosion plotted as a 3D contour (left) and surface plot (right). Both displays have a distinct peak in the correlation, with a maximum 1 – L1 Norm coefficient of 0.98, corresponding to a water depth of 80 m and yield of 4200 kg. The secondary peak of .976 is also shown, which gives a yield closer to the expected value of 5000 kg and but the depth is 90 m.

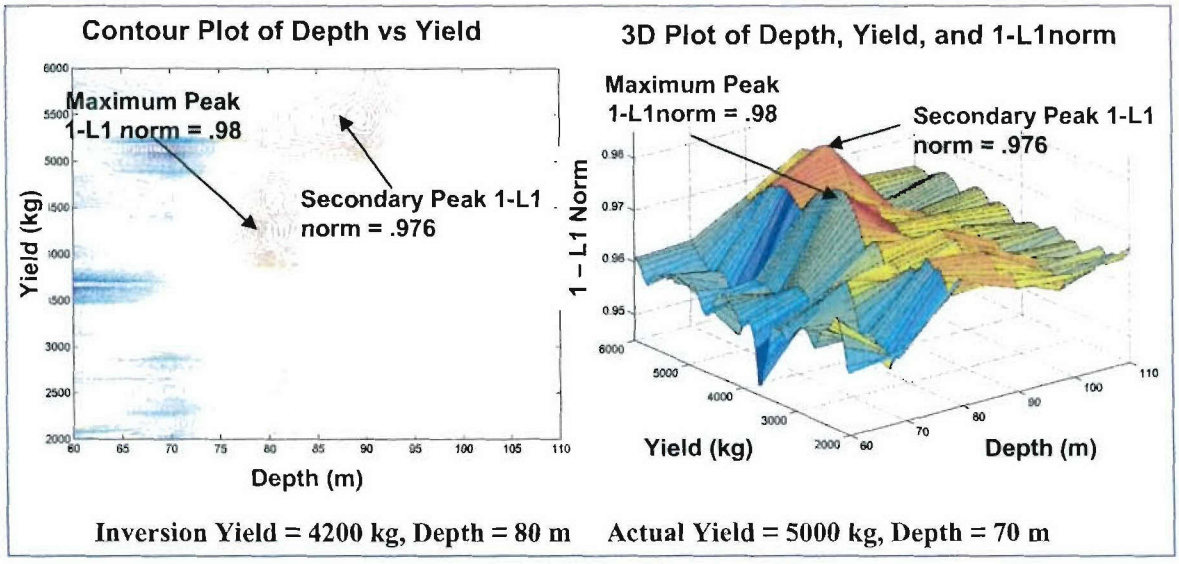

Figure 27. November 11, 1999: Example of exhaustive search for best matching synthetic cepstrum to observed cepstrum 1 – L1 Norm, (left) contour plot (right) surface plot.

The sensitivity to yield is shown in Figure 28 (left), where the maximum 1 – L2 norm correlation is plotted as a function of yield for the depth of 80 m. The maximum peak was at 4200 kg. However, the overall broad peak is about 800 kg in width, which gives an estimate of yield and uncertainty of 4200 kg ± 500 kg. Figure 28 (right) shows a direct comparison of the observed stack cepstrum and the best-matching synthetic cepstrum. Note that there is a very strong negative peak, which evidently comes from the surface reflection. This negative peak provides the constraint on depth.

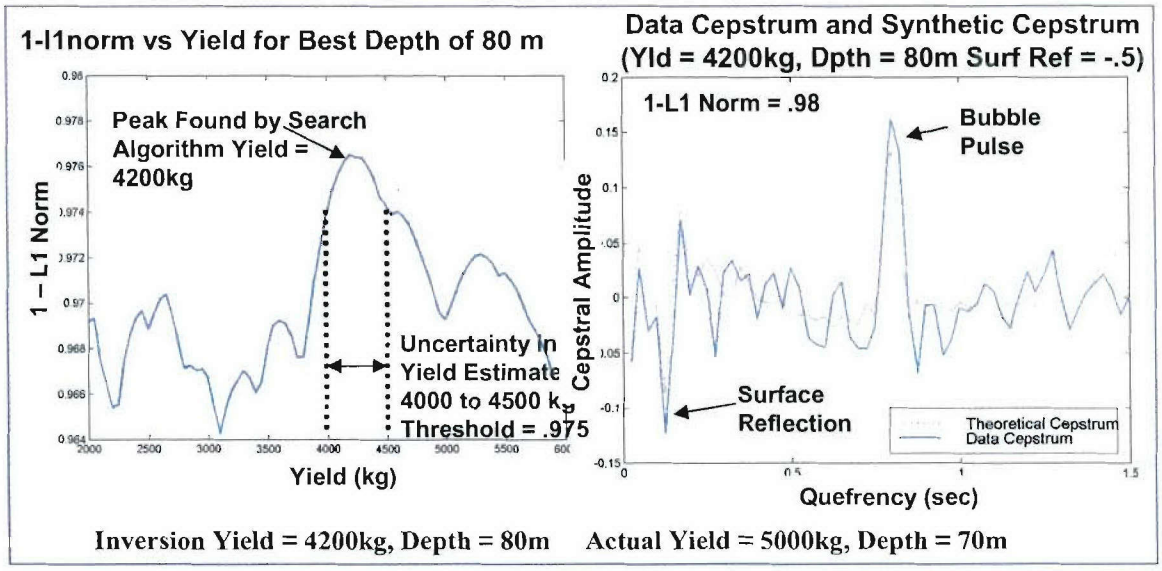

Figure 28. November 11, 1999: (left) cross section of cepstral fit surface; (right) comparison of synthetic cepstrum with stack EIL and MRNI data cepstrum.

The negative surface reflection is about 0.15 seconds. We assumed a water velocity of 1771 m/sec, which is higher than the oceanic value of about 1500 m/sec because of the high salinity of the Dead Sea (Gitterman et al, 1999). This time delay is consistent with a two-way travel time through a water column of about 80 m, which was found by the search algorithm. Note that this would be the depth of the explosion below the water surface. The actual charge depth was 70 m. As noted earlier, knowledge of the water depth is not actually required to infer the explosion depth in the water since the reflection from the surface is by far the strongest signal.

For all the cepstral matches described above, we have had to assume a very low surface reflection coefficient of –0.5, considerable lower than the expected value of –0.90. This lower value is required to match the negative trough amplitude. A coefficient of –0.9 would make the synthetic trough almost twice as large as the observed trough. The low amplitude of the trough in the model cepstrum is evidently caused by low correlation of the primary explosion pulse and the reflection. Because of the shallowness of the explosion, we are barely able to resolve the reflection with the limited bandwidth of the data. Thus, this poor resolution may cause the trough to be weaker than observed theoretically.

Regardless of the value assumed for the surface reflection coefficient, only the time of the surface-reflection trough in the data needs to be matched to the model, not the amplitude itself, in order to estimate depth.

3.4 DOWNHILL SIMPLEX SEARCH ALGORITHM.

The exhaustive grid-search cepstral matching algorithm that was applied previously has the disadvantage of being very time consuming, and in its current implementation, we could only vary the yield and depth parameter of the model. A number of other important parameters, such as water depth, surface reflection coefficient, and bottom reflection coefficients, had to be fixed. A faster algorithm that can perturb more parameters would be more desirable.

Here, we have applied the downhill simplex method, originally developed by Nelder and Mead (1965), for multidimensional search of a parameter space to minimize a functional. Given an N dimensional parameter space, the algorithm searches the complex topography of the function surface in the downhill direction to minimize a goodness of fit parameter. In our case, the function is defined as the match statistic (e.g., correlation coefficient or 1-L1 norm), $R[C_o, C_{th}(x)]$, between the observed cepstrum, C_o, and the theoretical cepstrum, C_{th}, and x is an N dimensional vector of parameters for the theoretical cepstrum. We desire parameters for a model that minimize the function $\varepsilon = 1 - R[C_o, C_{th}(x)]$.

Very briefly, the downhill simplex algorithm finds the minimum of the functional of an N dimensional surface by first defining a simplex with $N+1$ points. Given a starting point $\mathbf{P_o}$, the N other points are taken as

$$\mathbf{P_i} = \mathbf{P_o} + \lambda\, \mathbf{e_i}$$

where the $\mathbf{e_i}$'s are N unit vectors, and where λ is a constant that defines the guess values initial length scale. The downhill simplex method then takes a series of steps, moving from the point of the simplex where the function, ε, is largest through the opposite face of the simplex to a lower point. The method tries to find a valley and shrinks the simplex to

better define the minimum in the valley.

In our initial application of the algorithm, we allowed three parameters to be perturbed in the model -- depth, yield, and surface reflection coefficient. The reason surface reflection coefficient was included as a parameter is that lower values than -0.9 were needed to fit the amplitude of the negative peak in the cepstrum. However, given that we are using the cepstral correlation as the goodness-of-fit functional, it is not really necessary to have an exact match in the amplitudes of the peaks in order to get a high correlation. Still, as an experiment with the method and to find out what is necessary to get the synthetic cepstra to look more like the observed cepstra, we have allowed the surface reflection coefficient to vary.

The downhill simplex algorithm, originally developed by Nelder and Mead (1965), computes a multidimensional search of depth, yield, and surface reflection coefficient parameter space to maximize the correlation between the synthetic cepstrum and the data cepstrum. Figure 29 (left) shows a plot of the parameter space, consisting of yield and depth on the horizontal axes, and surface reflection coefficient on the vertical axis. Each 'x' symbol marks a point in the parameter space that was checked by the downhill simplex method. The arrow indicates the point that the algorithm found as the minimum of the L1 norm match statistic. This is the point where the simplex algorithm collapses in on a minimum value. The right plot of Figure 29 shows the best match, found by the downhill simplex optimization method, between the data cepstrum and the synthetic cepstrum. The match is good overall, although the height of the synthetic bubble pulse is not as big as that of the data cepstrum. The downhill simplex algorithm chose a yield of 4200 kg, and a depth of 80 m. The actual yield was 5000 kg, at a depth of 70 m.

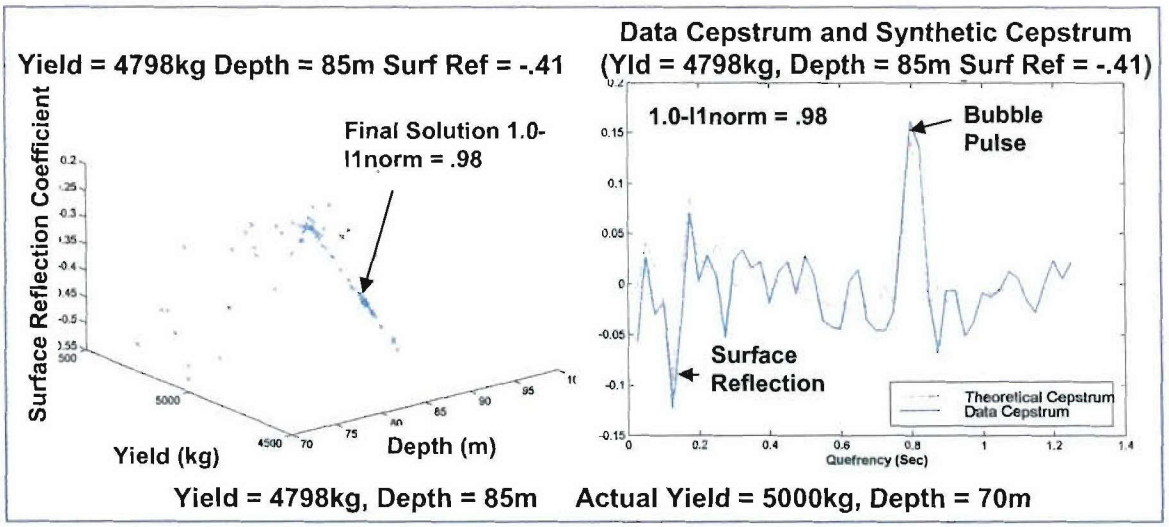

Figure 29. November 11, 1999: (left) downhill simplex optimization method; (right) comparison of synthetic cepstrum with highest correlation.

3.5 CONCLUSIONS.

The limited bandwidth of the IMS regional stations was not sufficient to resolve the 70 m depth of the explosions. However, we have shown that the cepstra for the explosions are consistent with the known depth of 70 m. The November 10, 1999 event appeared to have two bubble pulses, or perhaps to detonations. Lack of constraint on depth for this event produced a strong tradeoff between depth and yield. The bubble pulse period was consistent with the actual yield of 2000 kg. It was found that depth and yield could not be uniquely constrained by the data alone. The best depth and yield estimate, as might be expected, as found for the largest 5000 kg explosion. The results show good agreement with the know depths and yields, and suggest that the cepstrum inversion technique is a useful method for estimating depth and yield for underwater explosions. For the two larger explosions, we have demonstrated that the method can estimate yield with an accuracy of 10 to 15 %.

SECTION 4
UNDERWATER EXPLOSIONS IN THE BARENTS SEA – THE OCTOBER 23, 1997 MURMANSK AND AUGUST 12, 2000 KURSK EVENTS

This section presents analysis of recent events in the Barents Sea presumed to be underwater explosions. The first is a Russian underwater chemical blast detonated near Murmansk on October 23, 1997. The second may have been associated with the Kursk submarine sinking on August 12, 2000. The Murmansk event was described in a note submitted to DTRA (Baumgardt, 1998) in which it was suggested that the event be retained in a database for special event analysis of subsequent events in the region. The August 12, 2000 Kursk event, which was also described in another technical memo submitted to DTRA (Baumgardt and Freeman, 2000b), is an example of the kind of special event that would benefit from having this kind of reference event available for analysis. Other studies of this event have been published subsequent to ours (Koper et al, 2001; Gitterman, 2002), which we will discuss later in this section. In this section, we first present our reanalysis of the Murmansk event. We then discuss the August 12, 2000 event to show that the cepstral characterization of the events clearly shows that they are consistent with being underwater explosions of different yield and depth.

4.1 OCTOBER 23, 1997 MURMANSK EXPLOSION ANALYSIS.

The Murmansk explosion of was small, with a magnitude less than 2.5, and was too small to be reported in the REB of the PIDC. However, four seismic stations, ARCES, FINES, Spitzbergen, and NORES, recorded regional seismic phases from the event. Figure 30 shows a record section of the stations that recorded the event. Regional phases *Pn*, *Sn*, and Lg were recorded at each of the stations. Since no location was available, the event was relocated using the travel times for these regional phases. As in the case of the Tromso event (Section 1.0), we used the IASPEI91 and Baltic Shield model to locate the event. In addition, we also obtained data from KEV to relocate the event. The estimated locations, using different phases and travel-time curves, are shown in Figure 31.

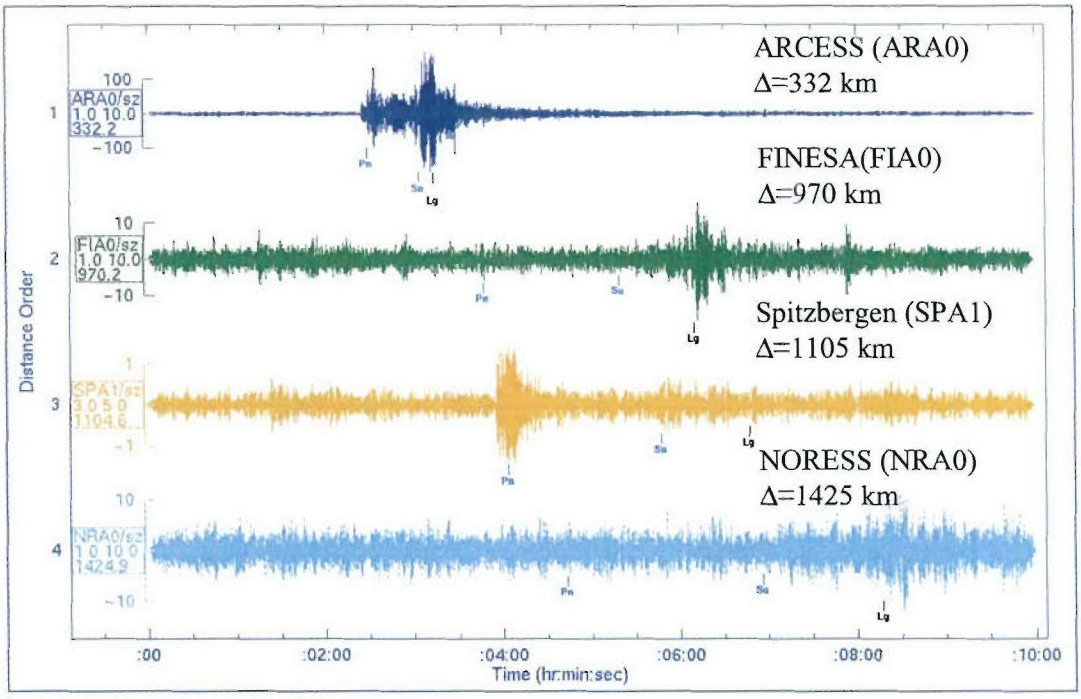

Figure 30. Waveforms recorded from the October 23, 1997 explosion.

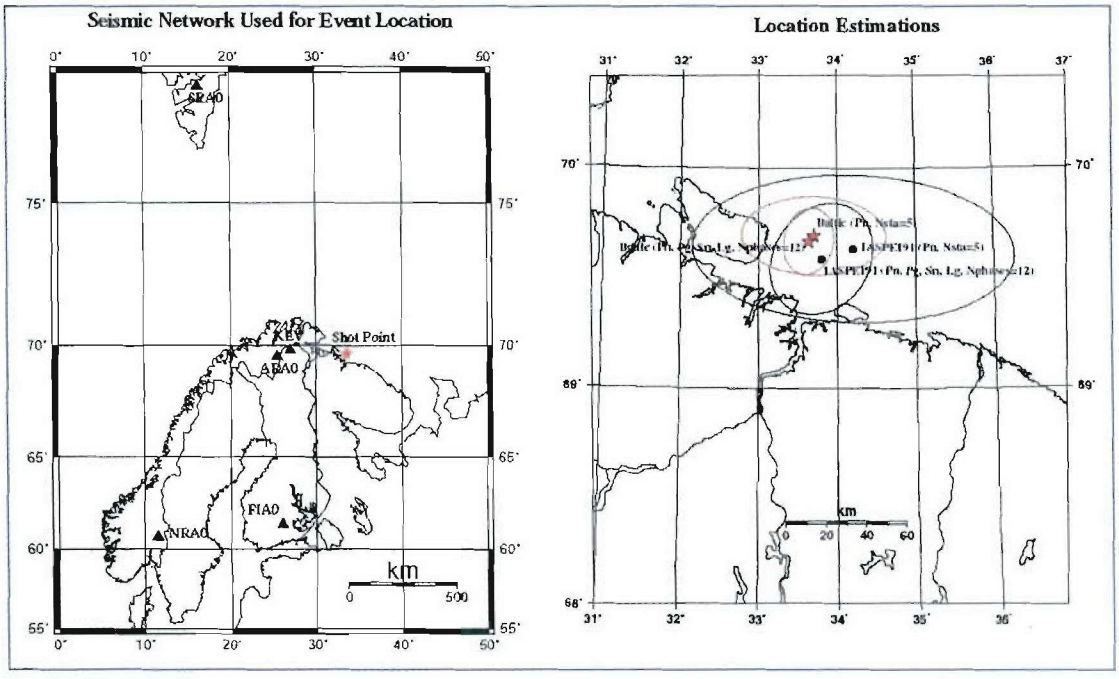

Figure 31. (Left) Map showing locations of the shot point and the stations that recorded phases from the October 23, 1997 event. (Right) Location estimates and error ellipses for the event.

The locations in Figure 31 (right) all place the event offshore, although some of the error ellipses overlap land. The best location, using *Pn* arrivals and the Baltic Shield travel-time model, has the smallest error ellipse that does not overlap land.

Figure 32 shows array-stacked spectra computed for the regional phases shown in Figure 30. In each case, the spectra have been corrected for the instrument. Strong spectral modulations are apparent in the spectra of the phases but not in the noise, except for those spectra that are near or below the noise level. Signal-to-noise ratios are obviously best for the ARCES array, where the entire modulation pattern is above the noise level.

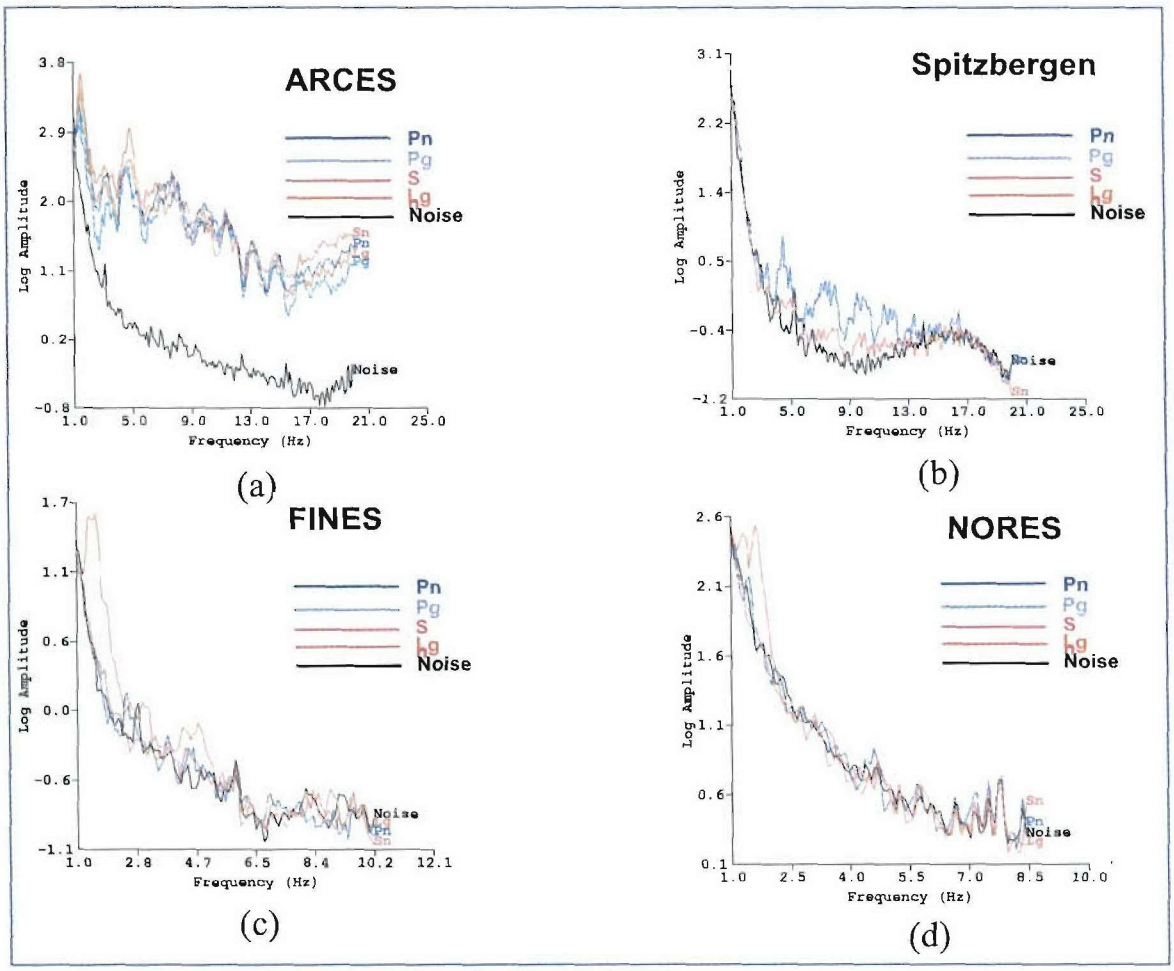

Figure 32. Array stacked spectra, corrected for instrument, for regional phases from the October 23, 1997 Murmansk event recorded at regional arrays. (a) ARCES, (b) Spitzbergen, (c) FINES, and (d) NORES.

Because ARCES recorded the highest signal to noise ratios, we chose to model to try to model this station. Figure 33 shows the spectra computed from the array-averaged spectra for ARCES, using techniques discussed earlier, and our initial interpretation of the cepstral features.

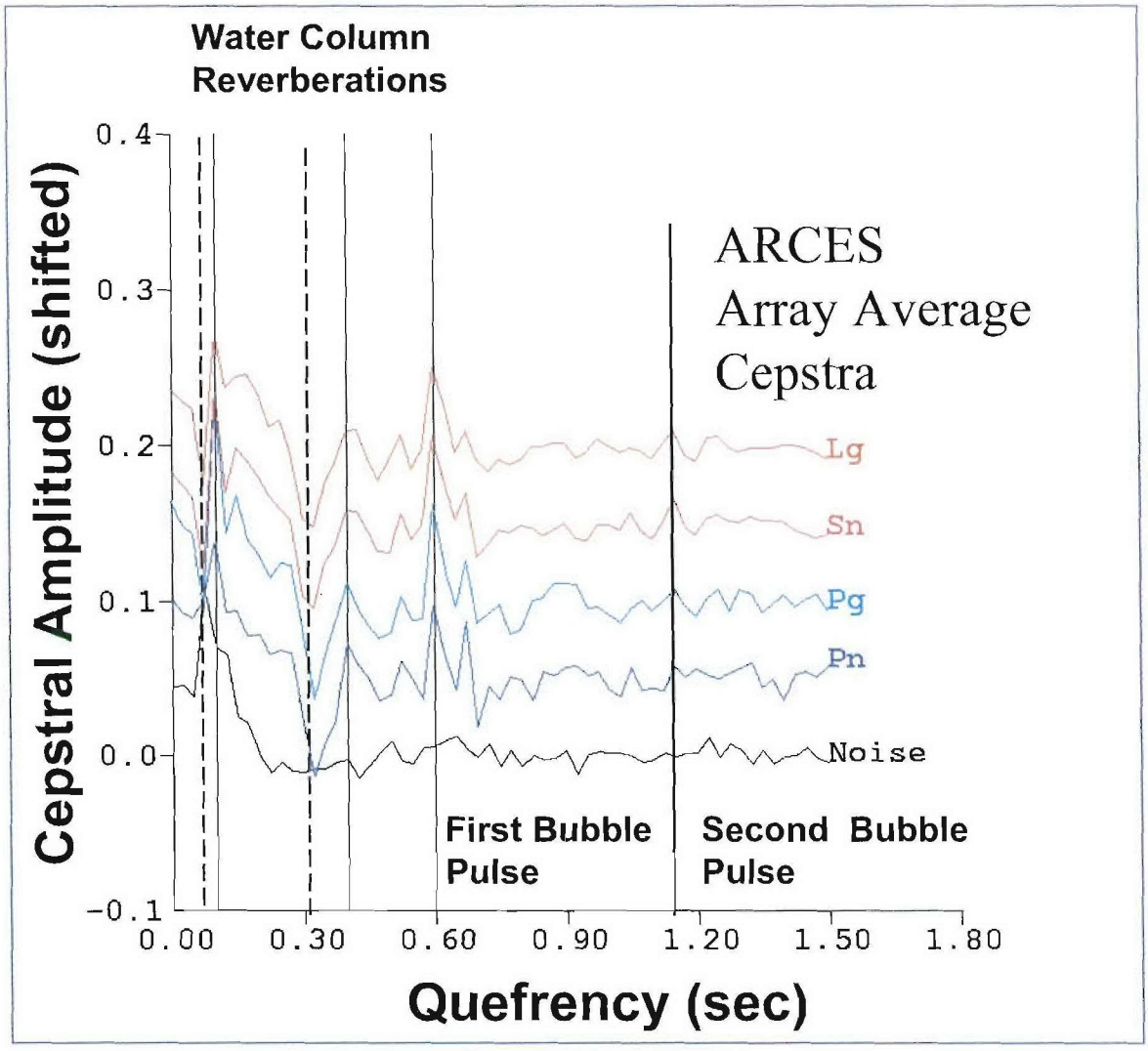

Figure 33. ARCES cepstra for each phase computed from array-stacked spectra. Cepstra have been shifted for display purposes.

The cepstra are very complicated, with a very evident negative trough at about 0.32 seconds. Assuming this to be the two-way acoustic travel time gives a depth of about 240 m, assuming a sound propagation speed in water of 1480 m/sec, which is close to the known bathymetric water depths in the region, which are about 200 m. However, multiple posi-

tive peaks are observed which we have interpreted as being caused by multiple bubble pulses. The question is whether these assumed bubble-pulse delay times can be accommodated with the 220 m depth in the water.

In this study, we modeled the stack of the phase cepstra at ARCES using trial and error to check the interpretation of the peaks in Figure 33. First, we considered the possibility that the first peak at 0.7 seconds is a bubble pulse peak. The model construction for this is shown in Figure 34.

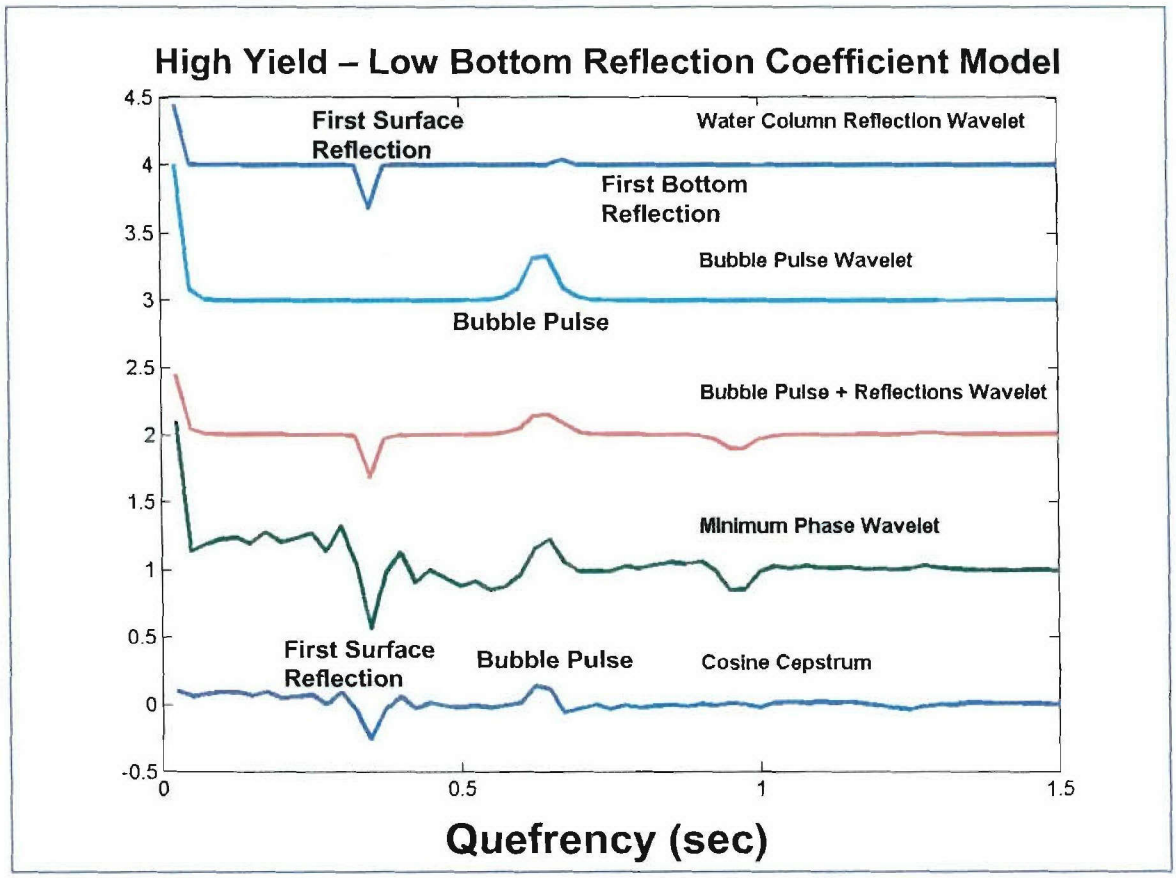

Figure 34. Model construction for a high-yield interpretation of the Murmansk explosion cepstra at ARCES. Surface reflection coefficient = -0.6, bottom reflection coefficient = 0.2, water depth = 240 m, depth of explosion = 240 m, yield=27,000 kg.

Figure 35 compares the synthetic cepstrum for the high-yield model with stack of all the phase cepstra at ARCES. The large negative peak at about 0.32 seconds is matched well by the surface reflection for 240 m depth. However, to match the large peak at 0.7 sec-

onds with a bubble pulse peak, the explosion yield must by 27,000 kg, which is an order of magnitude larger than the largest Dead Sea explosion. If this yield is right, the magnitude of the event should be over 4.0. However, this event had a very low magnitude of less than 2.5, since it was not reported by PIDC in the REB. Thus, we are forced to reject this model.

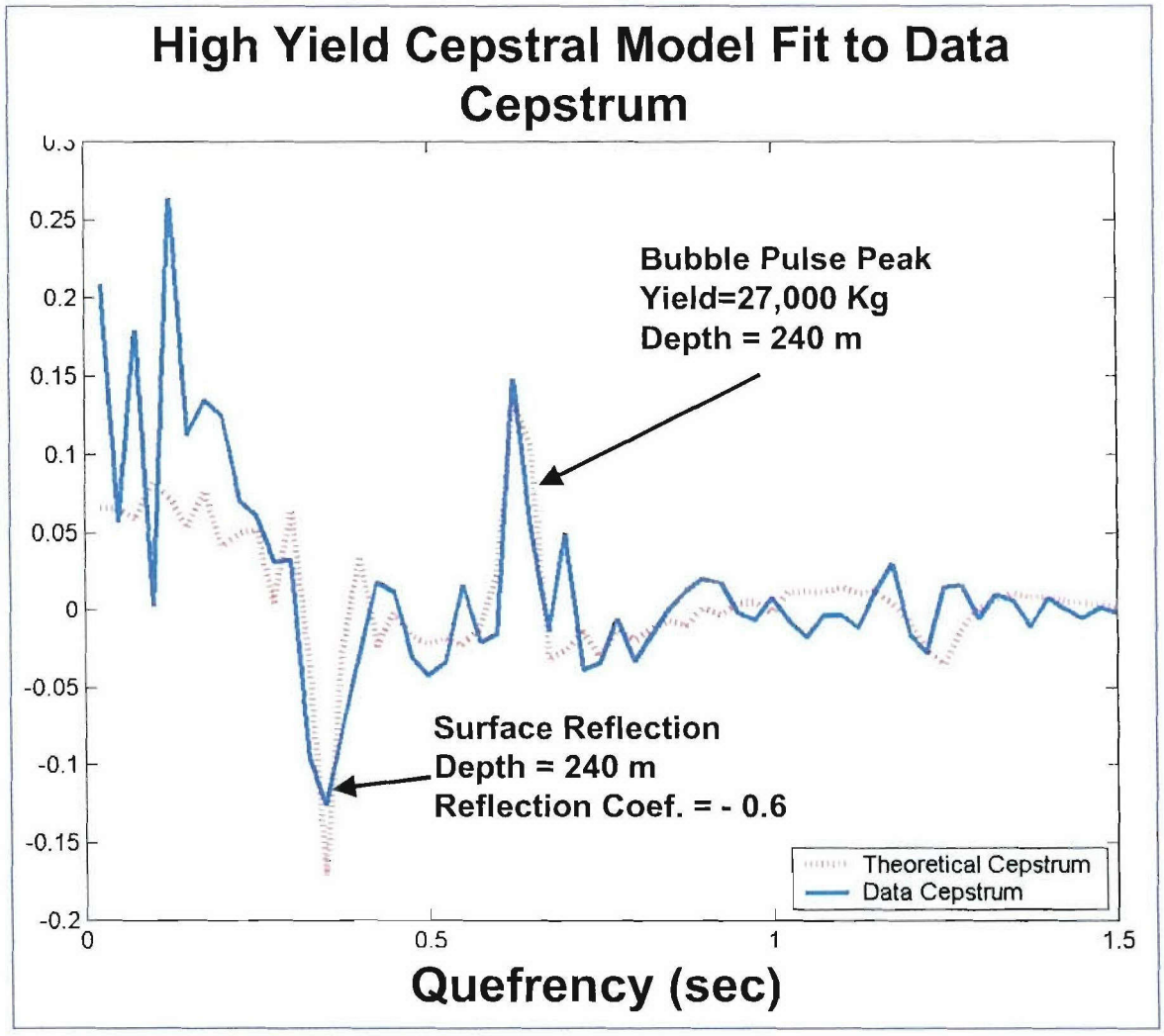

Figure 35. Comparison of the high-yield cepstral model with the stack of all the phase cepstra at ARCES.

We note that there is an unexplained peak at about 0.2 seconds which might actually be the bubble pulse. Thus, we consider the possibility that this peak is the bubble pulse and the peak at 0.7 seconds is due to a water reverberation. Figure 36 shows a second, low yield model. In this model, we have reduced the yield to 200 kg and increased the bottom

reflection coefficient from 0.2 to 0.6. Also, we consider two bubble pulses.

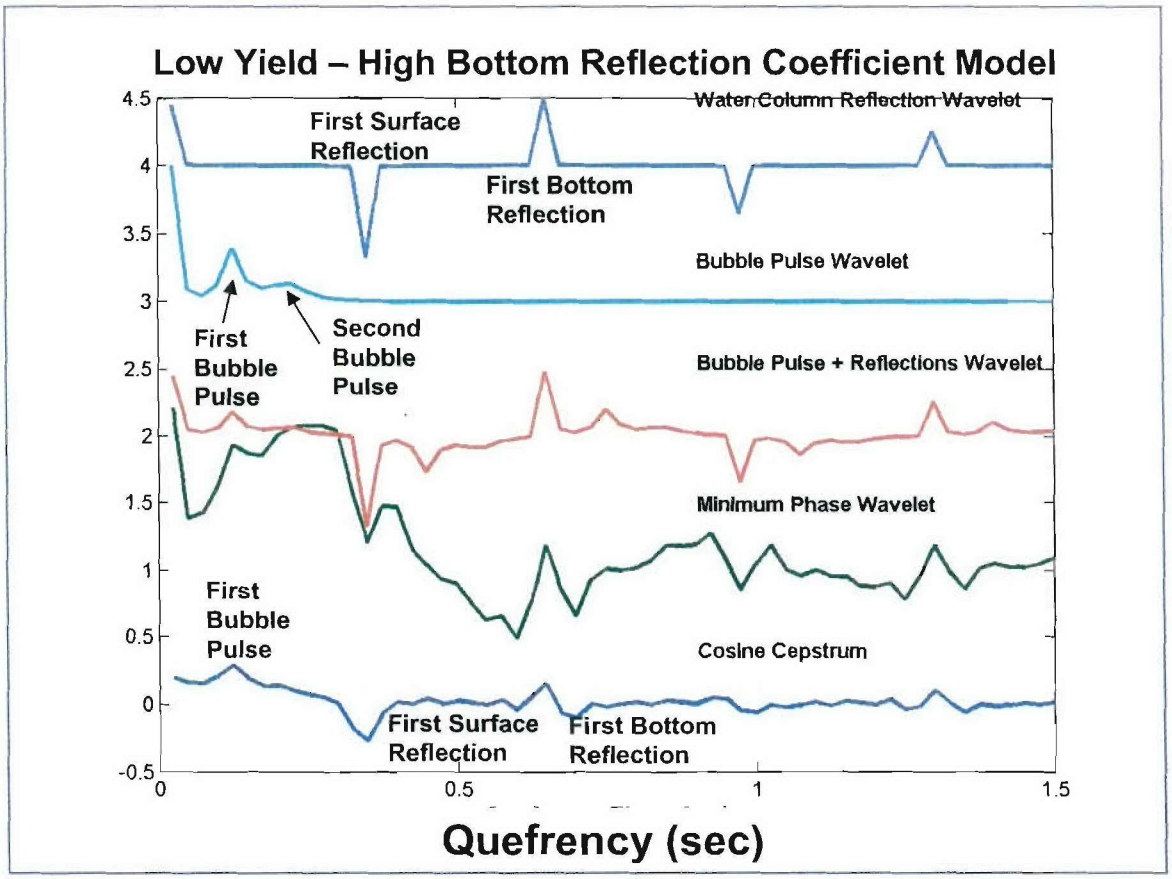

Figure 36. Model construction for a high-yield interpretation of the Murmansk explosion cepstra at ARCES. Surface reflection coefficient = -0.8, bottom reflection coefficient = 0.6, water depth = 240 m, depth of explosion = 235 m, yield=200 kg.

Figure 37 compares the synthetic cepstrum with the stack of all the individual phase cepstra at ARCES. With this model, we now explain the 0.2-second peak, as being the primary bubble peak and the peak at 0.7 seconds is now the first bottom reflection. However, to get a peak that large from a bottom reflection, we must assume a bottom reflection coefficient of 0.6. This depth is close to the known water depth in the region and the 200 kg yield estimate is more consistent with a low-magnitude event.

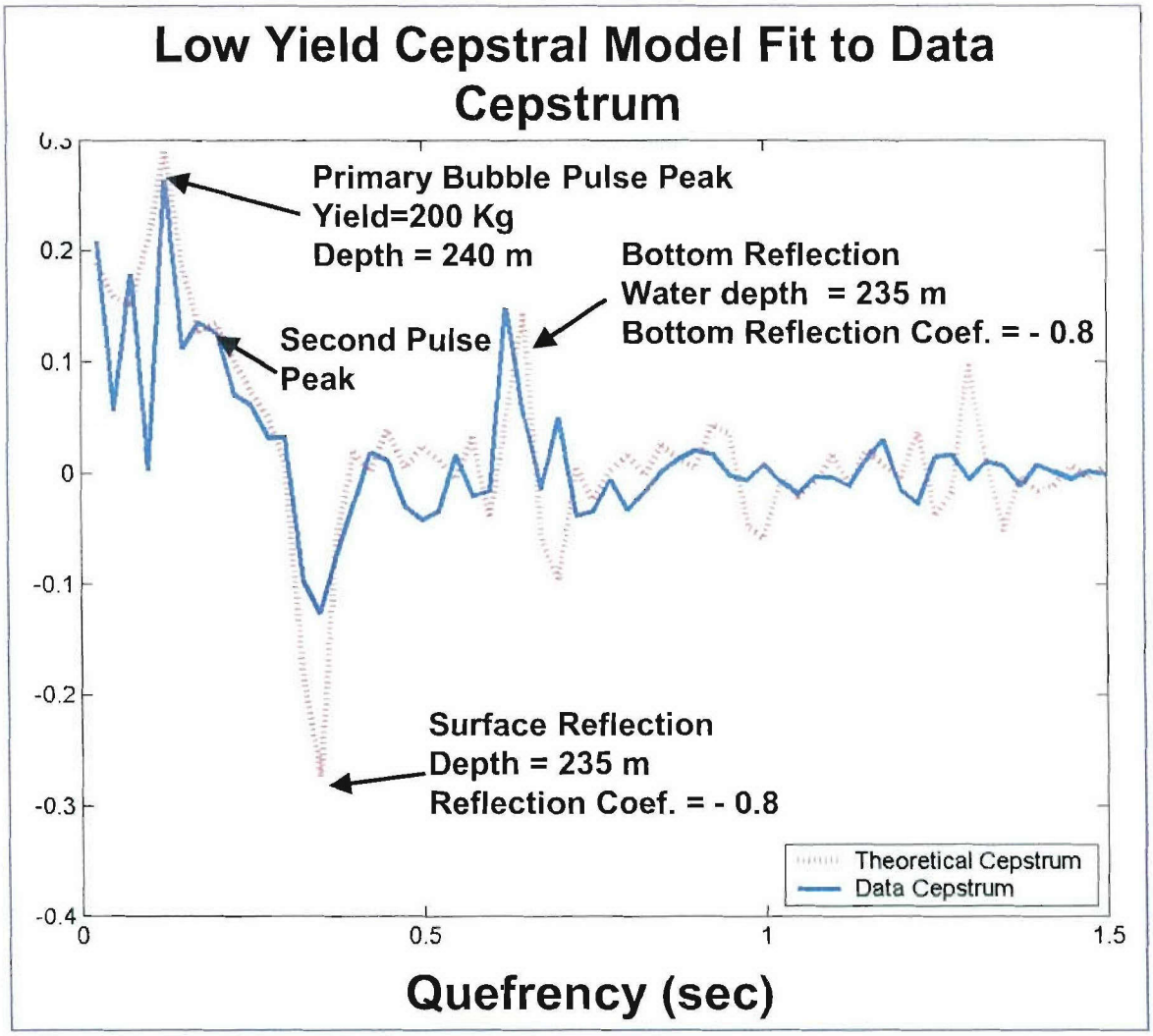

Figure 37. Comparison of low-yield synthetic cepstrum with the stack of all the phase cepstra at ARCES.

One of the problems we have had in matching these cepstra, as noted earlier, is that a small surface reflection coefficient has to be assumed to explain the negative peak. Normally, we would expect this coefficient to be about –0.9. However, Figure 37 shows that assuming a –0.8 surface reflection coefficient produces a negative trough that is much larger than the observed trough. This trough is produced by the negative correlation of the primary pressure pulse in the water and the surface reflection. The fact that this peak is so much smaller than expected from the model indicates that the two pulses are somewhat decorrelated. This lack of correlation may have been caused by distortion of the reflection

off the surface, or distortion of the signal as it propagates through the water column. Our model is currently not able to explain this decorrelation.

We conclude, based on this analysis, that the Murmansk event was in fact a small underwater explosion, detonated on the bottom of the Barents Sea near Murmansk, with a yield of about 200 kg.

4.2 AUGUST 12, 2000 KURSK EVENT ANALYSIS.

In this section, we interpret the seismic signals recorded from the Kursk submarine accident that occurred on August 12, 2000.

The Center for Monitoring Research (CMR) issued a report (Event Report, 2000) describing two events on that date, a small one (ML=2.2) and a later larger one (mb=3.6). The larger event occurred at 07:30:42 GMT and was described as having characteristics consistent with being an underwater explosion. In this study, we further analyze the event using the cepstral modeling and inversion algorithm, discussed earlier.

4.2.1 Waveform Analysis

Figure 38 shows on a map the location of the second large Barents Sea event, given in CMR report (Event Report, 2000), and the locations of nearby Scandinavian arrays that detected the event. Although the location is based on phases detected at ten stations, we focus on the waveforms from the arrays, and primarily, the closest array, ARCES (ARA0). Figure 39 shows a record section of recordings of the event at the regional arrays shown in Figure 38 and the identified regional seismic phases.

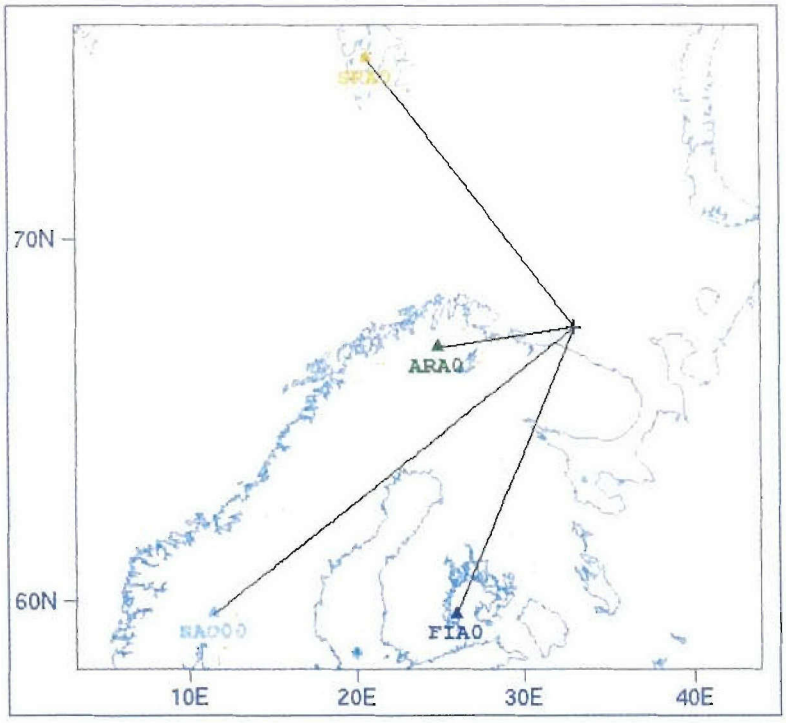

Figure 38. Map showing the location of the second and largest seismic event that occurred on August 12, 2000 at 07:30:42.

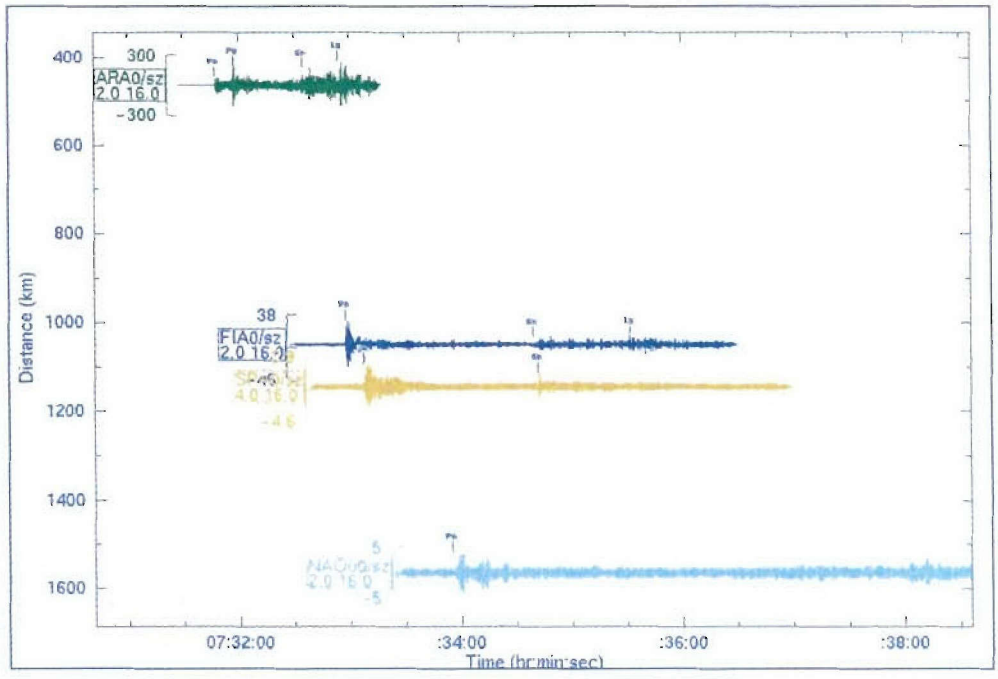

Figure 39. Record section of single-channel recordings from the Scandinavian arrays, which recorded the August 12, 2000 event in the Barents Sea. Each waveform was bandpass filtered in frequency bands, as indicated.

Regional phases *Pn* and *Sn* could be identified at all stations, with the possible exception of NORSAR (NAO00), although a weak phase can be discerned at about 7:38:00 that may be *Sn*. *Pg* and Lg are clearly observed at ARCES, and Lg is observed at FINES.

In the remainder of this section, we primarily focus on the ARCES array data. Figure 40 shows a bandpass filter analysis of the ARA0 channel waveform of ARCES.

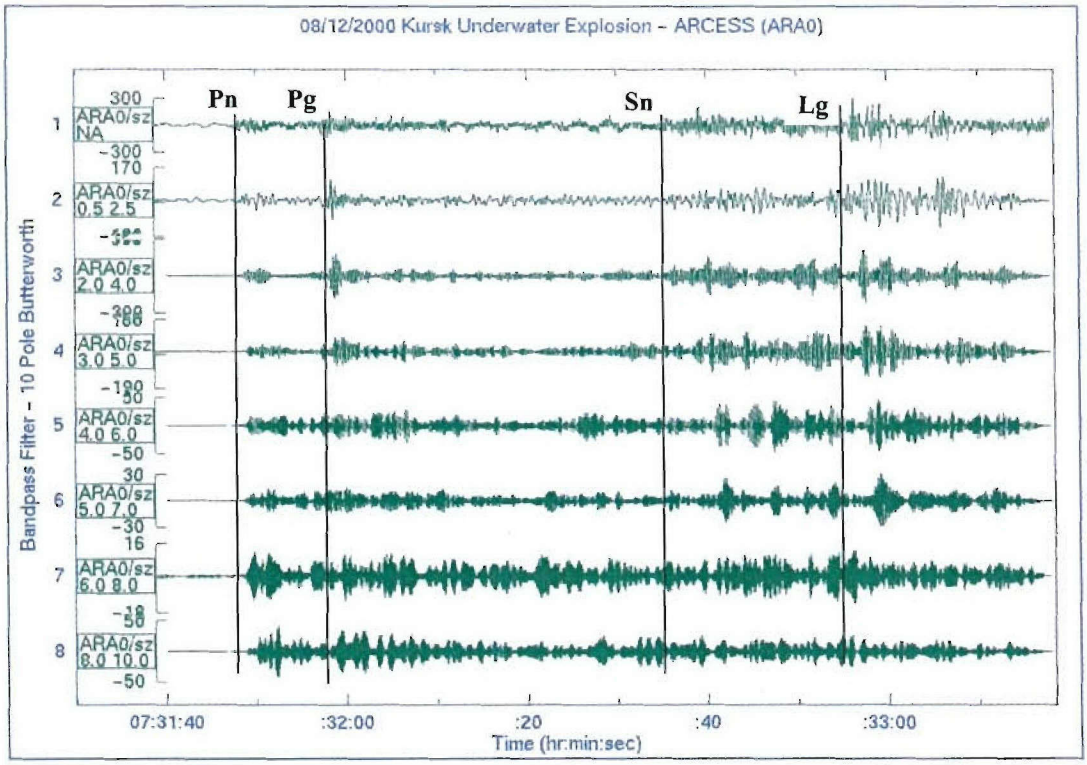

Figure 40. Bandpass filter analysis of the ARA0 channel waveform at ARCESS.

The phase picks made on the lower frequency bands are indicated with vertical lines that also shows their times at higher frequencies. Strong *Sn* and Lg phases are evident at low frequency. The *Pg* phase is very strong in the 2-to-4 and 3-to-5 Hz band. However, at the higher frequencies, the phases become much less distinct and look more like scattered waves. This result is somewhat different than the October 23, 1997 Murmansk explosion, described above, where we observed that the explosion had distinct phases at the higher frequency. Another difference is that the Murmansk explosion had much stronger shear waves relative to compressional waves at high frequency. Strong *Pn* and coda waves are apparent for the August 12, 2000 event in Figure 40, but the shear waves *Sn* and Lg are

not as evident in the coda at high frequency as they were for the Murmansk event.

4.2.2 Regional P/S Ratios

The ratios of the *Pn/Sn* and *Pg/Sn* ratios for the event measured at ARCES, along with measurements from earthquakes and explosions in nearby regions also recorded at ARCES, are plotted as a function of frequency in Figure 41. The earthquakes occurred in northwestern Norway and in the Norwegian Sea, the mine blasts on the Kola Peninsula, and the nuclear explosions at Novaya Zemlya. The marine explosion points (blue triangles) are for the presumed underwater explosion or implosion associated with the earlier Komsomolets submarine sinking in 1989. A line connects the points for the August 12, 2000 event. All ratios have been corrected for distance.

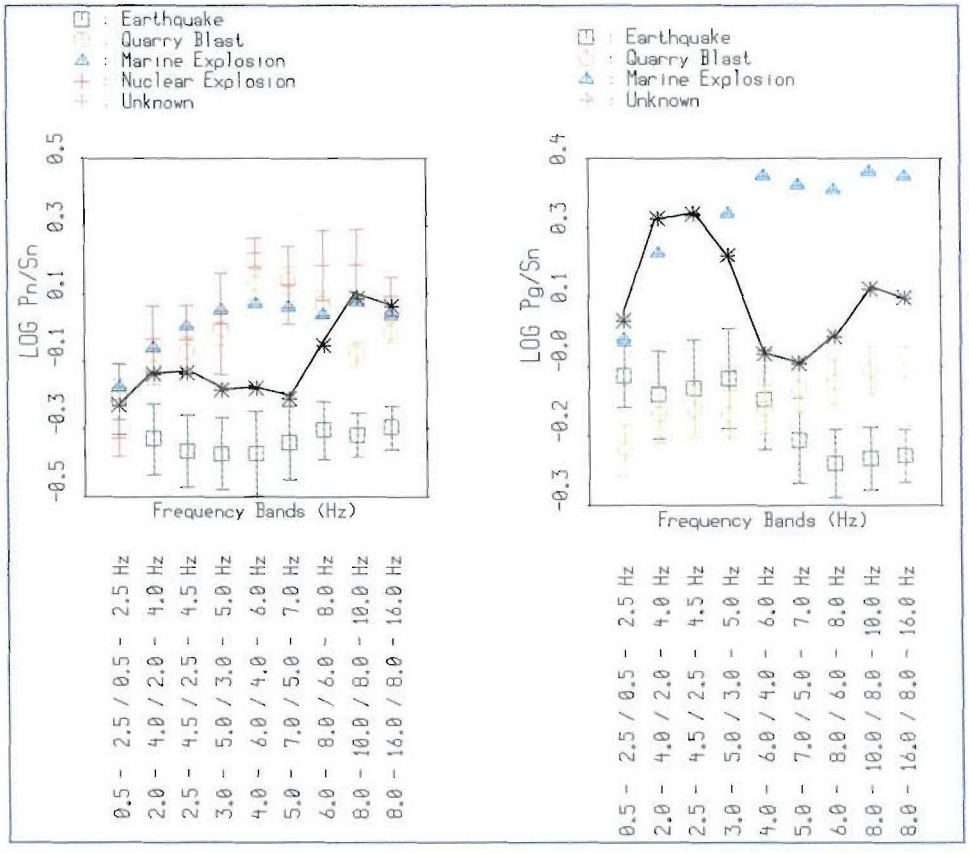

Figure 41. Pn/Sn (left) and Pg/Sn ratios plotted as a function of filter frequency band. The ratios have been corrected for distance.

The connected points for the August 12, 2000 event fall between the mine blast and earthquake points for the *Pn*/*Sn* ratios at lower frequencies but are more explosion-like at higher frequency. The *Pg*/*Sn* ratios are clearly explosion like across the entire frequency band. This trend can also be clearly seen in Fig, where the *Pg* and *Sn* phases are both quite strong at low frequency, and *Pg* is very impulsive and larger than Sn in the 0.5-2.5 and 2–4 Hz bands.

Overall, the *Pn*/Sn and *Pg*/Sn ratios are consistent with the event being an underwater explosion.

4.2.3 Spectral/Cepstral Analysis

Figure 42 shows the array-averaged spectra for each regional phase and noise.

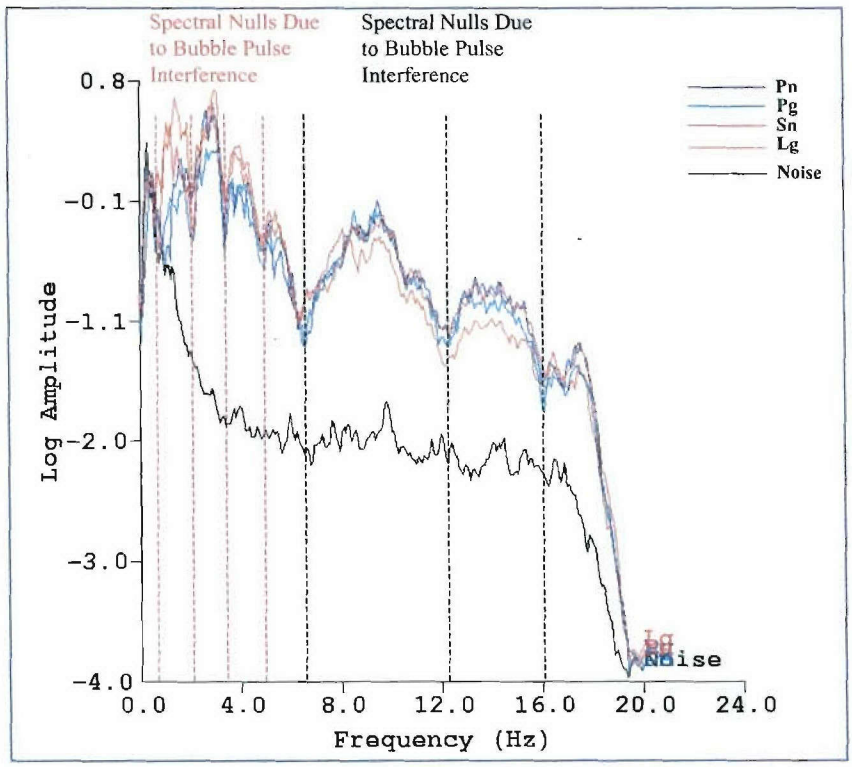

Figure 42. Array-averaged spectra for each regional phase from the 12 August 2000 event and the background noise to *Pn* recorded on the vertical component channels of ARCES.

These spectra are computed by first making spectral estimates of each of the four phases, *Pn*, *Pg*, Sn, and *Lg*, on each vertical component channel of the array and then averaging the spectra across all array elements. The noise spectra ahead of the *Pn* phase on each channel are computed in the same way. The spectra have not been corrected for instrument response. Thus, the spectra go to low values at low frequency, because of the low-frequency instrument response roll off, and at about 18 Hz on the high end due to the anti-aliasing filter. The most notable feature of the spectra is the strong modulations or "scalloping" of the spectra that appear in all phases. The black vertical dashed lines indicate the nulls of essentially two interfering scalloping patterns. The broader scalloping, indicated by the black vertical lines, have nulls separated by about 5 Hz. This broad scalloping results for spectral interference of reflections in the water column. The first peak of this broad scalloping has another scalloping pattern superimposed, as indicated by the red dashed lines, due to the bubble pulse.

Figure 43 shows the cosine or signed cepstra computed from the spectra in Figure 42.

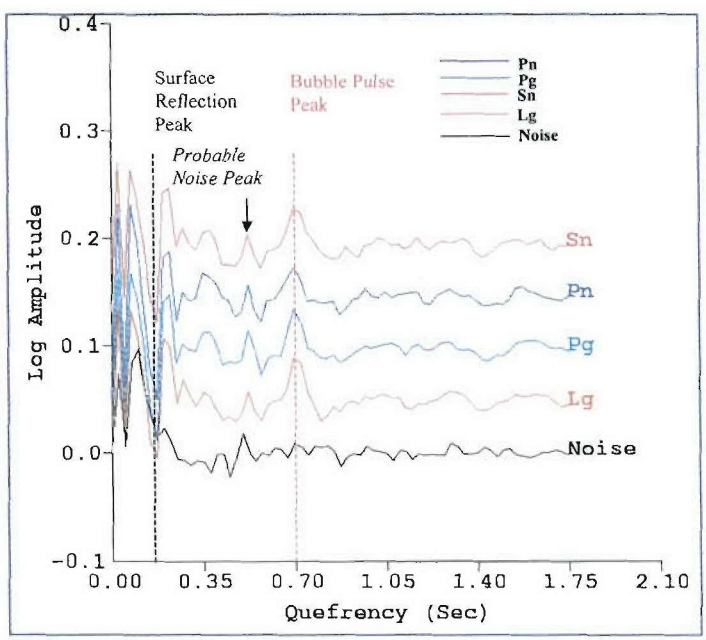

Figure 43. Cepstra computed from the spectra in Figure 42. The cepstra for the phases and noise have been shifted for display purposes.

The cosine cepstra are computed by methods discussed above. The red dashed line indicates the primary positive cepstral peak in the phase cepstra. Note that this peak does not appear in the noise. We interpret this peak as resulting from the bubble-pulse scalloping, as indicated in Figure 42, and has a delay time of about 0.75 seconds. The black dashed line indicates a negative peak at about 0.2 seconds that also does not appear the noise. We interpret this peak as resulting from the broad spectral scalloping in Figure 42 caused by the surface reflection, which would have a negative polarity relative to the primary phase. Thus, we conclude that these spectra and cepstra are consistent with the characteristics of underwater explosions.

4.2.4 Cepstral Model and Inversion

To further confirm that this event was an underwater explosion, and to estimate its depth and yield, we attempt to fit model cepstra for explosions to the observed cepstra.

For modeling purposes, we again choose to model the "stacked" cepstrum, that is, the average of each of the individual phase cepstra. The stacked cepstrum provides some improvement in signal strength and reduces features that do not appear in all the cepstra. Because the model cepstra are phase-independent, the stacked cepstrum serves as the best overall representation of the observed cepstra.

In Figure 44, both the spectra and cepstra are replotted with the stack spectrum and cepstrum plotted as the green trace. In this case, the spectra and cepstra of the individual phases are very similar so that the stacked spectra and cepstra are very similar to the individual ones. From now on, we use the stacked cepstrum as the observed cepstrum that we attempt to fit with a model cepstrum.

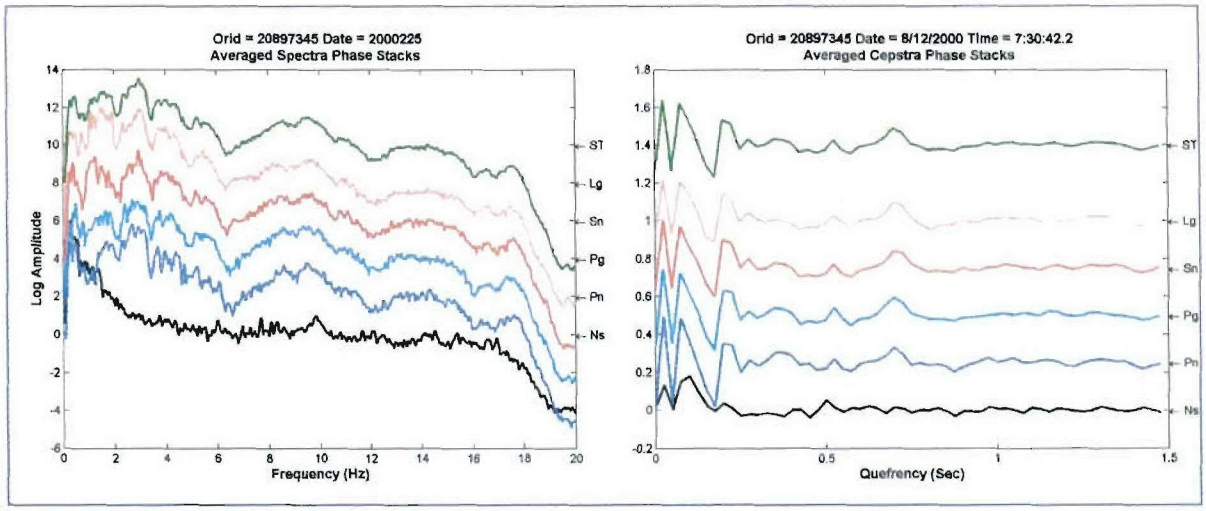

Figure 44. (Left) Noise, phase and stacked spectra; (right) Phase, noise and stacked cepstra. The green traces are the stacked spectra and cepstra.

Also, we are only interested in modeling features that appear in all of the individual phase cepstra, and not in the noise cepstra. Generally, we regard any feature that appears in both the signal and noise cepstra to be due to effects of noise or processing artifact. For example, in Figure 43, we point out a peak that appears in the cepstra just ahead of the bubble-pulse peak. This peak may also be in the noise cepstra, so we choose to ignore it when fitting model and signal cepstra. In order to try to reduce noise effects, we have experimented with two noise subtraction methods. In the first method, we subtract noise spectra from each of the individual phase spectra before the cepstrum computation. In the second method, we subtract the noise cepstrum from the signal cepstrum. In this study, we show the results of fitting modeled cepstra to observed cepstra corrected by spectral noise subtraction. The same results were obtained with cepstral noise subtraction.

We use the exhaustive grid-search method for matching synthetic and observed cepstra and use the one minus the L1 norm (1-L1) as the match statistic, where the L1 norm is the averaged absolute value of the difference between the observed and synthetic cepstra. plot. Figure 45 shows the result of this analysis on the spectral-noise corrected cepstra.

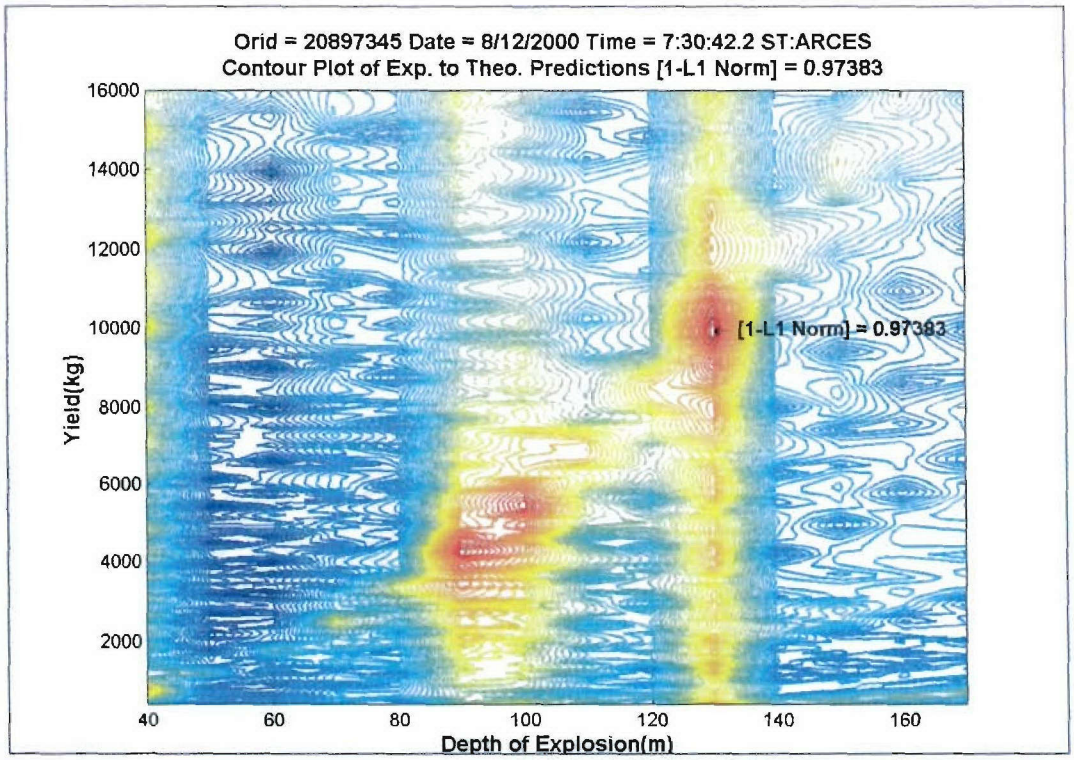

Figure 45. Contour plot of 1-L1 as a function of depth and yield for matches of synthetic cepstra to observed cepstra corrected by using noise spectra.

This plot shows that the solution is non-unique in that there are two peaks, one at low yield, about 4500 kg, and the second at a considerably higher yield of over 10000 kg. The higher-yield peak has a slightly higher 1-L1 statistic which is why it was picked in Figure 45. Also, the depth of the lower-yield peak is about 90 m compared with a depth of about 130 m for the higher-yield peak. Both of these depths are reasonably consistent with the known bathymetry in the region, where the water depths are on the order of 250 m.

Figure 46 shows cross sections at constant depth through these two peaks. The width of these peaks gives some measure of the yield-estimation uncertainty of this method.

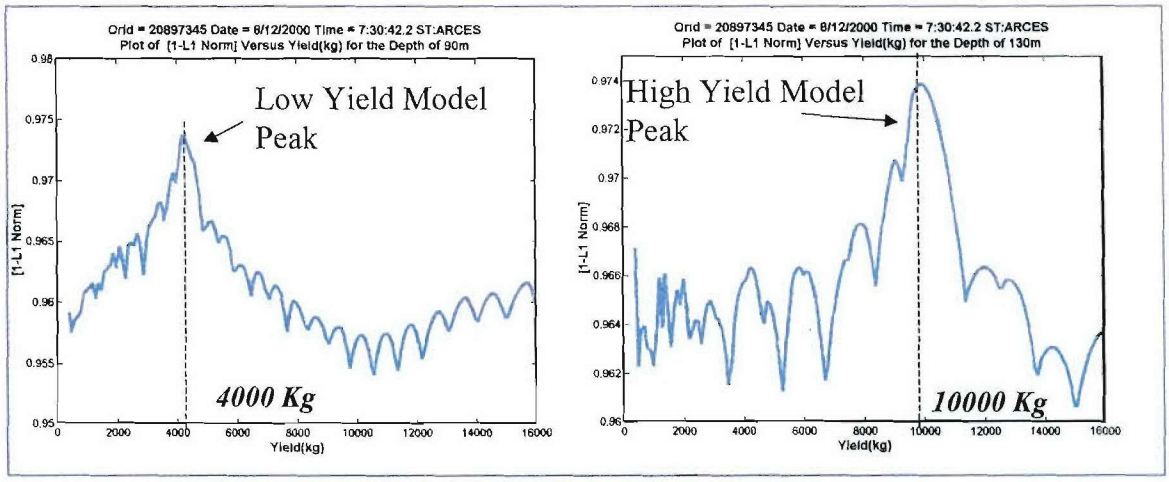

Figure 46. Constant-depth cross sections through the two peaks shown in Figure 45.

Both peaks are significant and their 1-L1 values are nearly the same, or about 0.97. Therefore, these plots alone are not sufficient alone to determine which model is best. Figure 47 shows a comparison of the synthetic and observed stacked cepstra for these two peaks.

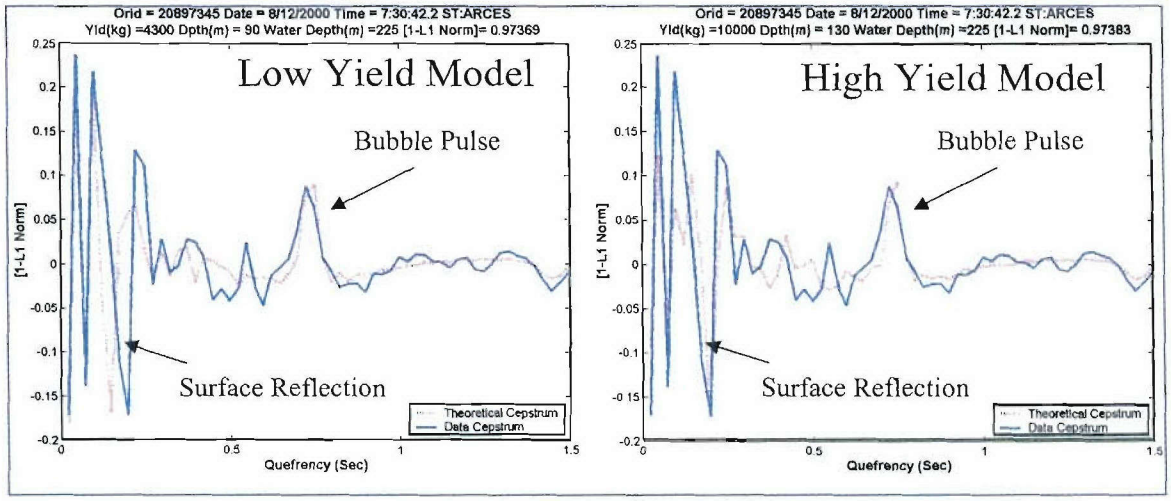

Figure 47. (Left) Comparison of synthetic and observed cepstra for the low-yield peak in Figure 45. (right) Comparison of synthetic and observed cepstra for the high-yield peak in Figure 45.

Both models match the bubble-pulse cepstral peak amplitude and delay time reasonably well. Looking at the spectra in Figure 42, there to be two broad modulations due to reverberations with peak separations of 4 Hz and 6 Hz. The former produces a cepstral trough

at 0.25 Hz and the latter produces one at 0.16 seconds. Both of the troughs appear in the cepstrums in Figure 43. The depth of 90 m appears to be matching the 0.16-second trough on the stack cepstrum, but not the 0.25 trough, whereas the 130 m depth is matching the 0.25 second trough by not the 0.16. The known water depths in the region are about 100 m. Thus, we would favor the 90 m depth with the lower yield.

One possible explanation for the two sets of modulations is that the 4 Hz modulation extends from about 12 Hz to 16 Hz, and the antialias filter rolloff begins at about 16 Hz. It could that the apparent 4 Hz modulation is due to the filter cutting off the high-frequency lobe of the modulation. Thus, this modulation frequency may be lower than it should be, producing the 0.25 Hz peak in the cepstrum.

Another possibility is that the surface modulation may be distorted by the proximity of the explosion to other reflection surfaces, such as the submarine itself, which could distort the spectral modulation. Other spectral peaks are evident in the spectra in Figure 42 at frequencies above 16 Hz, which may be causing some of this distortion. So, we believe that matching the 0.25-second cepstral peak may not be that important since it may be distorted. The 90 m depth model seems to match the very strong, low-quefrency peaks more accurately. Thus, we believe that this match is more likely the correct model.

4.3 CONCLUSIONS.

We conclude overall, based on our analysis, that both events in the Barents Sea that occurred on October 23, 1997 and August 12, 2000 were underwater blasts. For the Murmansk event, we used a trial and error matching method to obtain synthetic cepstrum that explains the essential characteristics of the observed cepstrum. The lower yield of the event, which was about 200 kg, with depth of 235 to 240 m is consistent with the small magnitude of the event and the known bathymetry in the region.

The second event on August 12, 2000 has signal characteristics consistent with the event being an underwater explosion, similar to those observed for the Murmansk event. Using the cepstral modeling and matching method, we obtain a best-matching model that has a

yield of 10000 kg, or about 10 tons, and a depth of 130 m. However, we also obtained a low yield fit of 4300 kg, or 4.73 tons, at a depth of 90 m. This lower-yield result seems to be more consistent with the expected yield of a torpedo as well as the known depth of water in the region, which is about 10 m.

News reports of sonar data indicated that the submarine may have been sunk by a very large explosion, perhaps due to an accidental torpedo explosion. It is possible that the explosion itself happened inside the submarine before it sank to the bottom, or the submarine may have rested somewhat vertically on the ocean bottom. Thus, the explosion may have occurred on or inside the submarine but elevated above the water bottom. Our results indicate that if the 90 m depth is right, the explosion occurred about 10 m above the surface.

Our estimates of yield essentially agree with the results of Koper et al (2001). However, Gitterman (2002), using some of the same data we have analyzed, recently published a lower yield of 1500 and 1650 kg for depths of 61 and 64 m. He states that the bubble frequency was 1.45 Hz, using ARCES data, which is close to our estimates. However, he uses the depths of 61 and 64 m to estimate the yields. After repeated readings of this paper, we cannot determine how he arrived at these depths. Apparently, they were not determined from data since he states that he was not able to observe any evidence of spectral modulations due to the water reverberations. However, we have shown clear evidence in this report of spectral modulations due to reverberations. Thus, we argue that Gitterman (2002) has underestimated the yields because his "assumed" detonation depths of 61 to 64 m are too low and are not supported by the data.

SECTION 5
OVERALL CONCLUSIONS AND RECOMMENDATIONS

This study has shown that seismic recordings of underwater blasts can be useful for the estimation of yield and water depths of the explosions. We have shown that the model developed by Baumgardt and Der (1998) effectively matches the predominant features of cepstra of underwater explosions, and simple fitting methods, using search techniques, can "invert" observed cepstra to infer the depth and yield of the explosion. The cepstral analysis technique provides a method for unambiguously separating out effects of bubble pulses and reverberation spectral modulations, and is a simpler technique that trying analyze harmonic peaks (e.g., Gitterman, 2002). Thus, the method can easily be automated for routine processing of seismic data.

The method described in this report was prototyped in Matlab© and is described more in a users manual that can be found in the Appendix. We recommend that this technique be incorporated as part of screening of events that are located off shore, including those that occur close to coasts where the error ellipses overlap land areas. If an event that occurs offshore can be fit with an underwater explosion cepstral model, then it could be so identified. Our analyses of many offshore events near Scandinavia in our first report (Baumgardt, 1999) showed that many offshore events are underwater blasts and the automated screening methods being used by the IDC and other national data centers should properly identify such events.

More research is required to refine the matching techniques and to estimate confidence of match. Studies of how this method works on earthquake spectra should also be made. In our Annual Report (Baumgardt, 1999), we showed some data that indicated that undersea earthquakes could produce spectral modulations due to water reverberations. Discrimination studies might identify these events, however our analysis of discriminants for underwater blasts suggest that many of them are very earthquake like. Thus, the cepstral matching method may be needed for discrimination. Thus, methods for how to evaluate matches to earthquakes, or lack of good matches, must be developed.

Of course, our studies have been limited to chemical blasts. Generally, the yields of these events are very low, compared to those for even small nuclear blasts. The task of monitoring for underwater blasts currently resides with the hydroacoustic networks, and the methods described in this report, with some modification, could also be applied to hydroacoustic data. However, we recommend that seismic monitoring systems also have the capability of characterizing underwater blasts, since explosions may occur in inlets or inland seas which may cause hydroacoustic signals to be blocked. Also, as we argued in the introduction, seismic signals propagate more directly from the source than do hydroacoustic signals. Because underwater blasts will likely produce sizable seismic signals, techniques such as this should be made available to the seismic monitoring systems as well as hydroacoustic systems.

REFERENCES

(U) Baumgardt, D.R. (1998). Anomalies in high-frequency P/S rations: The 16 October 1997 underwater explosion near Murmansk and PNEs recorded at Borovoye, Technical Notes submitted to Defense Threat Reduction Agency, 6 May 1998.

(U) Baumgardt, D.R. (1999). Characterization of underwater explosions by spectral/cepstral analysis, modeling, and inversion, Annual Report #1, submitted to Defense Threat Reduction Agency, November 1999.

(U) Baumgardt, D.R. and Z. Der (1998). Identification of presumed shallow underwater chemical explosions using land-based regional arrays, *Bull. Seism. Soc. Am.*, **88**, 581-595.

(U) Baumgardt, D.R. and A.M. Freeman (2000a). Seismic characterization of the November 8, 10 and 11, 1999 Dead Sea underwater chemical calibration explosions using cepstral modeling and inversion, abstract presented at 2000 Spring Meeting, American Geophysical Union, Washington, D.C. EOS, p. S7.

(U) Baumgardt, D.R. and A.M. Freeman (2000b). The August 12, 2000 Barents Sea Event: Preliminary Analysis, Technical Note Submitted to DTRA, ENSCO, Inc., Springfield, VA, August 31, 2000.

(U) Baumgardt, D.R. and K. Ziegler (1988). Spectral evidence of source multiplicity in explosions: application to regional discrimination of earthquakes and explosions, *Bull. Seism. Soc. Am.*, **78**, 1773-1795.

(U) Bondar, O. and V. Ryaboy (1997). Regional travel-time tables for the Baltic Shield region, Center for Monitoring Research, TR CMR-97/24, Arlington, VA.

(U) Cole, R.H. (1948). *Underwater Explosions*, Princeton University Press, Princeton, N.J.

(U) deGroot-Hedlin, C. and J. Orcutt (1997). Observations from T-phases from Pacific earthquake events: implications for seismic/acoustic coupling, *PL-TR-9702144*, Final Report, 12 November 1997.

(U) Der, Z.A. and D.R. Baumgardt (1998). Regional and teleseismic path attenuation estimates in Eurasia for the Indian and Pakistani nuclear explosions and seismic discrimination calibration for South Asia, *Proceedings, 20th Annual Seismic Research Symposium*, Sponsored to NPT/DOD and DOE, September 21-23, 182-191.

(U) Engdahl, E.R., R. van der Hilst, and R. Buland (1998). Global teleseismic earthquake relocation with improved travel times and procedures for depth determination, *Bull. Seism. Soc. Am.*, **88**, 722-743.

(U) Gitterman, Y. (2002). Implications of the Dead Sea experiment, Results for analysis of seismic recordings of the submarine Kursk explosions, *Seism. Res. Lett.*, **73**, 14-24.

(U) Event Report, Barents Sea, 2000/08/12. Event notification number 2000225-001, Preliminary REB-01, Issued 2000 August, Center for Monitoring Research, Arlington, VA.

(U) Gitterman, Y., V. Pinsky, and A. Shapira (1999). Dead Sea Calibration Explosions: Operation and Preliminary Data, Progress, Status and Management Report No. 26, Defense Threat Reduction Agency, 9 December 1999.

(U) Gitterman, Y. and A. Shapira (1994). Spectral characteristics of seismic events off the coast of the Levant, *Geophys. J. R. Ast. Soc.*, **116**, 485-497.

(U) Gitterman, Y. and A. Shapira (2000). Audio-visual and hydroacoustic observations of the Dead Sea calibration experiment.

(U) Gitterman, Y.Z., Z. Ben-Auraham, and A. Ginzburg (1998). Spectral analysis of underwater explosions in the Dead Sea, Geophys. J. Int., **134**, 460-472.

(U) Koper, K.D., T.C. Wallace, S. R. Taylor, and H. E. Hartze (2001). Forensic seismology and the sinking of the Kursk, *Eos, Trans. Am. Geophys. U.*, **82**, 4.

(U) Kennett, B.L.N (editor), (1991). IASPEI 1991 Seismological Tables, Research School of Earth Sciences, Australian National University.

(U) Laney, H., P. Dysart, and H. Freese (1998). Automated detection of underwater explosions by the IMS hydroacoustic network, abstract in *J. Acoust. Soc. Am.*, **105**, 1038.

(U) Nelder, J.A. and R. Mead (1965). Computer Journal, **7**, 308.

(U) Sereno, T.J. and J. A. Orcutt (1987). Synthetic *Pn* and *Sn* phases and the frequency dependence of Q in the lithosphere, *J. Geophys. Res.*, **92**, 3541-3566.

(U) Urick, R.J. (1983). *Principles of Underwater Sound*, McGraw-Hill, Inc., New York.

(U) Willis, H.F. (1941). Underwater explosions, time interval between successive explosions, British Report *WA-47-21*.

APPENDIX

CEPSTRAL ANALYSIS MODELING AND INVERSION TOOL

USER'S MANUAL

CEPSTRAL ANALYSIS MODELING AND INVERSION TOOL USER'S MANUAL

A1 GRAPHICAL USER INTERFACE (GUI)

The cepstral analysis modeling and inversion tool for underwater explosion allows the user to create and save cepstra files from selected data, and to run an inversion program on previously processed cepstra files. The inversion determines a best match, using various selectable comparison and optimization methods between the data cepstrum and various theoretical cepstra. For both of these options, input parameters must be specified.

A1.1 MODELING AND INVERSION PROGRAM.

The user interface for the Cepstral Modeling and Inversion Tool is Windows-based, and was designed using Matlab.

To start the program, double-click the Cepstral Analysis icon. The Cepstral **Modeling and Inversion Program** Window appears on the screen as shown in Figure A-1. The Cepstral Inversion Program may also be started by opening matlab, and typing cep_ana on the command line.

Note that the location of the cepstral inversion program needs to be added to the Matlab path for the program to run from any directory in Matlab. The Cepstrum folder, containing the cepstral inversion algorithm, should be placed in the /matlab/toolbox/Cepstrum directory. If the .../Cepstrum folder is not added to the matlab path, the user must be in the directory of the cepstral inversion program for the command cep_ana to run the inversion program.

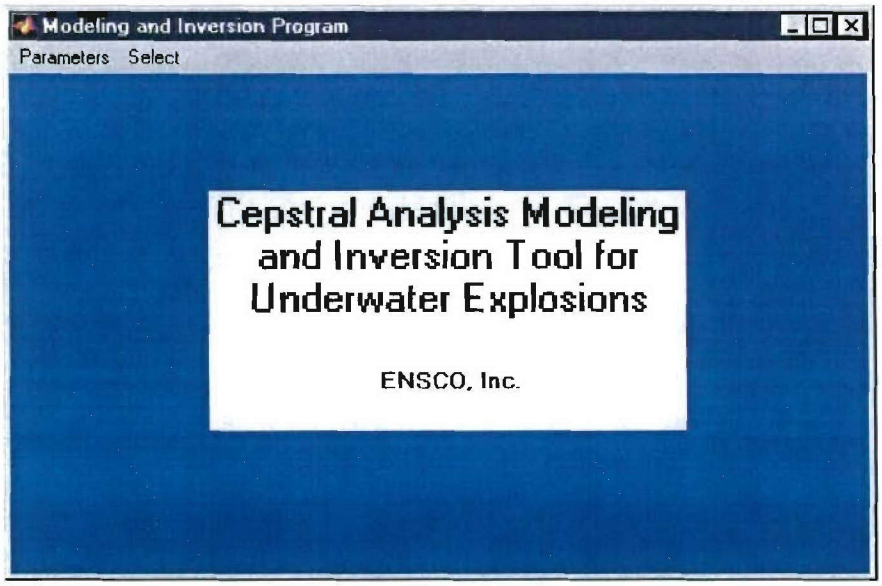

Figure A-1.Cepstral Analysis Modeling and Inversion Tool for Underwater Explosions Window

The Cepstral Analysis **Modeling and Inversion Program** window has two menus: **Parameters** and **Select**.

A1.1.1 Parameters Menu

The **Parameters** menu has one option: **Stations and Channels**. A detailed description of this option is given with Figure A-2. The **Stations and Channels** option is accessed by a pull-down option from the Parameters menu. Selections in the **Stations and Channels** window must be made in order to compute and save cepstra files from data.

Figure A-2. Parameters Menu and Options

Stations and Channels: Displays a window containing inputs for the waveform (*.w) file and inprefix of the additional files needed for processing the data. The files needed are:

*.w Waveform File

*.affiliation Network station affiliations

*.arrival Summary information on a seismic arrival

*.assoc Data associating arrivals with origins

*.origin ata on event location and confidence bounds

*.wfdisc aveform file header and descriptive information

*.wftag Waveform mapping file

Once these two inputs are chosen, the stations and channels for the particular waveform file chosen are displayed (section A1.2).

A1.1.2 Select Menu

The **Select** menu (Figure A-3) has two options: **Data Cepstrum** and **Inversion**. A detailed description of these two options is given in sections A1.3 and A1.4.

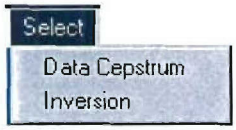

Figure A-3. Select Menu and Options

A1.2 STATIONS AND CHANNELS.

The **Stations and Channels** GUI window is shown in Figure A-5.

Waveform Files...: Clicking on this input button opens a browse window which filters for *.w files (Figure A-4). It is possible to browse, and also to select a different folder containing waveform (.w) files by changing the **Look in** folder in the browse window. Select the desired *.w file to process, either by selecting the file in the browse window, and selecting **Open**, or by double clicking on the desired *.w file in the browse window.

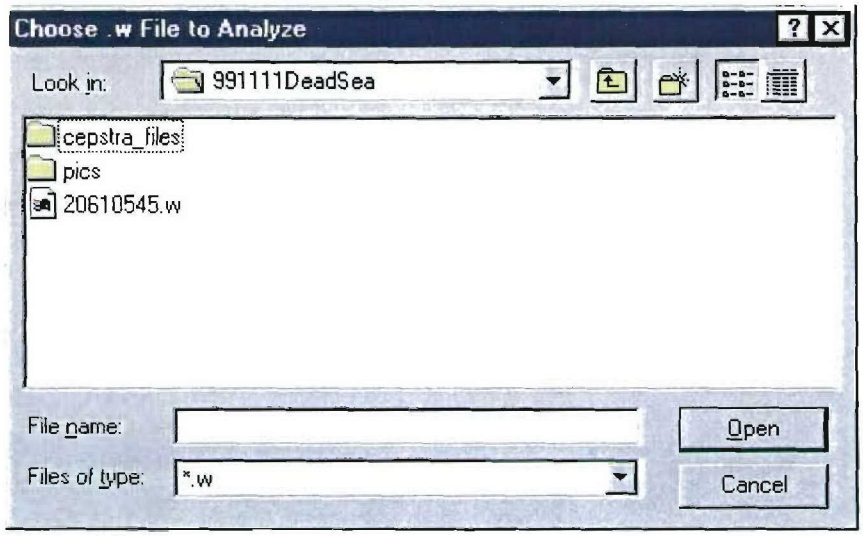

Figure A-4. Choose .w File to Analyze Browse Window

Prefix for Files: This is the prefix of the files needed, in addition to the *.w file for processing the data (section A1.1.1). Often, the prefixes for the *.w file and the other files are identical. Therefore, this edit box will fill in automatically with the prefix of the *.w file selected. However, when the prefixes for the additional files and the .w file differ, the **Prefix for Files** input box is edited to reflect the inprefix name of the additional files.

Stations:

Select All: Checks all of the checkboxes for stations listed in the window.

Clear All: Clears all of the checkboxes for the stations list in the window.

The station names for the chosen .w file(s) are listed (EIL, MLR, MRNI, Figure A-5) in a row. The elements of the respective stations are listed in up to two columns under the station name. The channels for each of the stations are listed under the station elements (be, bn, bz, Figure A-5). At least one element and one channel for one of the stations must be chosen in order to compute the data cepstrum.

Stations and Channels: Press this pushbutton after selecting waveform and inprefix for files. Stations and Channels will be displayed.

Save Selection: Saves the stations and channels to be processed. This also saves the selected *.w file and inprefix selected as defaults in the file, sta_cha.mat in the /matlab/toolbox/Cepstrum/MATFILES directory. Subsequently, they will be used as defaults.

Close: Closes the **Stations and Channels** window.

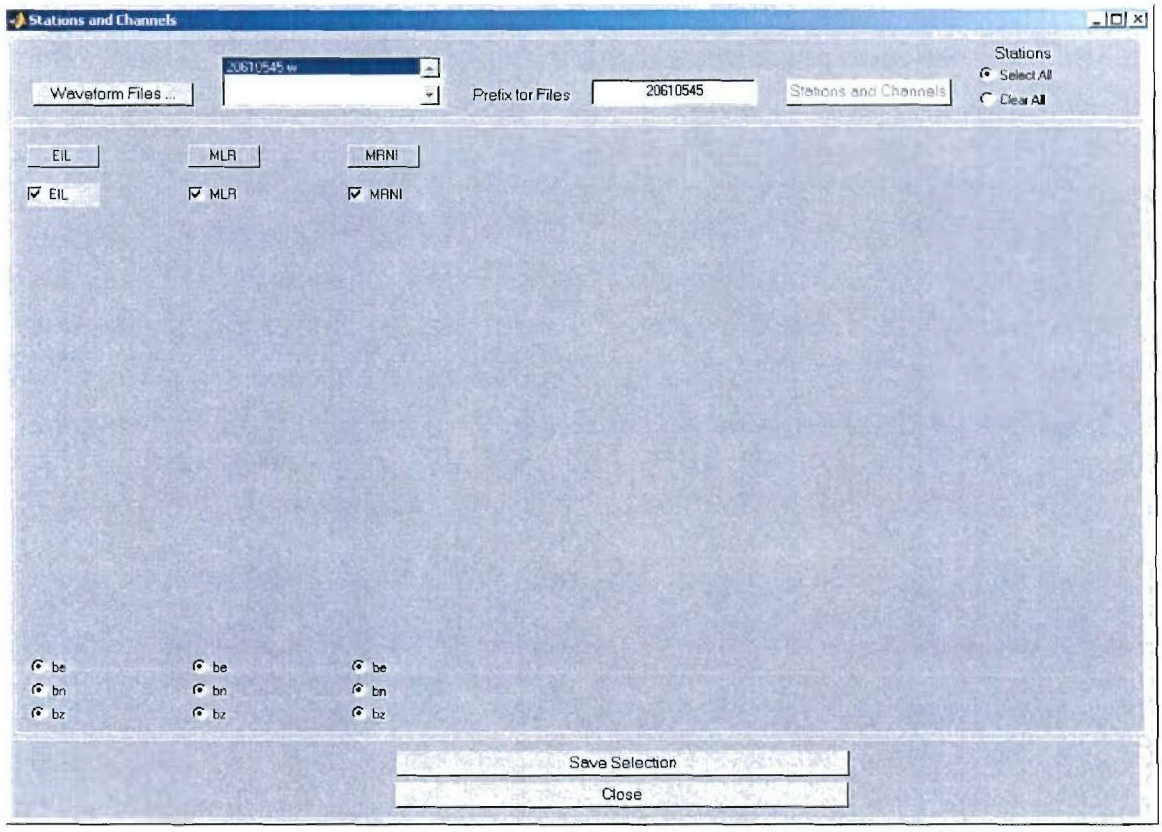

Figure A-5. Stations and Channels Window

A1.3 PROCESS CEPSTRUM.

The GUI window for **Process Cepstrum** is shown in Figure A-5. The **Process Cepstrum** window is accessed by selecting **Data Cepstrum** from the pull-down **Select** menu in the **Modeling and Inversion** window (section A1.1.2).

Utilities: The pull down menu contains the option to **Save Defaults**. Selecting **Save Defaults** saves the current inputs in the **Process Cepstrum** window for future use as defaults in a default_data.mat file in the /matlab/toolbox/Cepstrum/MATFILES directory.

File Processing: The corresponding box displays the *.w file currently processing. Clicking on the **File Processing...** pushbutton opens a browse window. Existing *.w files may be browsed; however, if a different *.w file is to be processed from the one displayed, the change of .w file must be made in the **Stations and Channels** window (section A1.2). This window will also display the corresponding stations and channels of the .w file for the user to select.

Inprefix: The inprefix for the additional files, besides the *.w file used to process data is displayed. The edit box contains the prefix for files specified in the **Inprefix** edit box in the **Stations and Channels** GUI.

Window: Specifies type of spectral smoothing. The windowing options to apply to the data are Hanning, Kaiser, or Parzen.

Length (s): The edit box specifies the length of the spectral window, in seconds.

Freq From: The edit box specifies the low frequency, in hertz (Hz), to filter the signal. This is the lower end of the bandwidth to compute the cepstrum

To: The edit box specifies the high frequency to filter to, in Hz. This is the higher end of the bandwidth to compute the cepstrum.

Subtract Noise: If checked, noise is subtracted from each phase. Noise is defined as the time before the first phase available for the station and channel. The noise is processed in the same way as the phase data.

Remove Instr. Resp.: If checked, the instrument response is removed by dividing out the response. The instrument response is read in from a file.

Plot Raw Spectra: If checked, the spectra of each phase and channel, without

polynomial subtraction or application of frequency limits specified in the **Freq From:** and **To:** edit boxes, are displayed, in a separate figure for each station.

Plot Spectra: If checked, the processed spectra for each phase and channel are displayed in a separate figure for each station.

Polynomial Fit Degree: Removes the trend from the spectra. The contents of the edit box specify which degree polynomial to fit to the spectra. This trend is then subtracted from the data.

Cepstrum:

Stacked Spectrum: Compute the data cepstrum by stacking the processed spectra, then taking the cepstrum of the stacked spectra. The cepstra files computed are saved in the folder specified in the **Save Files** input box, with the extension .cp.

Stacked Cepstrum: Compute the data cepstrum by computing the cepstra of the individual spectra, then stacking the cepstra. The cepstra files computed are saved in the folder specified in the **Save Files** input box, with the extension .sp.

Cepstrum Len. (s): Length of time to compute data cepstrum (in seconds).

Save Files: Location to save cepstra files, and also variable file containing inputs to creating the data cepstrum needed for inversion of data cepstrum and model cepstrum. The default for this file location is the .../cepstra_files folder in the folder which contains the data for processing. The file containing the parameters is saved as an 'inprefix'.mat file in the same folder.

Process Cepstrum: When selected, the variables specified in the **Process Cepstrum** window are used to compute the data cepstrum. The calculated cepstra are saved, both as averaged individual phases, and as a stack. The individual phases are saved as inprefix.phase_name.cp (or inprefix.phase_name.sp is **Stacked Spectrum** was selected in **Process Cepstrum** GUI). The stack is saved as inprefix.ST.cp (or inprefix.ST.sp if **Stacked Spectrum** was selected in the **Process Cepstrum** GUI). These files are saved

in the folder specified in the **Save Files** input box. Also saved is the file containing the input parameters needed for the inversion, as 'inprefix'.mat.

Close: When selected, the **Process Cepstrum** window is closed.

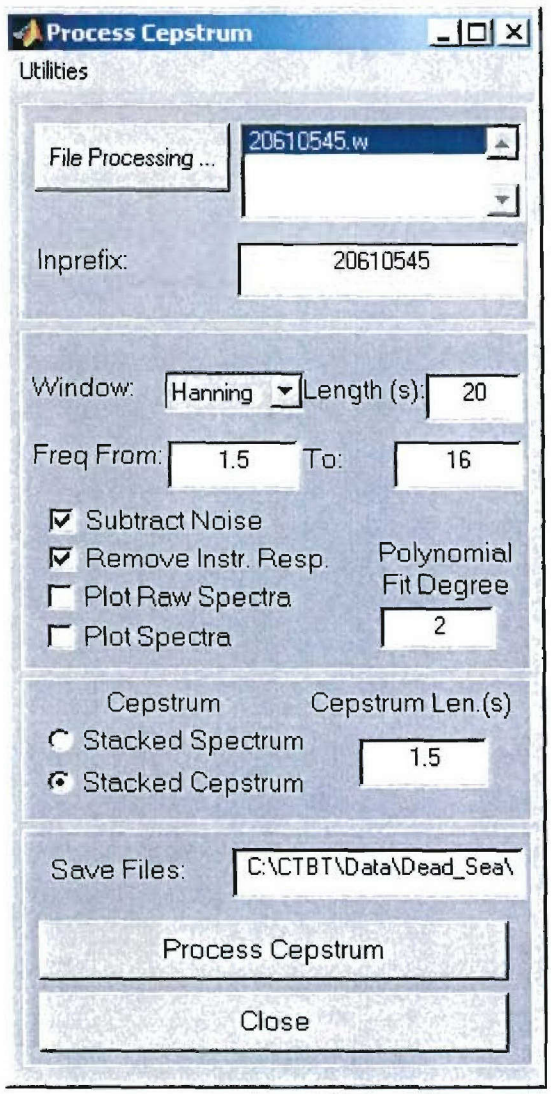

Figure A-6. Process Cepstrum Window

A1.4 INVERSION.

The GUI window for **Inversion** is shown in Figure A-7. The **Inversion** window shows a saved file from a previously saved processed cepstrum. Note that the name (and data) is

different than that previously shown for explaining processing the cepstrum (section A1.3). The **Inversion** window is accessed by selecting **Inversion** from the pull down menu in the **Modeling and Inversion** window (section A1.1.2).

Utilities: The pull down menu contains the option to **Save Defaults**. This saves the current inputs in the **Inversion** window for future use as an inv.mat file in the /matlab/toolbox/Cepstrum/MATFILES directory.

Saved Files...: When selected, displays a browse window on screen similar to that shown in Figure A-4. Clicking on this input button opens a browse window which filters for *ST.cp files, similar to Figure A-4. It is possible to browse and select a different folder containing cepstra (*ST.cp) files by changing the **Look in** folder in the browse window. It is also possible to select cepstra files, which were calculated using the **Stacked Spectrum** option from **Process Cepstrum** GUI window. These files have a *.sp suffix. Select the desired *.cp (or *.sp) file to process, either by selecting the file in the browse window, and selecting **Open**, or by double clicking on the desired *.cp (or *.sp) file in the browse window.

Inprefix: Specifies the inprefix to the saved parameters file (variables such as sampling rate) saved to the folder specified in the **Save Files** edit box when the cepstra were processed using the **Process Cepstrum** GUI. The edit box defaults to the inprefix of the saved cepstrum file to process.

Comparison:

Cross Corr: If selected, the cross correlation between the data cepstra and theoretical cepstrum is computed.

.....l1norm: If selected, l1norm between the data cepstrum and theoretical cepstra is computed

.....l2norm: If selected, l2norm between the data cepstrum and theoretical cepstra is computed

Optimization:

Range of Values: Exhaustive Search Technique that steps through user defined yield and depth space. At each grid point of yield and depth, the theoretical cepstrum is computed, and compared to the data cepstrum using the **Comparison** method chosen.

Downhill Simplex: Optimal Search Technique (originally developed by Nelder and Mead (1965)) that does a multidimensional search of a parameter space to minimize a function. In this case, to minimizes the difference between the data cepstrum and theoretical cepstra using the **Comparison** method chosen. This method finds a local minimum

Sim. Annealing: Optimal Search Technique that finds a global minimum between the data cepstrum and theoretical cepstra, using the comparison choice selected under **Comparison**.

Temps: The edit box contains the number of temperatures to be used for the Simulated Annealing search technique. This box is editable only if Sim. Annealing is chosen as Optimization technique.

Trials: The edit box contains the number of trials to be used for the Simulated Annealing search technique. This box is editable only if **Sim. Annealing** is chosen as **Optimization** technique.

Yield(kg): Yield in Kilograms(kg) for theoretical model. For **Range of Values Optimization** method, this is the beginning range of yield. For **Downhill Simplex and Sim. Annealing Optimization** methods, **Yield(kg)** is the starting point for the optimization method.

To: For **Range of Values Optimization** method, this is the high end of the yield range, in kg, for the theoretical cepstrum. This option is not visible if **Range of Values** is not the chosen **Optimization** method.

Step: The edit box signifies the successive steps from **Yield(kg)** and the value in edit box **To:** (high yield value) to take. This option is only available for the **Range of Values Optimization** method.

Depth(m): Depth in meters(m) for theoretical model. For **Range of Values Optimization** method, this is the beginning range of depth. For **Downhill Simplex and Sim. Annealing Optimization** methods, **Depth(m)** is the starting point, for the optimization method.

To: For **Range of Values Optimization** method, this is the high end of the depth range, in m, for the theoretical cepstrum. This option is not visible if **Range of Values** is not the chosen **Optimization** method.

Step: The edit box signifies the successive steps from **Depth(kg)** and the value in edit box **To:** (high depth value) to take. This option is only available for the **Range of Values Optimization** method.

Water Depth(m): The depth of the water, in m, at the location of the presumed explosion.

Sound Speed (m/s): Speed of sound in water, in units of (m/s).

Depth & Yield from Data Cepstrum: If this is checked, then an estimate of the beginning depth and yield values for the theoretical cepstrum are calculated from user input on the graph of the data cepstrum. When **Process Inversion** is pressed, a figure containing the stacks of the individual phases of the data cepstrum, as well as a stacked cepstrum over all phases is shown. With the mouse, hold cursor over the surface reflection and click once. Next, hold cursor over the first bubble pulse and click once. The algorithm computes a starting depth and yield from these inputs.

Plot Theoretical Model: If this is checked, then the theoretical model of the bubble pulse wavelet, water column reflection wavelet, bubble pulse and reflection wavelet, minimum phase wavelet, and cosine cepstrum will be displayed, for the theoretical model which is the best match to the data cepstrum by the chosen **Comparison** model.

Comparison to Theoretical(s): The edit box specifies the time, in seconds to compare the data cepstrum to the theoretical cepstrum.

Select Theoretical Parameters: If this is selected, a **Theoretical Parameters** window is shown (see section 0). This window allows the user to change theoretical cepstrum parameters.

Process Inversion: When selected, the algorithm utilizes the input parameters specified in the **Inversion** window to process the inversion of the data cepstrum with theoretical cepstra.

Close: When selected, the **Inversion** window is closed.

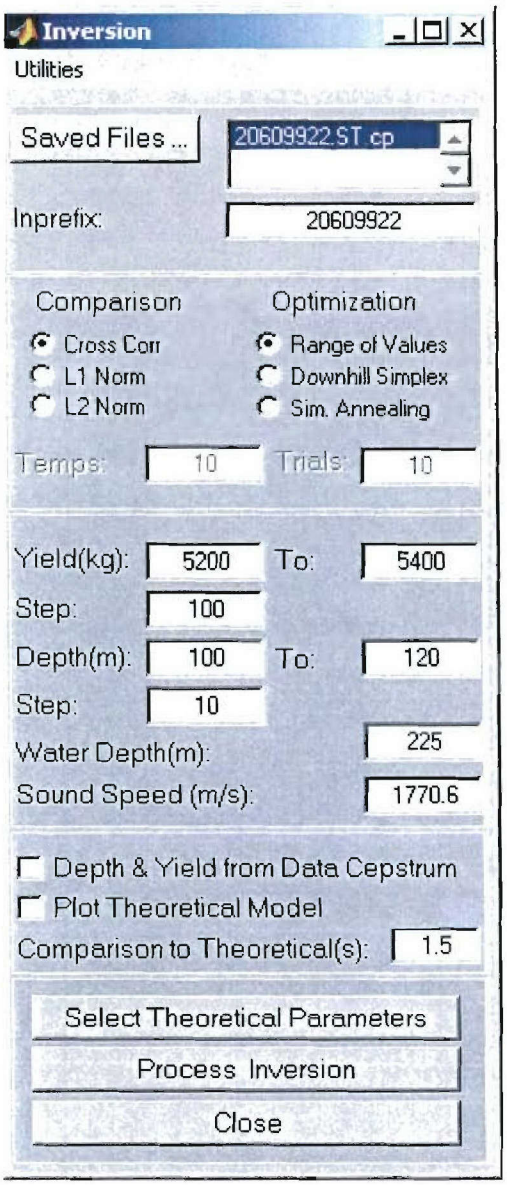

Figure A-7. Inversion Window

A1.5 Theoretical Cepstrum Parameters.

The GUI window for **Theoretical Cepstrum Parameters** is shown in Figure A-8. The **Theoretical Cepstrum Parameters** window is accessed by pressing **Select Theoretical Parameters** in the **Inversion** window. Default inputs are initially displayed, and used as parameters.

Surface Reflection: Reflection from the surface of the water (may range in value from – 1.0 to 0.0).

Bottom Reflection: Reflection from the bottom of the sea floor (may range in value from 0.0 to 1.0)

Decay Constant for Bubble Pulse: Multiplicative amplitude factor, which was set to 0.4, since this value was required to produce the spectral modulation observed (Baumgardt and Der, 1998, pg. 589).

Takeoff Angle (Degrees):

Number of Bubble Pulses: The number of bubble pulses, which can continue until the bubble rises and breaks the surface.

Bubble Pulse Weighting: Exponential time constants for each bubble pulse (?). Five edit boxes are provided, one for each of up to five potential bubble pulses.

Save Parameters: If selected then the inputs in the **Theoretical Cepstrum Parameters** GUI are saved to use in the inversion. Saving these parameters is optional. If not selected, then the default parameters will be used. Once the parameters are saved, they will become the new defaults, being saved as theo.mat in the /matlab/toolbox/Cepstrum/MATFILES directory.

Close: If selected, closes **Theoretical Cepstrum Parameters** window.

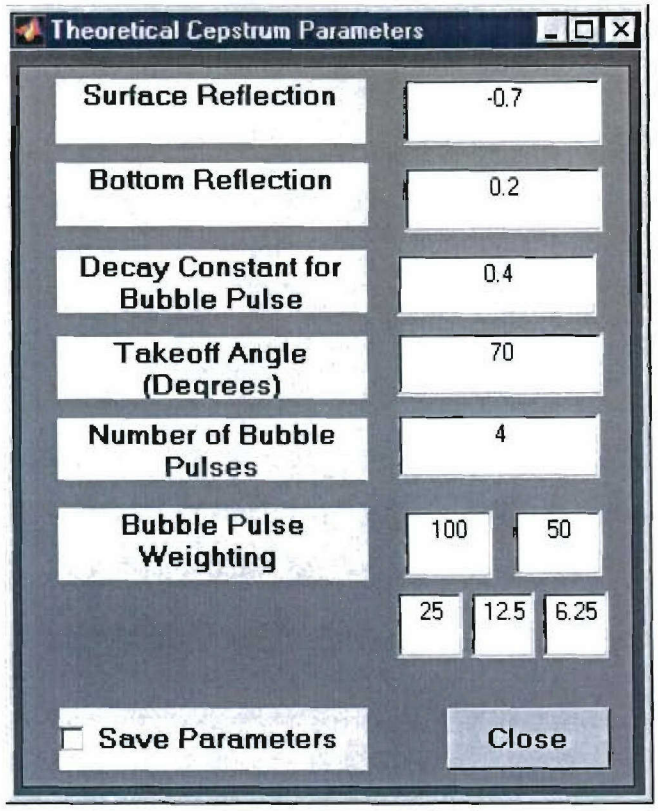

Figure A-8. Theoretical Cepstrum Parameters Window

A2 EXAMPLE

The following is a complete example that includes processing stacked cepstra from selected data. The files saved from processing the data cepstrum are then used for the inversion. The stacked data cepstrum is compared to model cepstra to find the best match. This best match provides the user with the depth and yield of the presumed underwater explosion. Please note that the terms in bold are described in Section A1.

A2.1 Location of Files.

The files used for this example are located in the locations detailed below. To compute the data cepstrum, the following files are needed:

*.w Waveform File

*.affiliation Network station affiliations

*.arrival Summary information on a seismic arrival

*.assoc Data associating arrivals with origins

*.origin Data on event location and confidence bounds

*.wfdisc Waveform file header and descriptive information

*.wftag Waveform mapping file

Note: In this example, the .w file, and also the additional files needed to process the data cepstrum have the prefix 20610545. The .w file and the additional files do not need to have the same prefix, although the additional files all need to be named with a common prefix.

The *.w file used, as well as the additional files needed to compute the cepstrum are located in (this folder is arbitrary):

C:/CTBT/Data/Dead_Sea/991111DeadSea/

This C:/CTBT/Data/Dead_Sea/991111DeadSea/ folder contains a subfolder called /cepstra_files/ It is imperative that the folder which contains your data contains a subfolder named /cepstra_files/ in order to save computed cepstra.

C:/CTBT/Data/Dead_Sea/991111DeadSea/cepstra_files/

This folder is where the calculated cepstra files will be saved.

The location of the Cepstral Modeling and Inversion program is in the matlab directory:

C:/matlabR12/toolbox/Cepstrum/

This /Cepstrum folder also contains a /MATFILES folder, where the default inputs to the GUI may be saved. The /Cepstrum folder has also been added to the matlab path.

C:/matlabR12/toolbox/Cepstrum/MATFILES/

A2.2 DATA CEPSTRUM.

The data cepstrum is computed from inputs from the **Stations and Channels** GUI window, and also the **Process Cepstrum** GUI window

A2.2.1 Stations and Channels -- Selecting Waveform, Stations and Channels for Computing Data Cepstrum

On the matlab command line, the command cep_ana is typed. This opens the **Modeling and Inversion** GUI shown in Figure .A-1. Please note that the folder containing the cepstral inversion algorithm has been added to the matlab path. Therefore, it can be run from any matlab directory. First, it is desired to compute a cepstrum from data. Therefore, the **Parameters** pull down menu is chosen, and the **Stations and Channels** option is selected, as shown in Figure A-9.

The **Stations and Channels** GUI window opens, with blank inputs, as shown in Figure A-10. Click on **Waveform Files...** pushbutton. This opens the **Browse Window**, Choose .w File to Analyze (Figure A-11). The **Look In** directory is changed to C:/CTBT/Data/Dead_Sea/991111DeadSea/. The browse window filters on .w files. The desired 20610545.w file is selected with the mouse. **Open** may now be pressed to open the file, or the file may be double clicked to open.

The **Stations and Channels** GUI window gets filled in with the waveform file name. Also the **Prefix for Files** edit box is filled in with the prefix of the selected .w file. This is the prefix for the additional files, besides the .w file needed to process the data. If the prefix for these additional files differs from the prefix for the .w file, this **Prefix for Files** edit box must be changed to reflect the prefix for the additional files. The **Select All** button is selected. Therefore all of stations corresponding to the input waveform are also selected. **Clear All** clears the selection of the stations.

The program displays the stations and channels associated with the chosen .w file. Vari-

Various combinations of stations and channels may be selected for processing the data cepstrum. However, at least one station and a corresponding channel must be selected. Once the desired inputs are chosen, push **Save Selection**. This saves the inputs for use in processing the data cepstrum, and also saves the input .w file and location, to be used as a subsequent default as the file file_loc.mat inC:/matlabR12/toolbox/Cepstrum/MATFILES.

For this example, the bz channels of stations EIL and MRNI were selected for processing, as shown Figure A-12.

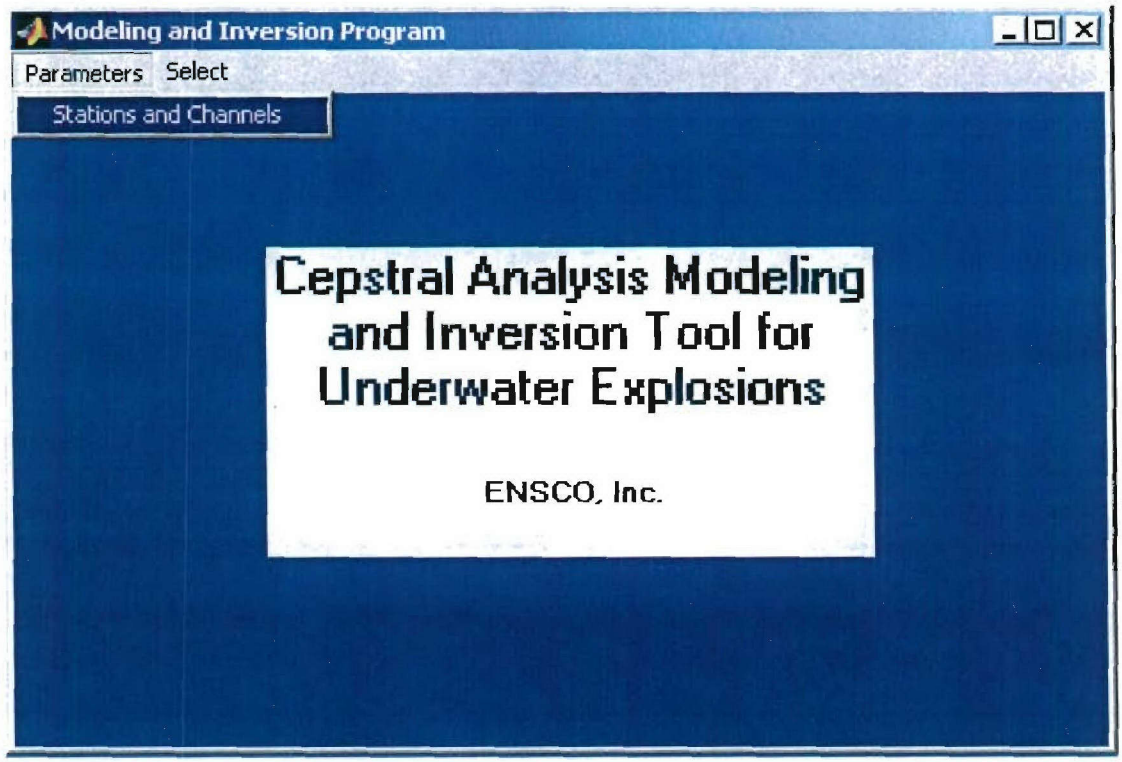

Figure A-9. Modeling and Inversion

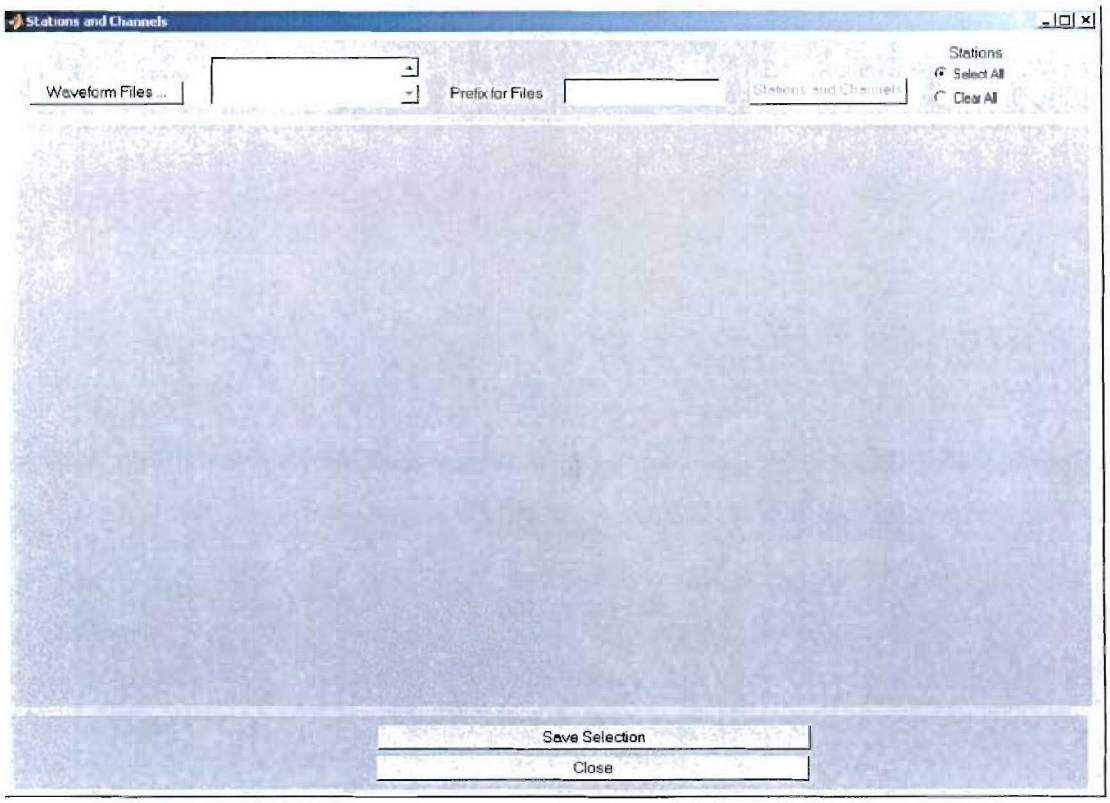

Figure A-10. Initial Stations and Channels Display

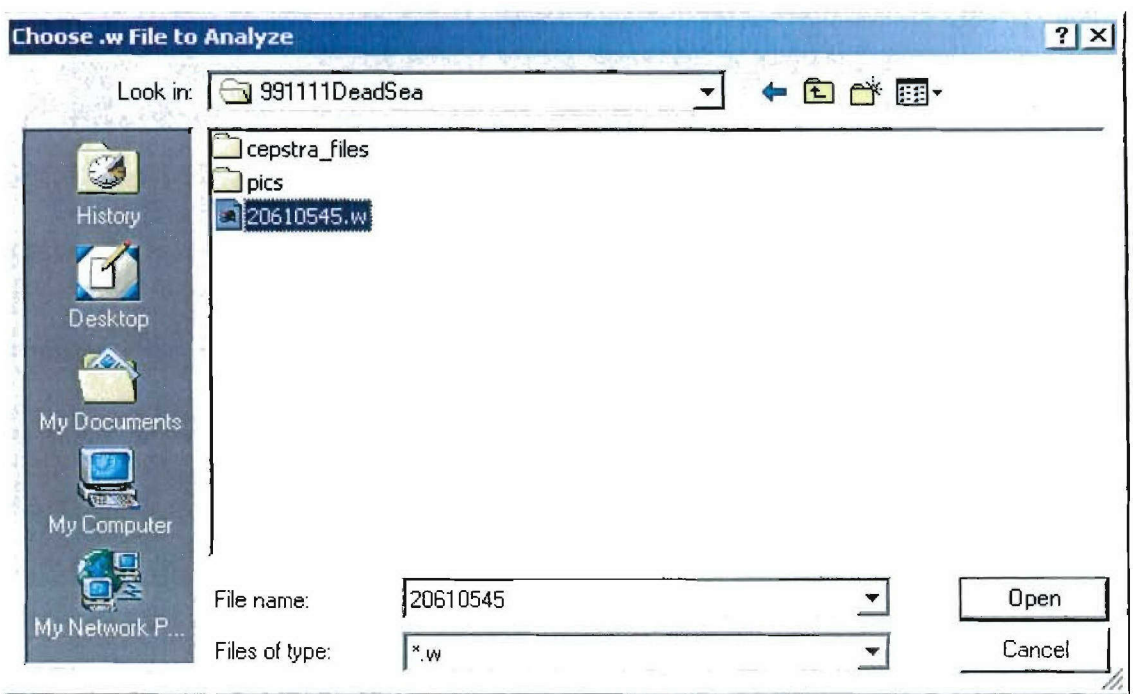

Figure A-11. Waveform Files……Browse Window

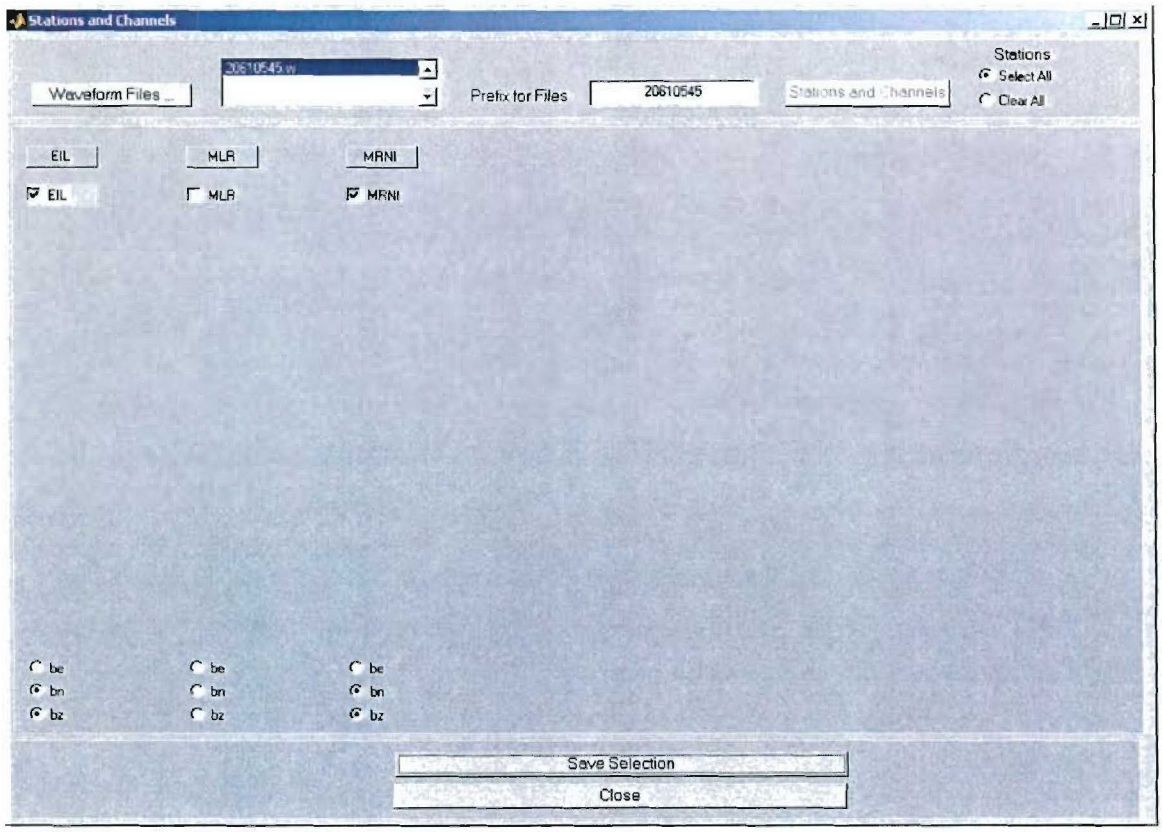

Figure A-12. Selected Stations and Channels

A2.3 PROCESS CEPSTRUM – VARIABLE INPUTS FOR COMPUTING DATA CEPSTRUM.

In the **Modeling and Inversion** GUI window (Figure A-1), from the **Select** menu, choose **Data Cepstrum**, as shown in Figure A-13.

The **Process Cepstrum** window opens, with the *.w file chosen in the **Stations and Channels** window displayed in the **File Processing...** display. The **Inprefix for Files** from the **Stations and Channels** window is displayed in the **Inprefix** box. Note that although browsing for different *.w files is possible by clicking on the **File Processing...** pushbutton, changes of the file used for processing must be made in the **Stations and Channels** window.

Defaults are used to fill in the variable values for the remaining inputs. The **Save Files** edit box is filled in with the path of the *.w file from the **Stations and Channels** window, with the /cepstra_files/ folder appended. The location of where to save the cepstra files may be changed. However, it should be saved in a folder by the name /cepstra_files/. Figure A-14 shows the **Process Cepstrum** window with default values.

To change values of the inputs for processing the cepstrum, simply change the values of the inputs. The values displayed on the **Process Cepstrum** window will be used to process the data cepstrum. If the altered inputs are to be saved for use as the future defaults, select the pull down menu **Utilities**, and choose **Save Defaults**. This will save the values to be used as the future defaults in the file default_data.mat in location C:/matlabR12/toolbox/Cepstrum/MATFILES/.

Figure A-14 shows the **Process Cepstrum** window with some of the input variables edited. To process the cepstrum, the pushbutton **Process Cepstrum** is pressed.

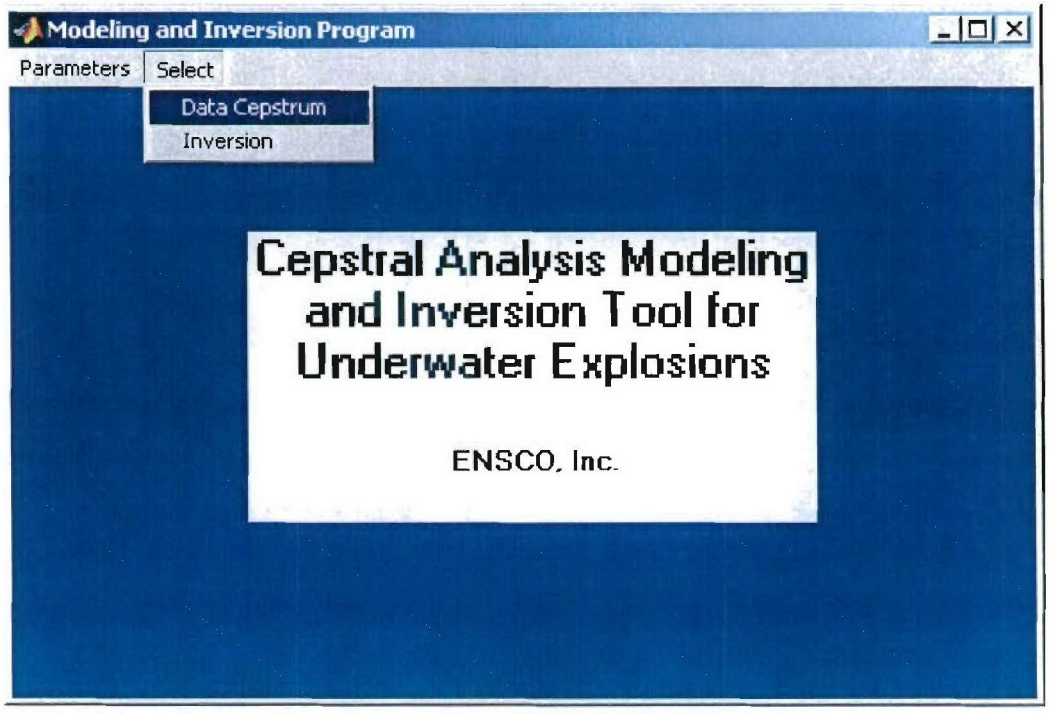

Figure A-13. Modeling and Inversion -- Data Cepstrum

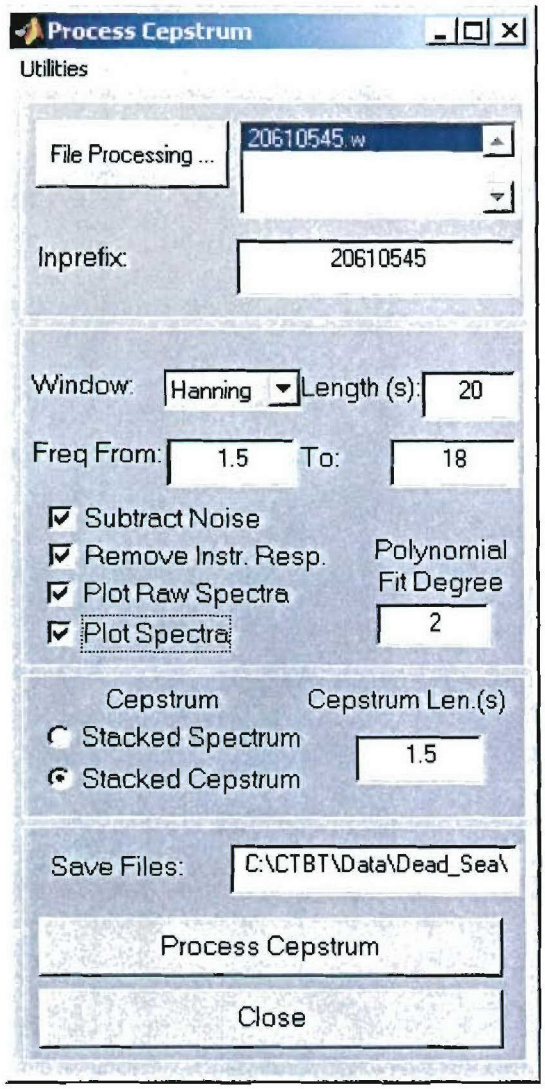

Figure A-14. Process Cepstrum Inputs

The inputs chosen in the **Process Cepstrum** window produce Figure A-15, Figure A-16, and Figure A-17. Since the **Plot Raw Spectra** and **Plot Spectra** options are both chosen, the plots in Figure A-15 and Figure A-16 are generated. The figures generated by the cepstral inversion program all contain a heading consisting of the orid, date, time, stations used to create plot (if applicable), and a brief title describing the plot.

The individual spectra, either raw or processed, are plotted in a separate figure for each station. The spectrum for each individual phase for each channel is plotted on the same

figure for each station. Since two channels (bn and bz) were selected for both the EIL and MRNI stations in the **Process Cepstrum** window, two traces for each phase are seen plotted in the plots in Figure A-15 and Figure A-16. The spectra are windowed by a Hanning window, and are a length of 20 seconds, set in **Window** and **Length (s)** in the **Process Cepstrum** window. The processed cepstrum reflects the **Freq From:** and **To:** values of 1.5 to 18 (Hz), and also the polynomial degree fit subtraction of 2 from the **Polynomial Fit Degree** input. Since **Subtract Noise** and **Remove Instr. Resp.** are both checked, the noise was subtracted from each of the spectrum phases, and the instrument response was removed. The time length of the cepstrum in Figure A-17 reflects the user input **Cepstrum Len.(s)** of 1.5 (s). The cepstrum was computed by stacking all of the phase cepstra.

The spectra plots of Figure A-15 and Figure A-16 display the spectra of all phases available for the station. However, for computing the stacked cepstrum in Figure A-17, only the phases that are available across all of the chosen stations are used. Since only the Pn phase is available for stations EIL and MRNI, only this station is used to compute the stacked cepstrum.

The cepstra files are saved in the C:/CTBT/Data/Dead_Sea/991111DeadSea/cepstra_files/ folder specified in the **Save Files** edit box in the **Process Cepstrum** window. The saved files are:

20610545.mat Contains the variables used for processing that are also needed for inversion

20610545.ST.cp Stacked Cepstrum

20610545.Ns.cp Stacked Noise Cepstrum

20610545.Lg.cp Stacked Phase Cepstrum (Lg phase)

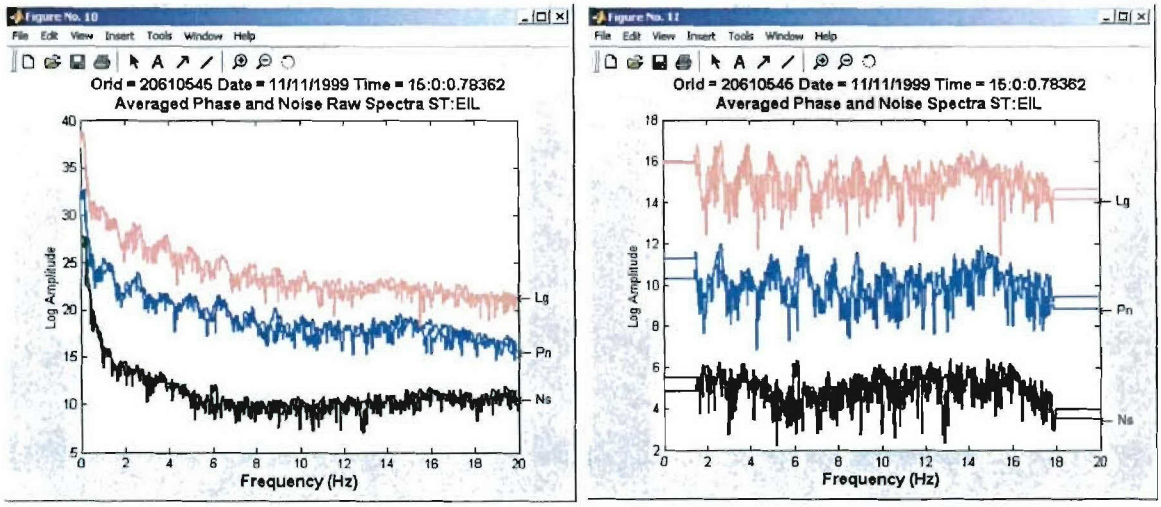

Figure A-15. Raw and Processed Spectra for Each Phase for EIL Station

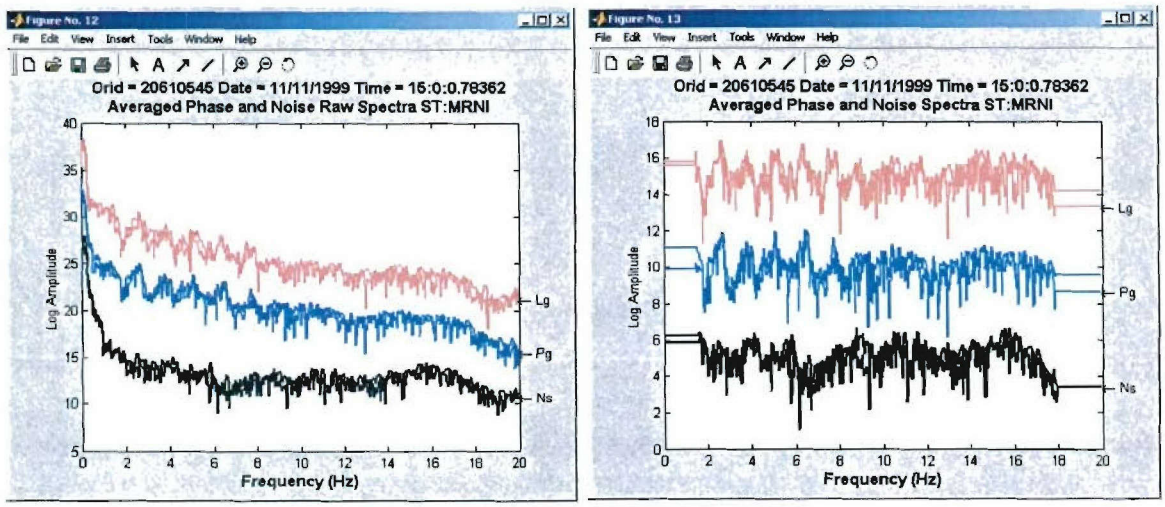

Figure A-16. Raw and Processed Spectra for Each Phase for MRNI Station

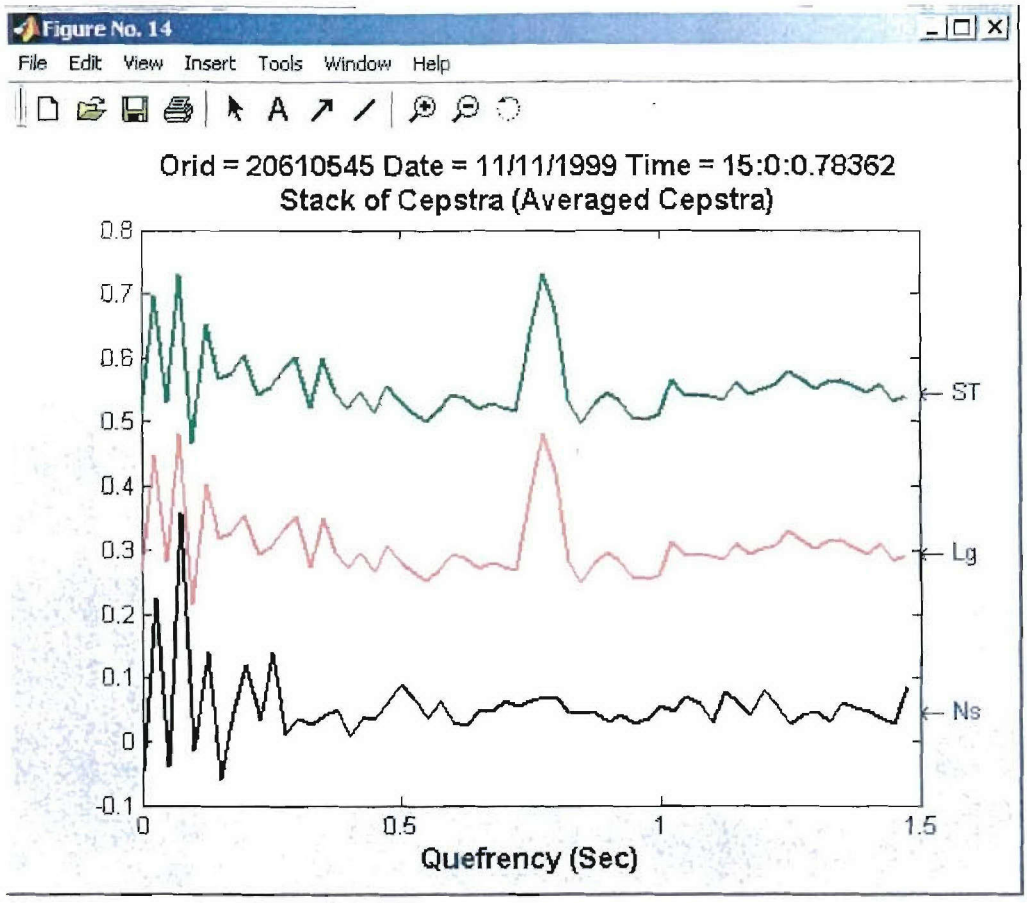

Figure A-17. Cepstra Computed with User Inputs

A2.4 CALCULATING DEPTH AND YIELD BY INVERSION.

The Inversion of the data cepstrum to the theoretical cepstrum is computed using the selected saved cepstra files, and the inputs to the **Inversion** and **Theoretical Cepstrum Parameters** window. Inversion of the data cepstrum to theoretical cepstra determines the best fit of depth and yield of the explosion

A2.4.1 Inversion

In the **Modeling and Inversion** window (Figure A-1), from the **Select** menu, choose **Inversion**, as shown in Figure A-18.

The **Inversion** window opens, with blank inputs for the **Saved Files...** and the **Inprefix:**. The inputs for the variables filling in the rest of the window are defaults (Figure A-19). Click on the **Saved Files...** pushbutton. This opens the **Browse Window,** Choose .cp or .sp File to Analyze (Figure A-20). The **Look In** directory is changed to C:/CTBT/Data/Dead_Sea/991111DeadSea/cepstra_files/. The browse window filters on .ST.cp files (Figure A-20). These files are the saved stack cepstra files saved from the **Process Cepstrum** window. The desired 20610545.ST.cp file is selected with the mouse. **Open** may now be pressed to open the file, or the file may be double clicked to open.

The **Saved Files...** box is filled in with the .ST.cp file chosen. The **Inprefix** edit box is filled in with the prefix of the chosen cepstra file. To change values of the parameter inputs for the inversion, simply change the values of the inputs. The values displayed in the **Inversion** window will be used to process the inversion. If the altered inputs are to be saved for use as the future defaults, select the pull down menu **Utilities**, and choose **Save Defaults**. This will save the values to be used as the future defaults in the file inv.mat in location C:/matlabR12/toolbox/Cepstrum/MATFILES/.

In order to determine, and also change the default theoretical parameters, the **Select Theoretical Parameters** pushbutton is pressed in the **Inversion** window. This opens the **Theoretical Cepstrum Parameters** window, with the default parameters as inputs (Figure A-22). Any of the input parameters may be edited. To use the changed parameters in the current inversion calculation, check the **Save Parameters** checkbox in the **Theoretical Parameters** window. To save the parameters for future default settings, in the **Inversion** window, select the pull down menu **Utilities**, and choose **Save Defaults**. Note that this will also save the inputs in the **Inversion** window to use as future defaults.

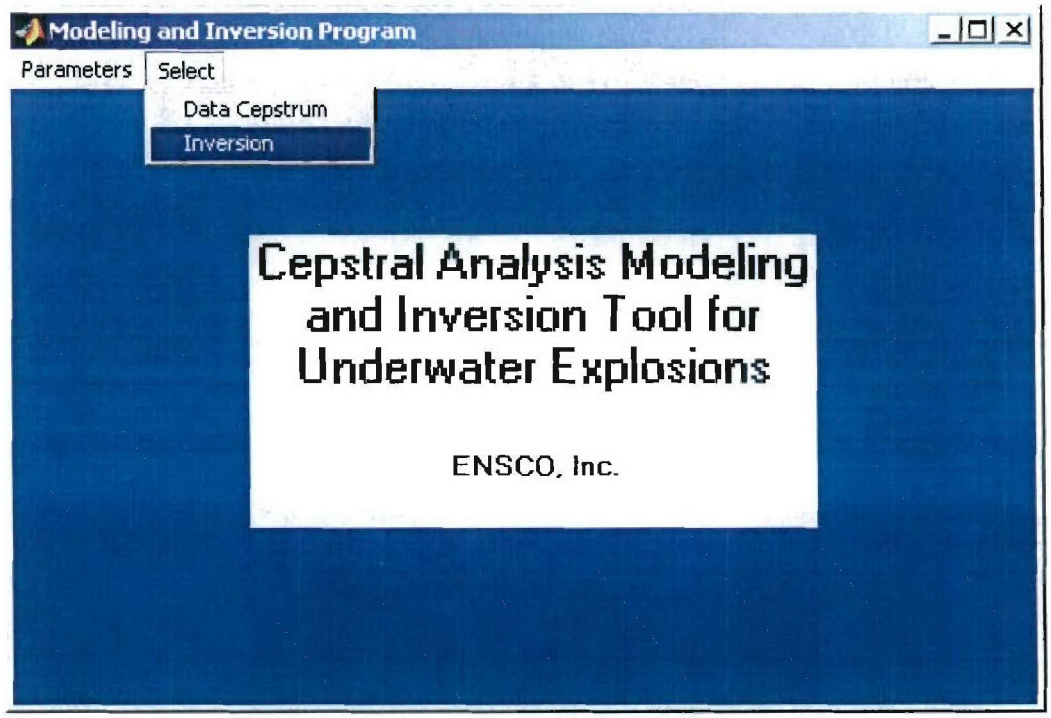

Figure A-18. Modeling and Inversion Program – Inversion

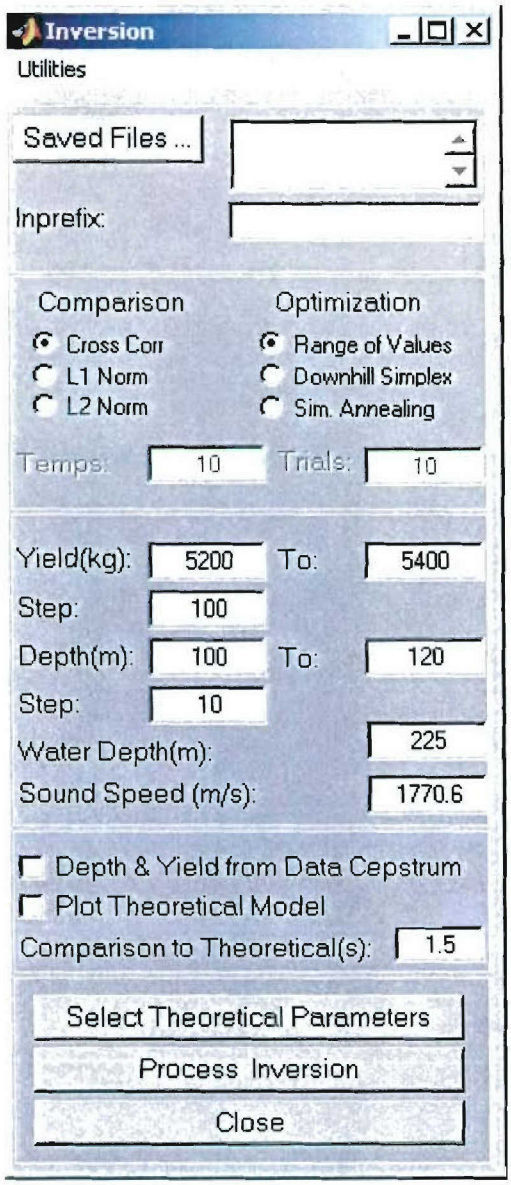

Figure A-19. Initial Inversion Window

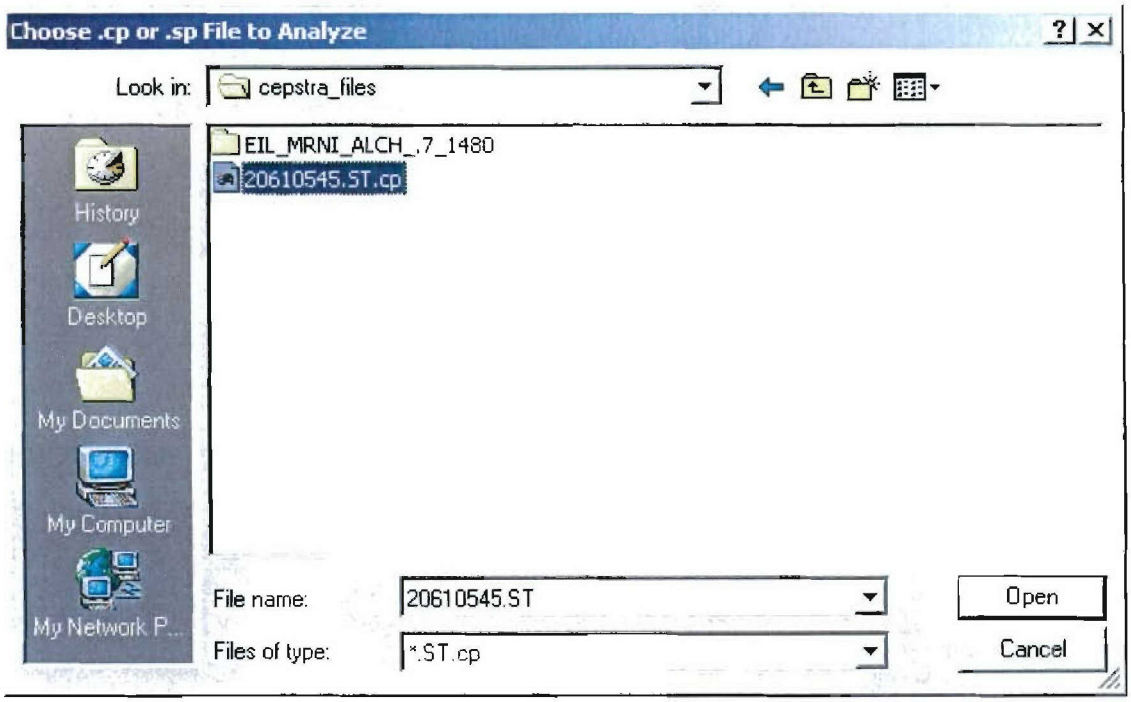

Figure A-20. Files Saved... Browse Window

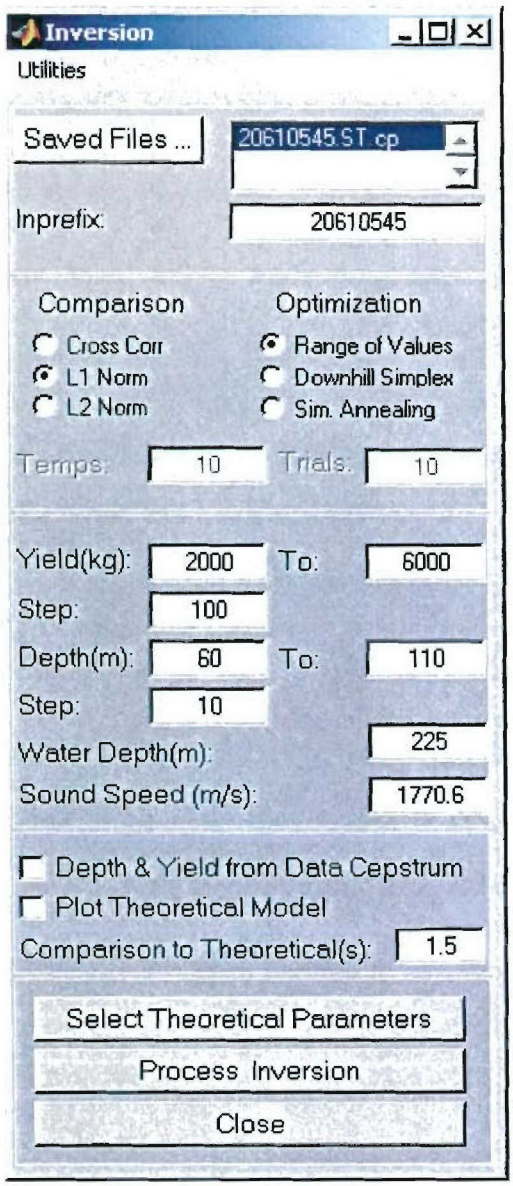

Figure A-21. Inversion Inputs

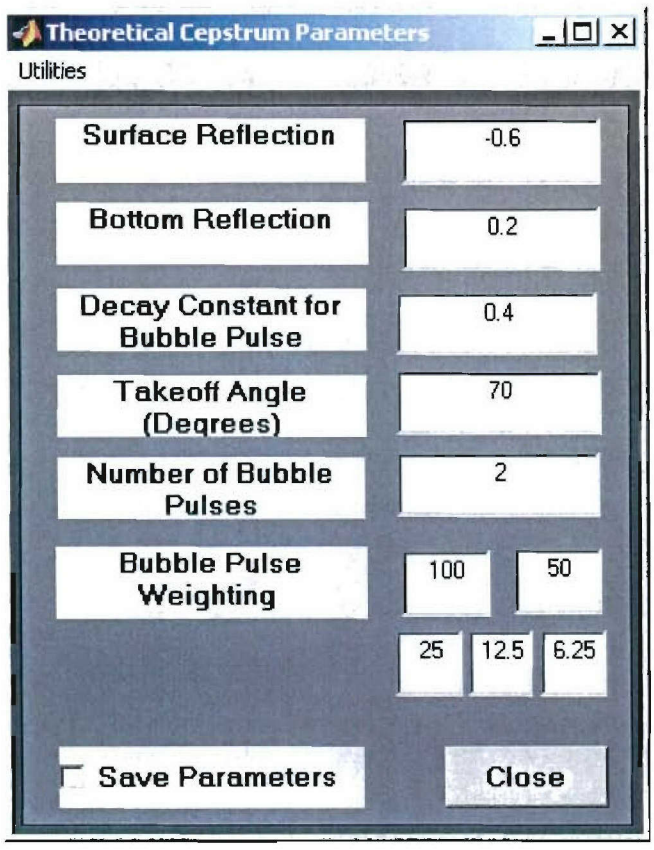

Figure A-22. Theoretical Cepstrum Parameters Window with Defaults

A2.4.2 Inversion using L1 Norm Comparison Method, and Range of Values Optimization Method

The inputs chosen in the **Inversion** window produce the related figures (Figure A-23, Figure A-24, Figure A-25, Figure A-26). First displayed is an image of the saved cepstra phase and stacked cepstra, used in the inversion algorithm (Figure A-23). The input of the **Saved Files...** and **Inprefix** boxes determine which saved cepstra files to use in the inversion and display. Parameters input in the **Inversion** window determine the comparison method of the data cepstrum to the theoretical cepstra. In this example, **L1 Norm** was chosen as the **Comparison** method, with a **Range of Values Optimization** method. The **Yield(kg):** and **To:** values of 2000 and 6000, respectively, is the range of yields for the theoretical cepstra, with a **Step:** of 100.

The data cepstrum is compared to theoretical cepstra, computed with the inputs of the **Inversion** and **Theoretical Cepstrum Parameters** inputs. Comparison of the data cepstrum with the range of values input into creating various theoretical cepstra produces corresponding 1-L1 Norm values. The range of values chosen in the **Inversion** window is reflected in the 3D plot of 1-L1 Norm of the data cepstrum and theoretical cepstra over the input range of values (Figure A-24). A contour plot of the range of values 1-L1Norm is also created, shown in Figure A-25. A search is made for the best match of 1-L1 Norm between the data cepstrum and the theoretical cepstra. The best matching theoretical cepstrum is plotted, in red dashes, along with the data cepstrum (Figure A-26). The depth, yield, and match values are listed in the plot title. The second plot in Figure A-26 shows the plot of 1-L1Norm, with depth constrained to the depth of maximizing the comparison. The plots in Figure A-26 are also shown for the second highest match between the theoretical and data cepstrum.

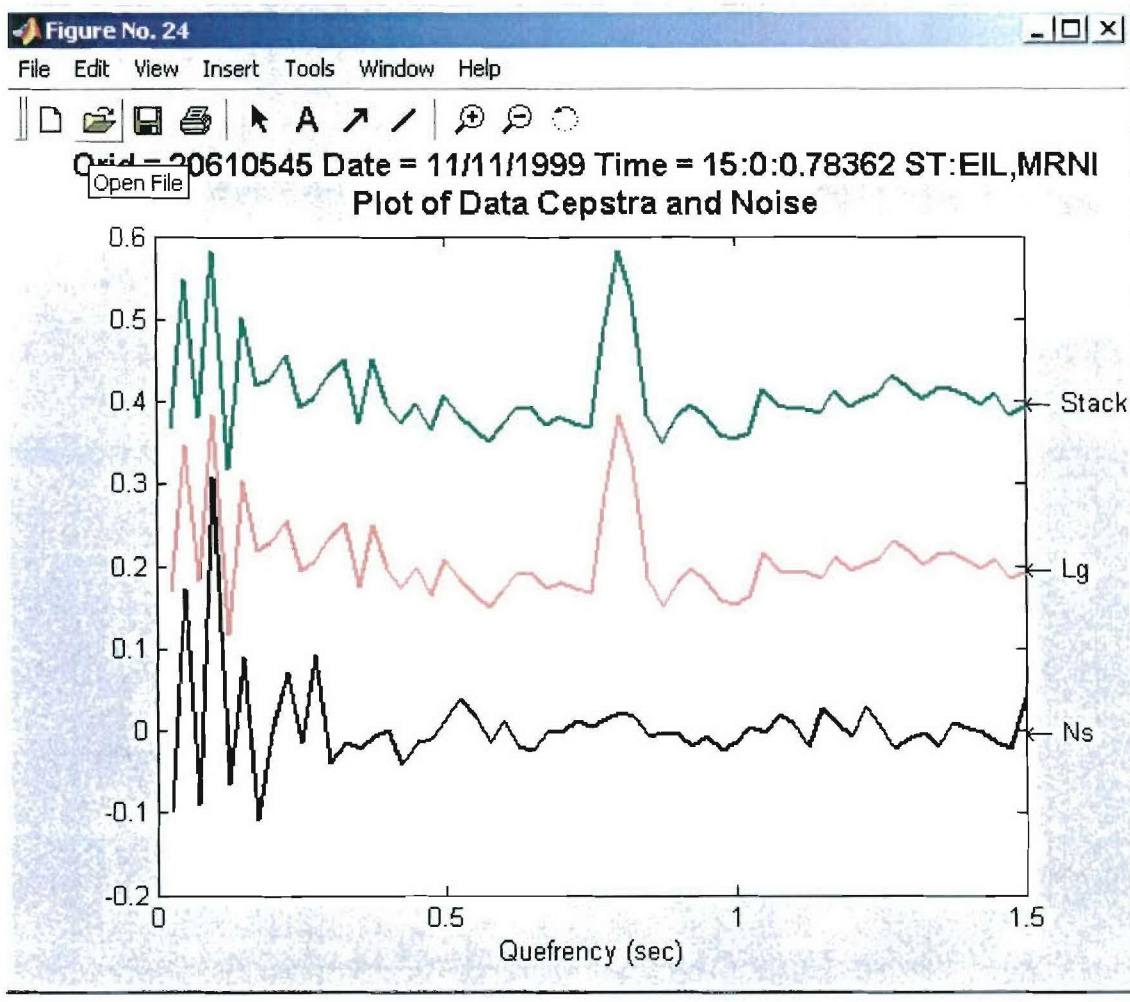

Figure A-23. Image of Saved Phase and Stack Cepstra Used for Inversion

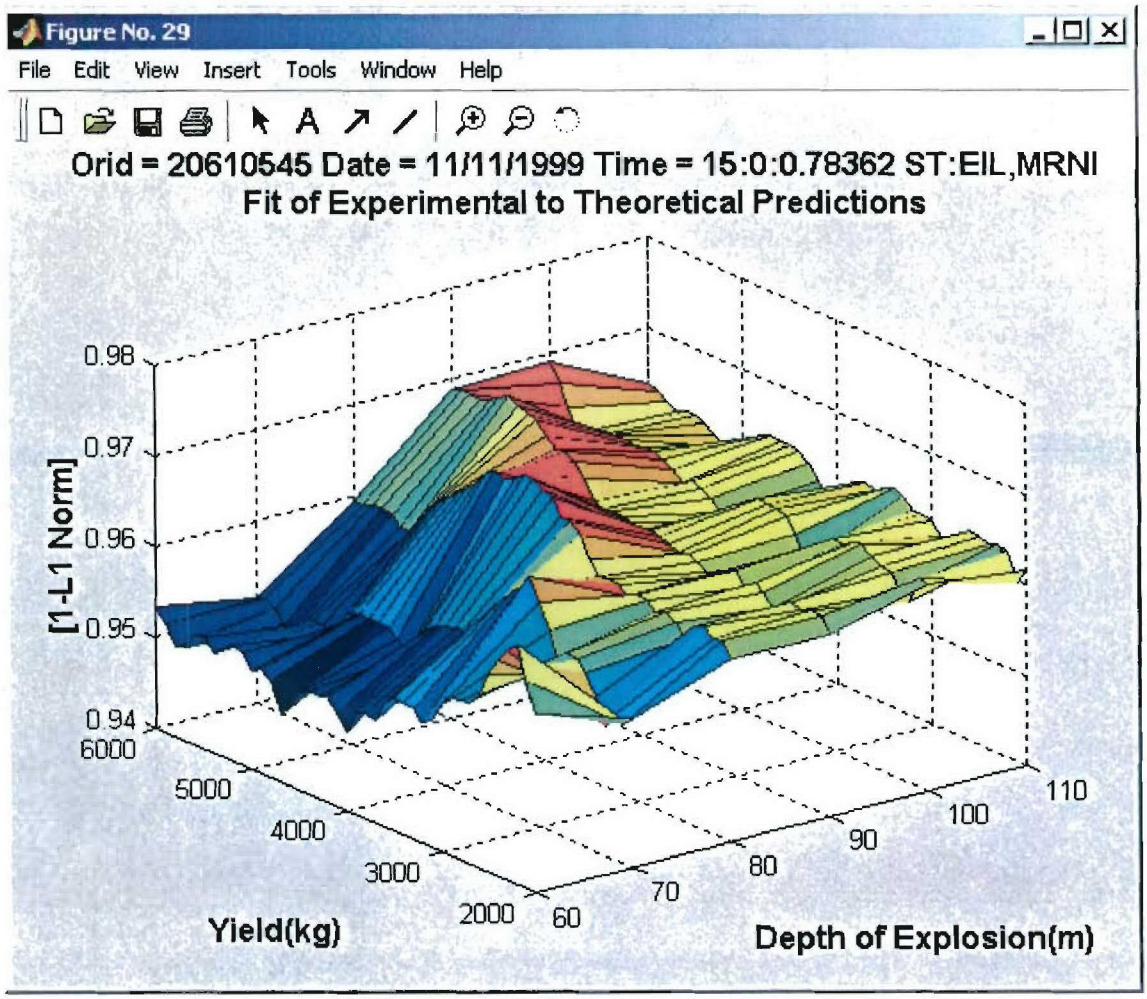

Figure A-24. 3D Range of Values

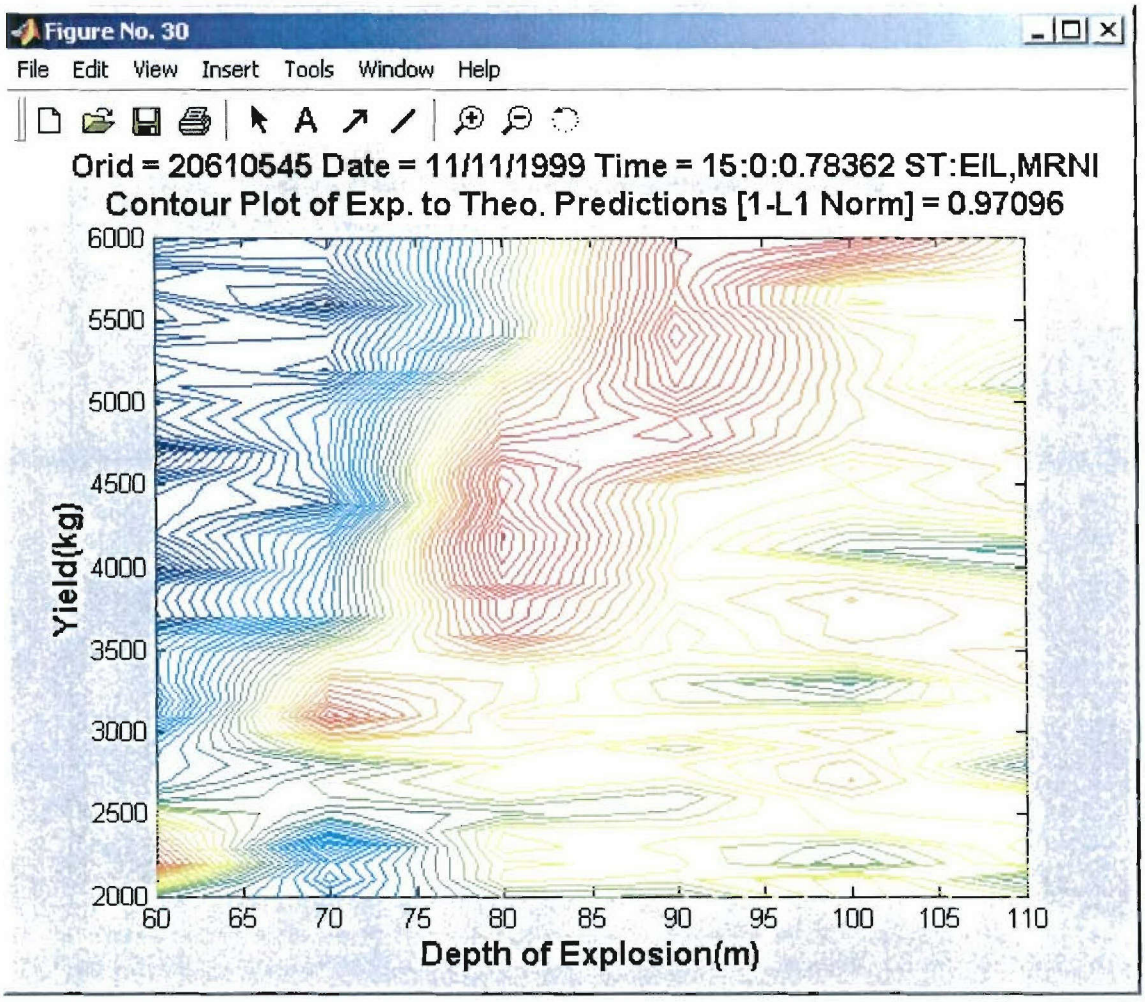

Figure A-25. Contour Plot of 1-L1 Norm of Data Cepstrum and Theoretical Cepstra

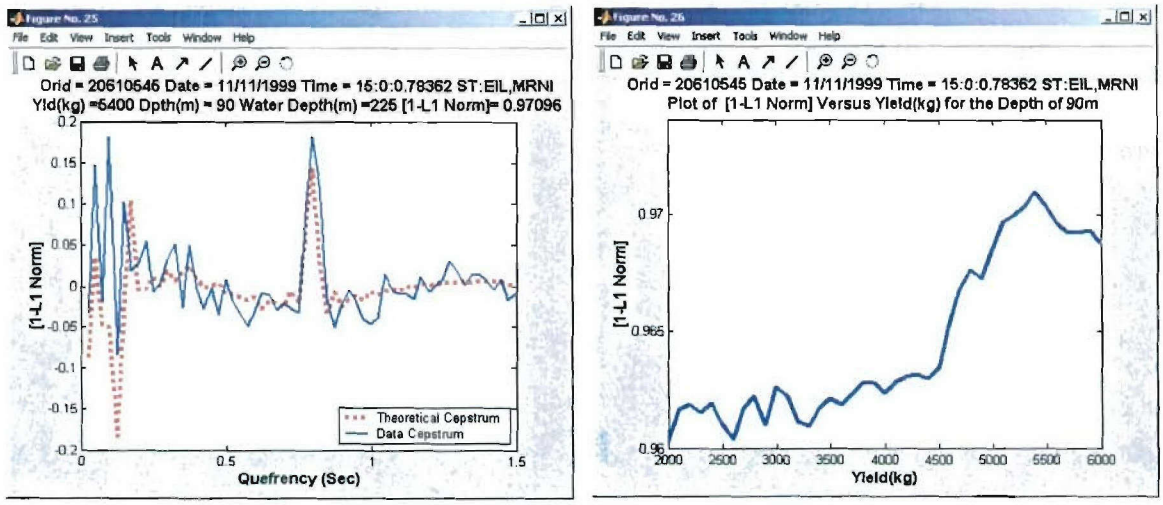

Figure A-26. Comparison of Theoretical and Data Cepstrum, and Plot of 1-L1 Norm vs. Yield

A2.4.3 Comparison Methods

The example in section A2.8 used the **L1 Norm Comparison** method for finding the depth and yield of the explosion. **Cross Corr**, or **L2 Norm** may also be used as the **Comparison** method between the data cepstrum and various theoretical cepstra. The same types of figures as those described above will be created, and labeled with the appropriate **Comparison** choice.

A2.4.4 Optimization Methods

The example in A2.8 used the **Range of Values Optimization** method. All combinations between **Comparison** and **Optimization** can be used to find the depth and yield of the explosion.

Choosing **Downhill Simplex** as the **Optimization** method changes the **Inversion** window to look as that in Figure A-27. The input required for **Yield(kg):** is a single value, which is the starting point of the Downhill Simplex algorithm. The single **Depth(m):** value also is a starting point for the algorithm. In this example, the default yield and depth were changed to match the best match yield and depth determined by the inversion algorithm for the range of values example in A2.4.2.

As for each inversion, the first figure created displays the data cepstra, as in Figure A-23. Each value of depth, yield, and surface reflection coefficient the downhill simplex algorithm chose, is marked with a blue 'x' in Figure A-28. Also shown is the best match, determined by the downhill simplex method for the comparison method of choice between the data and theoretical cepstra.

Since **Plot Theoretical Model** was checked, Figure A-29 was created. This shows the components of the model theoretical cepstrum for the depth and yield values of the best matching cepstrum.

Choosing the **Simulated Annealing Optimization** method uses an algorithm that attempts to find a global maximum match between the data cepstrum and theoretical cepstra. When this **Optimization** method is chosen, the **Temps:** and **Trials:** edit boxes become active. These may be changed to reflect the desired number of trial and temperatures for the algorithm. In this example **Depth and Yield from Data Cepstrum** was selected. This option allows the user to click on the bottom reflection and first bubble pulse in the data cepstrum figure (Figure A-23), which is plotted for each inversion computed. The user places the cursor over the desired location, a cross designates the location, and the user clicks (Figure A-30).

The results of the simulated annealing algorithm search are plotted, and the best depth and yield found.

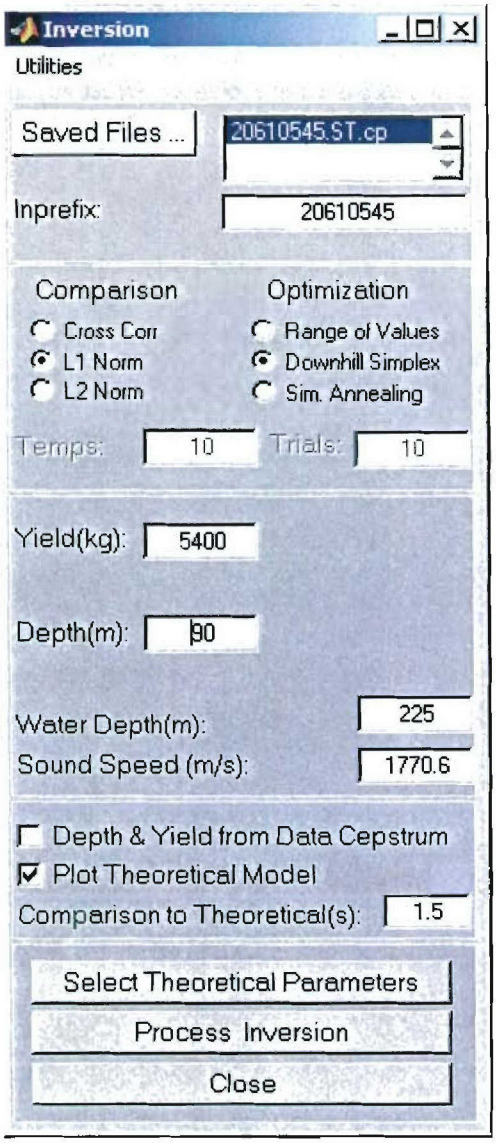

Figure A-27. Inversion with Optimization Method Downhill Simplex

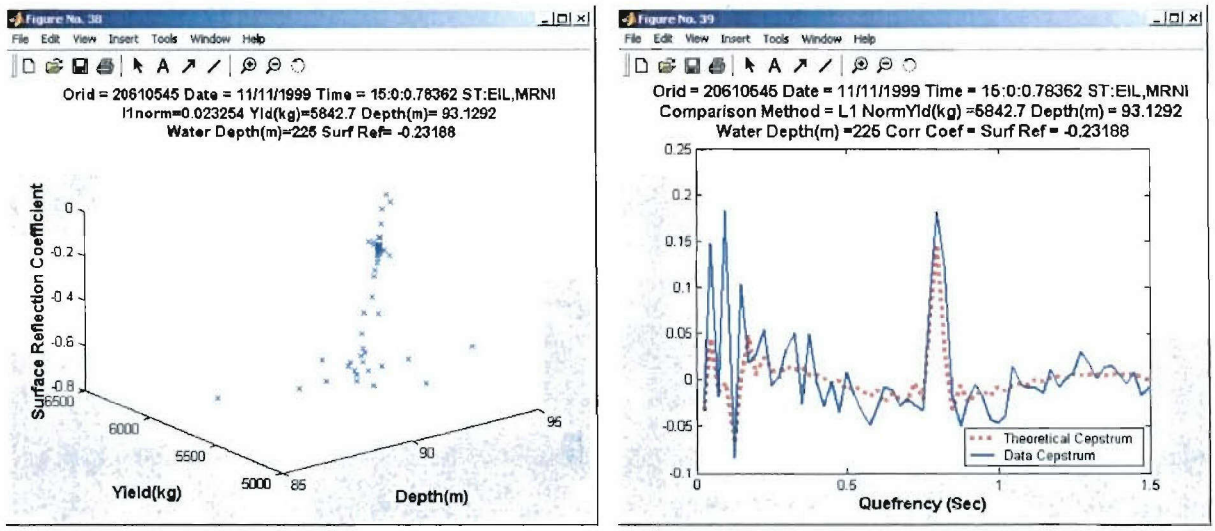

Figure A-28. Downhill Simplex Best Value Search, and Best Match of Data and Theoretical Cep strum

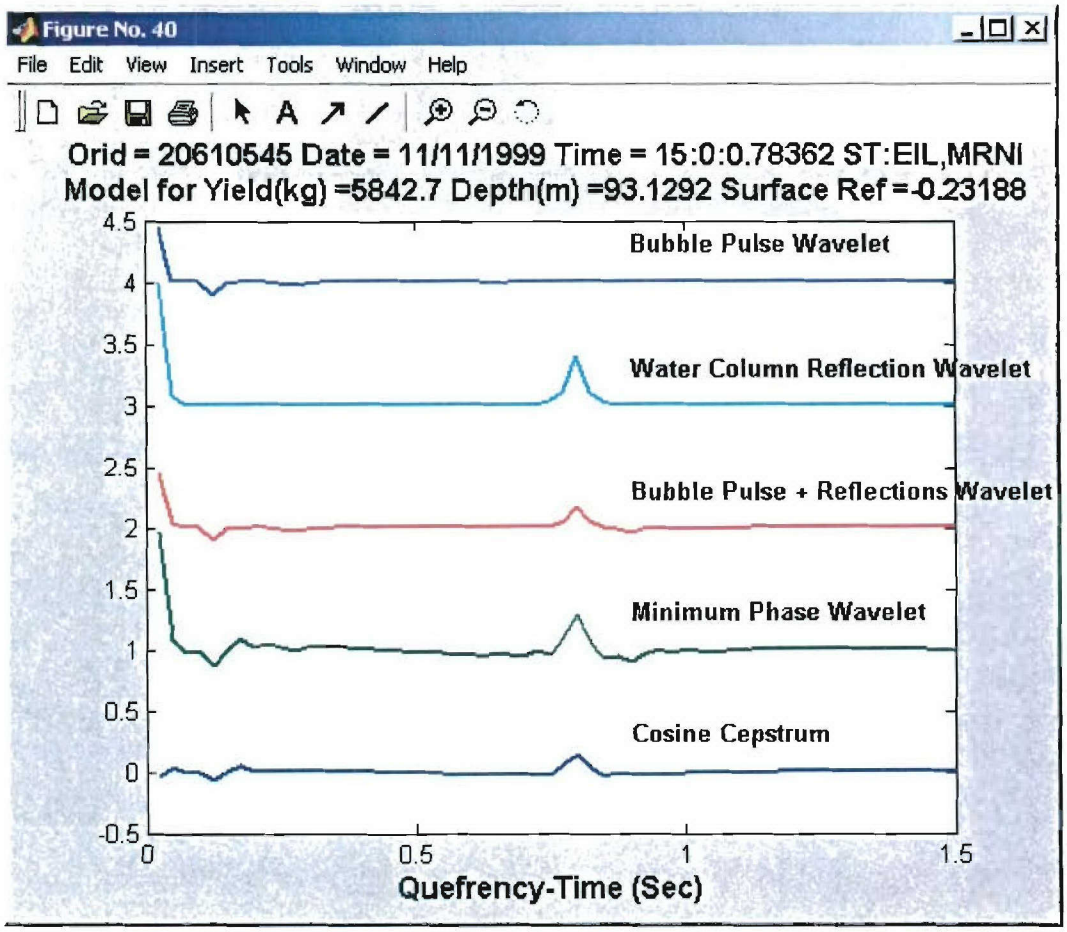

Figure A-29. Theoretical Model

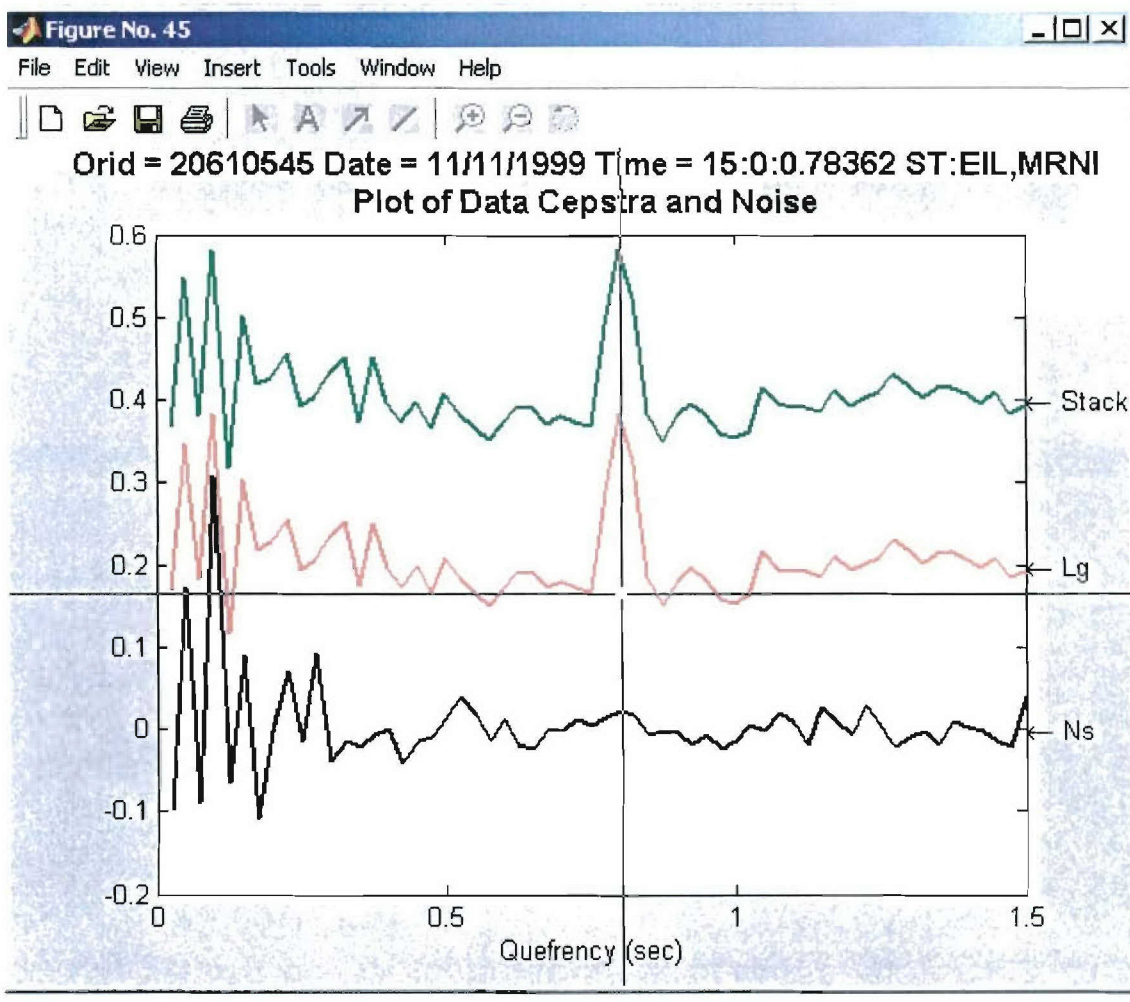

Figure A-30. Determining Starting Depth and Yield from User Inputs

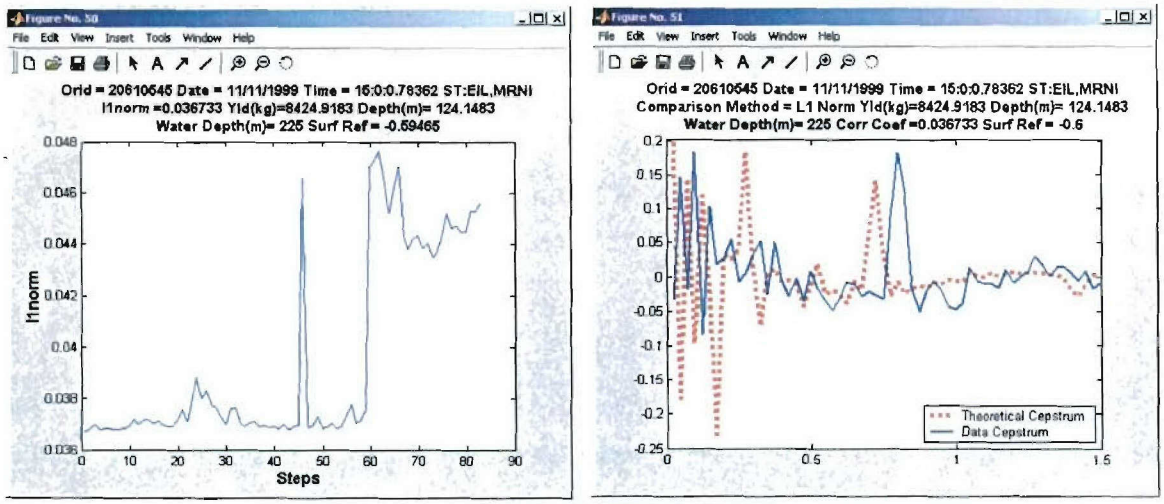

Figure A-31. Simulated Annealing, and Best Match of Data and Theoretical Cepstra

DEPARTMENT OF DEFENSE

DIRECTOR
DEFENSE INTELLIGENCE AGENCY
BUILDING 6000
WASHINGTON, DC 20340-5100
ATTN: DTIB

DIRECTOR
DEFENSE RESEARCH AND ENGINEERING
3030 DEFENSE PENTAGON
WASHINGTON, D.C. 20301-3030
ATTN: DDR&E, ROOM 3E808

DEFENSE TECHNICAL INFORMATION CENTER
8725 JOHN J. KINGMAN ROAD, SUITE 0944
FT. BELVOIR, VA 22060-6218
2 CYS ATTN: DTIC/OCA

DEFENSE THREAT REDUCTION AGENCY
8725 JOHN J. KINGMAN ROAD MS 6201
FT. BELVOIR, VA 22060-6201
ATTN: TDND, CPT. BARBER

OFFICE OF THE SECRETARY OF DEFENSE
CHEMICAL DEMILITARIZATION AND THREAT
REDUCTION OFFICE
1515 WILSON BOULEVARD, SUITE 720
ARLINGTON, VA 22209-2402
ATTN: P. WAKEFIELD
ATTN: DR. S. MANGINO

DEPARTMENT OF THE ARMY

US ARMY SMDC
SMDC-TC-YD
P.O. BOX 1500
HUNTSVILLE, AL 35807 3801
ATTN: B. ANDRE

DEPARTMENT OF THE AIR FORCE

AIR FORCE RESEARCH LABORATORY
29 RANDOLPH ROAD
HANSCOM AFB, MA 01731
ATTN: RESEARCH LIBRARY
ATTN: VSBL, R. RAISTRICK

USAF AT USGS
2201 SUNRISE VALLEY DRIVE MS 951
RESTON, VA 20192
ATTN: R. BLANDFORD
ATTN: R. JIH

AIR FORCE TECHNICAL APPLICATIONS CTR
1030 S. HIGHWAY AIA
PATRICK AFB, FL 32925 3002
ATTN: CA/STINFO
ATTN: TTR, D. CLAUTER
ATTN: CTI, DR. B. KEMERAIT
ATTN: TT, DR. D. RUSSELL
ATTN: TTR, F. SCHULTZ
ATTN: TTR, G. ROTHE
ATTN: TTR, V. HSU
ATTN: DR. B. NGUYEN
ATTN: DR. E. SMART
ATTN: DR. G. WAGNER
ATTN: DR. M. WOODS

DEPARTMENT OF THE NAVY

NAVAL RESEARCH LABORATORY
4555 OVERLOOK AVE, SW, CODE 7643
WASHINGTON, DC 20375 0001
ATTN: DR. D. DROB

DEPARTMENT OF ENERGY

NATIONAL NUCLEAR SECURITY
ADMINISTRATION
1000 INDEPENDENCE AVE SW
WASHINGTON, DC 20585 0420
ATTN: L. CASEY
ATTN: G. KIERNAN

UNIVERSITY OF CALIFORNIA
LAWRENCE LIVERMORE NATIONAL LAB
P.O. BOX 808
LIVERMORE, CA 94551 9900
ATTN: MS L205, DR. D. HARRIS
ATTN: MS 205, TECHNICAL STAFF

LOS ALAMOS NATIONAL LABORATORY
P.O. BOX 1663
LOS ALAMOS, NM 87545
ATTN: MS C335, DR. S. R. TAYLOR

PACIFIC NORTHWEST NATIONAL LABORATORY
P.O. BOX 999
1 BATTELEE BOULEVARD
RICHLAND, WA 99352
ATTN: MS P8-20, T. HEIMBIGNER
ATTN: MS K8-29, DR. N. WOGMAN

SANDIA NATIONAL LABORATAORIES
MAIL SERVICES
P.O. BOX 5800
ALBUQUERQUE, NM 87185 1164
ATTN: WILLIAM GUYTON

OTHER GOVERNMENT

DEPARTMENT OF STATE
2201 C STREET NW
WASHINGTON, DC 20520
ATTN: R. MORROW, ROOM 5741

US GEOLOGICAL SURVEY
905 NATION CENTER
12201 SUNRISE VALLEY DR
RESTON, VA 20192
ATTN: W. LEITH

US GEOLOGICAL SURVEY
345 MIDDLEFIELD RD MS 977
MENLO PARK, CA 94025
ATTN: S. DETWEILER
ATTN: DR. W. MOONEY

DEPARTMENT OF DEFENSE CONTRACTORS

BATTELLE
MANAGER, ENERGETIC SYSTEMS & SECURITY TECHNOLOGIES
505 KING AVE
COLUMBUS, OH 43201-2693
ATTN: NEAL OWENS (7-2-081)

BBN CORPORATION
1300 N 17TH STREET, SUITE 400
ARLINGTON, VA 22209
ATTN: DR. D. NORRIS
ATTN: R. GIBSON
ATTN: J. PULLI

CENTER FOR MONITORING RESEARCH
1953 GALLOWS ROAD, SUITE 260
VIENNA, VA 22182 3997
ATTN: DR. K. L. MCLAUGLHLIN
ATTN: DR. R. WOODWARD
ATTN: DR. R. NORTH
ATTN: DR. X. YANG
ATTN: LIBRARIAN

ENSCO, INC.
5400 PORT ROYAL ROAD
SPRINGFIELD, VA 22151 2312
ATTN: D. BAUMGARDT
ATTN: Z. DER

WESTON GEOPHYSICAL CORPORATION
27 BEDFORD ST, SUITE 102
LEXINGTON, MA 02420
ATTN: DR. D. REITER
ATTN: J. LEWKOWICZ
ATTN: DR. A. ROSCA
ATTN: DR. I. TIBULEAC
ATTN: M. JOHNSON

ITT INDUSTRIES
ITT SYSTEMS CORPORATION
1680 TEXAS STREET SE

KIRTLAND AFB, NM 87117 5669
2 CYS ATTN: DTRIAC
ATTN: DARE

TITAN
1900 CAMPUS COMMONS DR SUITE 600
RESTON, VA 20191-1535
ATTN: DR. C. P. KNOWLES

MISSION RESEARCH CORPORATION
8560 CINDERBED ROAD, SUITE 700
NEWINGTON, VA 22122
ATTN: DR. M. FISK

MULTIMAX, INC
1441 MC CORMICK DRIVE
LANDOVER, MD 20785
ATTN: DR. I. N. GUPTA
ATTN: W. RIVERS

MULTIMAX, INC
1090 N HIGHWAY A1A SUITE D
INDIANLATIC, FL 32903
ATTN: DR. H. GHALIB

SCIENCE APPLICATIONS INTERNATIONAL CORP
10260 CAMPUS POINT DRIVE
SAN DIEGO, CA 92121 1578
ATTN: DR.M. ENEVA
ATTN: DR. G. E. BAKER
ATTN: DR. J. STEVENS
ATTN: DR. D. ADAMS

SCIENCE APPLICATIONS INT'L CORP
1227 S. PATRICK DR SUITE 110
SATELLITE BEACH, FL 32937
ATTN: DR. M. FELIX
ATTN: DR. H. GIVEN

URS CORPORATION
566 EL DORADO STREET
PASADENA, CA 91109 3245
ATTN: DR. N.B. WOODS
ATTN: DR. C. SAIKIA
ATTN: DR. G. ICHINOSE

DIRECTORY OF OTHER (LIBRARIES AND UNIVERSITIES)

BOSTON COLLEGE
INSTITUTE FOR SPACE RESEARCH
140 COMMONWEALTH AVENUE
CHESTNUT HILL, MA 02167
ATTN: DR. D. HARKRIDER
ATTN: B. SULLIVAN

BROWN UNIVERSITY
DEPARTMENT OF GEOLOGICAL SCIENCES
75 WATERMAN STREET
PROVIDENCE, RI 02912 1846
ATTN: PROF. D. FORSYTH

CALIFORNIA INSTITUTE OF TECHNOLOGY
DIVISION OF GEOLOGY & PLANETARY SCIENCES
PASADENA, CA 91125
ATTN: PROF. DONALD V. HELMBERGER
ATTN: PROF. THOMAS AHRENS

UNIVERSITY OF CALIFORNIA BERKELEY
281 MCCONE HALL
BERKELEY, CA 94720 2599
ATTN: PROF. B. ROMANOWICZ
ATTN: DR. D. DREGER

UNIVERSITY OF CALIFORNIA-DAVIS
DEPT OF STATISTICS
DAVIS, CA 95616
ATTN:. R H SHUMWAY, DIV STATS

UNIVERSITY OF CALIFORNIA SAN DIEGO
SCRIPPS INSTITUTION OF TECHNOLOGY
9500 GILMAN DRIVE
LA JOLLA, CA 92093 0225
ATTN: DR. L. DEGROOT - HEDLIN
ATTN: DR. M. HEDLIN
ATTN: PROF. F. VERNON
ATTN: PROF. J. BERGER
ATTN: J. ORCUTT

UNIVERSITY OF CALIFORNIA SANTA CRUZ
INSTITUTE OF TECTONICS
SANTA CRUZ, CA 95064
ATTN: DR. R. S. WU
ATTN: PROF. T. LAY

UNIVERSITY OF COLORADO BOULDER
DEPT OF PHYSICS, CAMPUS BOX 390
BOULDER, CO 80309
ATTN: DR.R. ENGDAHL
ATTN: M. RITZWOLLER
ATTN: PROF. C. ARCHAMBEAU

COLUMBIA UNIVERSITY
LAMONT DOHERTY EARTH OBSERVATORY
PALISADES, NY 10964
ATTN: DR. J. XIE
ATTN: DR. W. Y. KIM
ATTN: PROF. P.G. RICHARDS
ATTN: DR. M. TOLSTOY

UNIVERSITY OF CONNECTICUT
DEPARTMENT OF GEOLOGY & GEOPHYSICS
STOORS, CT 06269 2045
ATTN: PROF. V.F. CORMIER, U-45,
ROOM 207

CORNELL UNIVERSITY
DEPARTMENT OF GEOLOGICAL SCIENCES
3126 SNEE HALL
ITHACA, NY 14853
ATTN: PROF. M.A. BARAZANGI

HARVARD UNIVERSITY
HOFFMAN LABORATORY
20 OXFORD STREET
CAMBRIDGE, MA 02138
ATTN: PROF. A. DZIEWONSKI
ATTN: PROF. G. EKSTROM

INDIANA UNIVERSITY
DEPARTMENT OF GEOLOGICAL SCIENCES
1005 10TH STREET
BLOOMINGTON, IN 47405
ATTN: PROF. G. PAVLIS

IRIS
1200 NEW YORK AVENUE, NW SUITE 800
WASHINGTON, DC 20005
ATTN: DR. D. SIMPSON

IRIS
1408 NE 45TH ST #201
SEATTLE, WA 98105
ATTN: DR. T. AHERN

MASSACHUSETTS INSTITUTE OF TECHNOLOGY
EARTH RESOURCES LABORATORY
42 CARLETON STREET
CAMBRIDGE, MA 02142
ATTN: DR. W. RODI
ATTN: PROF. M.N. TOKSOZ

MICHIGAN STATE UNIVERSITY LIBRARY
450 ADMINISTRATION BUILDING
EAST LANSING, MI 48824
ATTN: K. FUJITA

NEW MEXICO STATE UNIVERSITY
DEPARTMENT OF PHYSICS
LAS CRUCES, NM 88003
ATTN: PROF. J. NI
ATTN: PROF. T. HEARN

NORTHWESTERN UNIVERSITY
DEPARTMENT OF GEOLOGICAL SCIENCES
1847 SHERIDAN RD
EVANSTON, IL 60208
ATTN: PROF. E. OKAL

PENNSYLVANIA STATE UNIVERSITY
GEOSCIENCES DEPARTMENT
403 DEIKE BUILDING
UNIVERSITY PARK, PA 16802
ATTN: PROF. C. AMMON
ATTN: PROF. S. ALEXANDER
ATTN: DR. A. NYBLADE

SAN DIEGO STATE UNIVERSITY
DEPARTMENT OF GEOLOGICAL SCIENCES
SAN DIEGO, CA 92182
ATTN: PROF. S. M. DAY

SOUTHERN METHODIST UNIVERSITY
DEPARTMENT OF GEOLOGICAL SCIENCES
P.O. BOX 750395
DALLAS, TX 75275
ATTN: B. STUMP
ATTN: E. HERRIN
ATTN: P. GOLDEN

UNIVERSITY OF HAWAII- MANOA
P.O. BOX 1599
KAILUA-KONA, HI 96745 1599
ATTN: DR. M. A. GARCES

UNIVERSITY OF MISSISSIPPI
1 COLISEUM DRIVE
UNIVERSITY, MS 38677
ATTN: PROF. H. BASS

UNIVERSITY OF SOUTHERN CALIFORNIA
520 SEAVER SCIENCE CENTER
UNIVERSITY PARK
LOS ANGELES, CA 90089 0483
ATTN: PROF. C. G. SAMMIS
ATTN: PROF. T. JORDAN

UNIVERSITY OF WISCONSIN MADISON
1215 W DAYTON ST
MADSION, WI 53706 1600
ATTN: DR. C. THURBER

ST LOUIS UNIVERSITY
EARTH & ATMOSPHERIC SCIENCES
STATION 3507 LACLEDE AVE
ST LOUIS, MO 63103
ATTN: PROF. B. J. MITCHELL
ATTN: PROF. R. HERRMAN

UNIVERSITY OF MEMPHIS
3890 CENTRAL AVE
MEMPHIS, TN 38152
ATTN: DR. J. PUJOL

UNIVERSITY OF MEMPHIS
3876 CENTRAL AVE
MEMPHIS, TN 38152
ATTN: DR. C. LANGSTON

UNIVERSITY OF TEXAS AUSTIN
IGS 130
AUSTIN, TX 78712
ATTN: DR. J. PULLIAM

UNIVERSITY OF TEXAS AUSTIN
IGS 131
AUSTIN, TX 78712
ATTN: DR. M. SEN

UNIVERSITY OF TEXAS EL PASO
DEPT OF GEOLOGICAL SCIENCES
EL PASO, TX 79901
ATTN: PROF. G. KELLER
ATTN: DR. D. DOSER
ATTN: DR. A. VELASCO

FOREIGN

AUSTRALIAN GEOLOGICAL SURVEY
ORGANIZATION
CORNER OF JERRAGOMRRRA &
NINDMARSH DRIVE
CANBERRA, ACT 2609
AUSTRALIA
ATTN: D. JEPSON

GEOPHYSICAL INSTITUTE OF ISRAEL
POB 182
LOD, 7100 ISRAEL
ATTN: DR. Y. GITTERMAN
ATTN: DR. A. SHAPIRA

GEOLOGICAL SURVEY OF CANADA
7 OBSERVATORY CRESCENT
OTTAWA K1A 0Y3 ONT
CANADA
ATTN: C. WOODGOLD

I.R.I.G.M. B.P. 68
38402 ST. MARTIN D'HERES
CEDEX, FRANCE
ATTN: DR. M. BOUCHON

MINISTRY OF DEFENSE
PROCUREMENT EXEUTIVE
BLACKNESS, BRIMPTON
READING FG7-4RS ENGLAND
ATTN: DR. D. BOWERS

NTNF/NORSAR
P.O. BOX 51
N-2007 KJELLER, NORWAY
ATTN: DR. F. RINGDAL
ATTN: T. KVAERNA
ATTN: S. MYKKELTVEIT